Sea State Estimation from Inertial Platform Data for Real-Time Ocean Wave Prediction

Tinashe G. Gwatiringa

Department of Electrical Engineering
University of Cape Town
Rondebosch, Cape Town
South Africa

Supervisor:
Prof. E. Boje

Co-supervisor:
Robyn A. Verrinder

August 2018

MSc. thesis submitted in fulfilment of the requirements for the degree of Master of Science in the Department of Electrical Engineering at the University of Cape Town

Keywords: state estimation; wave glider; control theory

Declaration

I, Tinashe G. Gwatiringa, hereby:

1. grant the University of Cape Town free licence to reproduce the above thesis in whole or in part, for the purpose of research;

2. declare that:

   (a) this thesis is my own unaided work, both in concept and execution, and apart from the normal guidance from my supervisor, I have received no assistance except as stated below:

   (b) neither the substance nor any part of the above thesis has been submitted in the past, or is being, or is to be submitted for a degree at this University or at any other university, except as stated below.

   (c) this dissertation has been submitted to the Turnitin module and I confirm that my supervisor has seen my report and any concerns revealed by such have been resolved with my supervisor.

Signed by candidate

Tinashe G. Gwatiringa

Department of Electrical Engineering
University of Cape Town

Tuesday 21st August, 2018

This page has been intentionally left blank.

Abstract

Sea State Estimation from Inertial Platform Data for Real-Time Ocean Wave Prediction

Tinashe G. Gwatiringa

Tuesday 21st August, 2018

Ocean observation is vital in understanding how the oceans contribute toward climate change and other effects. This is one of many undertakings requiring a persistent presence in the oceans. These maritime activities are mainly carried out on large research vessels chartered for weeks at a time, which can be extremely costly.

In addition, the data obtained when using these vessels are only short snapshots of the continual processes that occur. Recently, there has been a drive toward using Unmanned Surface Vehicles (USVs) and Unmanned Underwater Vehicles (UUVs), which can be deployed at a fraction of the cost, and provide greatly improved spatio-temporal data. The wave glider (WG) is one such autonomous marine robot used for persistent ocean research and other maritime activities, and forms the focus of this study. The WG is a low power USV/UUV hybrid that harnesses wave energy for propulsion, and has a small solar- and battery-powered thruster, and a rudder for steering.

Due to effects of waves, currents, and other disturbances, the platform tends to veer off its desired path. Additionally, local sea state information is not taken into consideration while manoeuvring, hence energy extraction from ocean waves is not optimal. More sophisticated navigation algorithms operating on a per-wave strategy may improve accuracy along a specified path and maximise the energy uptake from the waves.

To realise these improvements requires prediction of local wave behaviour. If one can predict what the wave field will be a short time in the future, then possible control action can be taken to efficiently navigate in the environment. Inertial measurements and wave modelling have been used to improve localisation of the WG platform directly, and predict the platform's velocity. However there is limited work in the context of WG navigation. Hence the problem this dissertation aims to solve is the estimation and subsequent prediction of local wave behaviour.

This work proposes a novel approach to estimate the sea state and hence predict short-term, local wave behaviour from inertial measurements on a slow-moving marine platform such as the WG. A Kalman filtering strategy consisting of a phase-locked loop and filter based sea state estimator is used to generate local height and angle of arrival estimates. This method offers an improvement over existing Fast Fourier Transform methods as it does not require long time series data to produce results, and enables the prediction of wave behaviour a short time into

the future.

The ideas are tested in simulation by generating wind waves using ocean wave models such as the Pierson Moskowitz model, and dynamic a dynamic model of the WG platform. In addition, a small scale lab experiment is carried out to verify the performance of the sea-state estimator developed. Preliminary results obtained indicate that relative wave height can be estimated on-board a marine platform, using only inertial sensors.

This page has been intentionally left blank.

Acknowledgements

The financial assistance of the South African Department of Science and Technology (DST) and Council for Scientific and Industrial Research (CSIR) via the Robotics Strategy of South Africa (ROSSA) grant is hereby acknowledged. Opinions expressed and conclusions arrived at, are those of the author and are not necessarily to be attributed to the DST and CSIR.

I would like to thank my supervisor, Prof. Edward Boje, for the guidance and advice provided throughout my time as his student. I would also like to thank my co-supervisor, Robyn Verrinder, for her continued support. I have been extremely lucky to have two supervisors working closely with me, and providing prompt feedback in times of doubt.

Finally, a great thank you to the friends and family who took this journey with me. In particular, Darryn Jordan and Gevashkar Rampersadh, who kept me sane during the long nights on campus.

This work is dedicated to Shadreck T. S. Makombe, for he taught me the value of education.

Contents

List of Figures

This page has been intentionally left blank.

List of Tables

Nomenclature

$\bar{\gamma}$	Expected random phase [rad]
λ_i	Spatial wavelength [m]
$\mathcal{O}$	Observability matrix
$\mathcal{T}$	Denavit-Hartenberg homogeneous transformation
$\mathcal{U}(a, b)$	Uniformly distributed number between the interval a and b
ω	Angular frequency [$\text{rad} \cdot \text{s}^{-1}$]
θ	Mean wave propagation direction [rad]
$\vec{k}$	Wave number vector [$\text{rad} \cdot \text{m}^{-1}$]
D	Depth to the ocean floor [m]
$E\{\}$	Expectation operator
g	Acceleration due to gravity [$9.81\,\text{m} \cdot \text{s}^{-2}$]
H_s	Significant wave height [m]
$N(\mu, \sigma^2)$	Normally distributed random variable, with mean, μ, and variance, σ^2
U_x	Wind speed at x metres above the mean sea level [$\text{m} \cdot \text{s}^{-1}$]
2D	Two Dimensional
3D	Three Dimensional
AIC	Akaike Information Criterion
BODY	Body Fixed Reference Frame
CFD	Computational Fluid Dynamics
CSIR	Council for Scientific and Industrial Research
DH	Denavit-Hartenberg Coordinate Referencing
DOF	Degrees of Freedom
ECEF	Earth Centred, Earth Fixed Reference Frame
EKF	Extended Kalman Filter
FFT	Fast Fourier Transform

GPS Global Positioning System

IMU Inertial Measurement Unit

JONSWAP Joint North Sea Wave Project

KF Kalman Filter

MEMS Micro Electro Mechanical Sensor

NED North-East-Down Reference Frame

NOAA National Oceanic and Atmospheric Administration

PLL Phase-Locked Loop

PM Pierson-Moskowitz Wave Model

PSD Power Spectral Density

RAO Response Amplitude Operator

SNAME Society of Naval Architects and Marine Engineers

SNR Signal to Noise Ratio

SNTP Simple Network Time Protocol Server

SOCCO Southern Ocean Carbon and Climate Observatory

TRIAD Triaxial Attitude Determination

USV Unmanned Surface Vehicle

UTC Coordinated Universal Time

UUV Unmanned Underwater Vehicle

VCO Voltage Controller Oscillator

WG Wave Glider

Chapter 1

Introduction

Understanding ocean dynamics plays a critical role in navigation, scientific observation, and other maritime activities. The Council for Scientific and Industrial Research (CSIR) and Southern Ocean Carbon and Climate Observatory (SOCCO) have marine research activities that require persistent monitoring of ocean features such as dissolved carbon dioxide, temperature, and algal blooms, amongst others [1, 2]. These monitoring activities are mainly carried out on large research vessels chartered for weeks at a time, often at great cost. Additionally, the data obtained when using research ships are only a short snapshot of the continual processes that occur in the oceans.

There has recently been a drive towards using unmanned surface vehicles (USV), and unmanned underwater vehicles (UUV), which can be deployed to gather data at low cost relative to research vessels. Moreover, they are capable of longer missions at sea [3, 4]. These robotic platforms have proven to be well suited to the remote and often inhospitable environments such as the Southern Ocean [5]. The increase in sensor-rich platforms at sea presents an opportunity to generate high resolution measurements, and to improve ocean dynamic models. In turn, these can be used for more advanced navigation strategies, in addition to extending the capabilities of scientific observation.

Fig. 1.1 shows the Liquid Robotics Wave Glider (WG), a USV/UUV hybrid which forms the focus of this study. The WG is a low power platform that harnesses wave energy for propulsion. A small solar- and battery-powered thruster and rudder provide steering and power for on-board electronics. This enables the WG to be deployed for months at a time, and it has proven indispensable as a marine platform [5–7]. Not only is the WG an effective ocean research platform, it is also used for ocean surveillance in the defence industry, exploration in the oil and gas industry, as well as protection of fishing and other coastal rights.

1.1 Motivation

Currently, the WG is remotely operated via a satellite link, using Global Positioning System (GPS) way-points, a speed logger, and a compass. As there is limited power available for the electronics, communications must be kept to a minimum. This presents a challenge given the harsh environment of the Southern Ocean. This is ultimately a limitation to the autonomy of the platform, as it largely relies on human control through a limited communication channel.

What is more, the platform tends to veer off its desired path due to the effects of waves, currents,

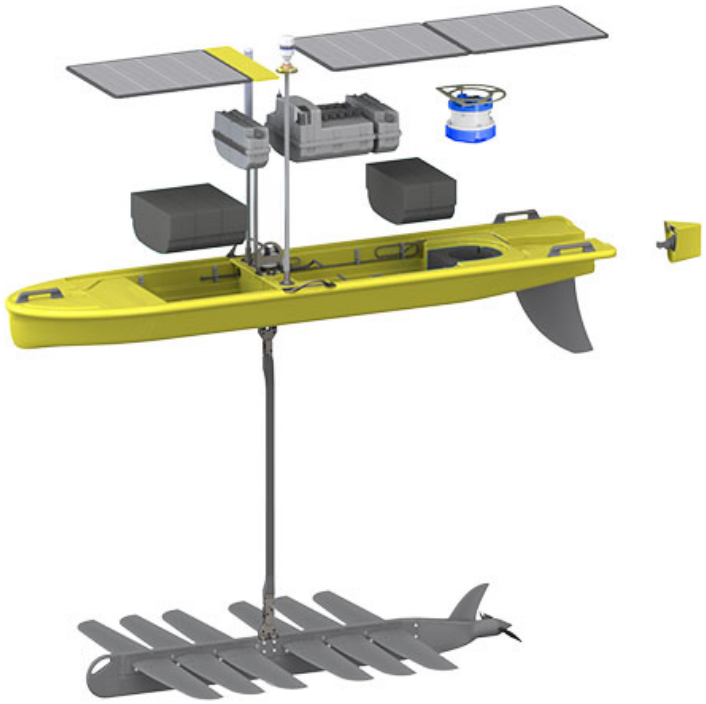

Figure 1.1: Liquid Robotics' Wave Glider SV3 model, showing payload units and solar panels separately (taken from [8]).

and other disturbances. This is largely dealt with in the global navigation strategy employed, using estimation and compensation techniques [9]. However, local sea state information is not taken into consideration by these approaches, hence energy extraction from the sea waves is not optimal. Taking a step towards autonomy requires more sophisticated navigation algorithms, operating on a per-wave strategy, which may improve accuracy along a specified path and maximise the energy uptake from the waves. To realise these improvements, local wave behaviour must be predicted a few wave cycles ahead of time. As the goal is estimation of the local behaviour, the strategy should be implemented on the available inertial measurement units on-board the platform.

1.2 Problem Description

Sea state estimation using unmanned marine platforms is an ongoing area of research [10]. Traditional means make use of Fast Fourier Transforms (FFT) on board wave rider buoys [11–14]. However, this approach requires long time spans of recorded data, upwards of 30 min (200 wave cycles), to produce one set of results. Although this time scale is acceptable for oceanographic purposes such as weather prediction, a much shorter time scale (less than approximately 0.2 min) is required for local trajectory generation and online tracking. Hence for local wave prediction, FFT methods are unsuitable. Alternative strategies make use of Kalman filters and other time domain estimation techniques to achieve this improvement [15].

1.3 Objectives

1. Develop a simple WG dynamic model and ocean wave generator, to be used for verification of the estimation strategy.
2. Develop a sea state estimator that can integrate inertial platform measurements, and predict the short term, local wave behaviour (wave height and angle of arrival estimates), a few wave cycles ahead.

1.4 Scope and Limitations

- The focus of this study is on WG platforms operating in the Southern Ocean, away from any coast. This fulfils the deep sea wave and long fetch conditions required for ocean models used. Fetch is the distance over which wind blows with a constant velocity.
- Development of estimation strategies is the focus of this study. Hence, only a fundamental model of the platform will be derived for the purpose of verifying performance of the estimator. There will not be detailed development of the dynamic model, such as calculation of drag coefficients, added mass, e.t.c.
- The sea state estimator developed must model the ocean behaviour in order to provide predictions. Integrating a dynamic model of the WG into the estimator, although not necessary, would provide benefits over modelling only the ocean behaviour. As this is a preliminary study, the WG dynamic model is not included in the estimation scheme within the scope of the current project.
- Development of navigational algorithms making use of local sea state information is not part of the present work. The focus is on providing the sea state information required by these algorithms.

1.5 Expected Outputs

Within the scope and limitations noted, the expected outputs of this dissertation are as follows:

- Two dimensional (2D) dynamic model of the WG platform.
- Ocean wave generator making use of spectral models.
- Filter based sea state estimator using the WG's inertial sensors as measurements, providing wave height estimates. In addition, it will estimate the angle of arrival, which is the mean direction from which the waves encounter the platform.

1.6 Overview of the Dissertation

In Chapter 2, a review of the most relevant literature concerning sea state estimation on mobile marine platforms is presented. It explores the current state of the art in terms of dynamic modelling of the WG platform, outlining assumptions that have been made to achieve practical

models. Moreover, some important concepts that are continually referenced in the text are briefly described in this chapter.

Following this in Chapter 3, the WG platform is discussed in more detail, and a 2D dynamic model is developed. This entails a kinematic description of the platform, and dynamic modelling. After developing a platform model, the next step taken is to describe ocean dynamics. Chapter 4 firstly details the stochastic wave models used to describe ocean behaviour. Once this is done, a wave generator model is developed, for use in simulating ocean waves that will be used to verify the performance of both the WG dynamic platform, and the subsequent sea state estimator.

The ocean waves dynamics chapter lays the groundwork for two critical chapters that follow it. Chapter 5 and 6 encompass the estimation approach taken, which involves taking a close look at spectral estimation, and filtering for wave height prediction. An overview of the simulation procedures and experimental work conducted for verification of the developed systems is given in Chapter 7, before the results of these experiments are presented. Finally, the results obtained are analysed in the discussions along with concluding remarks and recommendations in Chapter 9.

Research done in this dissertation not central to the main estimation approach is presented in the appendix. Of note is Appendix C, which explains some of the mathematical operations used in the text. In addition, all citations, chapter and equation references are hyper-linked for convenient navigation of the document.

Chapter 2

Literature Review

In this section, the operating principle of the Wave Glider (WG) is presented, including existing research work. Following this, background information concerning modelling of the platform and ocean behaviour will be discussed in detail. Finally, the background on estimation techniques will be described.

2.1 The Wave Glider Platform

The WG is a hybrid system, having both a surface component as well as an underwater component. It consists of two rigid bodies connected by a flexible tether; a float housing the electronics payload and a submerged glider with mechanical fins and a rudder for directional control. Fig. 2.1 shows the operation of the WG SV3, the third iteration of the platform. This model is equipped with a battery powered thruster for steering.

Wave energy harvesting is therefore essential for propulsion. As the buoyant float is raised by a wave, the glider is pulled up causing the fins to orient themselves in such a way that the glider experiences a forward thrust. As float falls due to a trough in the wave profile, the difference in buoyancy and weight of the float and glider pulls the WG down, and the fins change orientation and a forward thrust is again experienced. Hence positive and negative motion in the vertical plane gives forward propulsion in the horizontal plane.

2.1.1 Previous Work

With the increased presence of UUVs and USVs at sea, a wealth of knowledge has been accumulated about the modelling of mobile marine platforms, and their subsequent use in maritime activities [16]. Previous studies have developed dynamic models of the hybrid system, using Lagrangian dynamics [17], and estimated various aspects of the sea state. This modelling approach is adopted in this text.

For a global navigation goal, prediction of the speed of a WG platform has been achieved using long time-scale wave height recordings from the National Oceanic and Atmospheric Administration (NOAA) [18]. These wave height recordings are taken using wave buoys at sea. It follows a machine learning approach with a two degree of freedom (DOF) WG model, fed by significant wave height and peak frequency as input data. Results from this investigation show that using NOAA data does not give good results, due to lack of correlation between where measurements

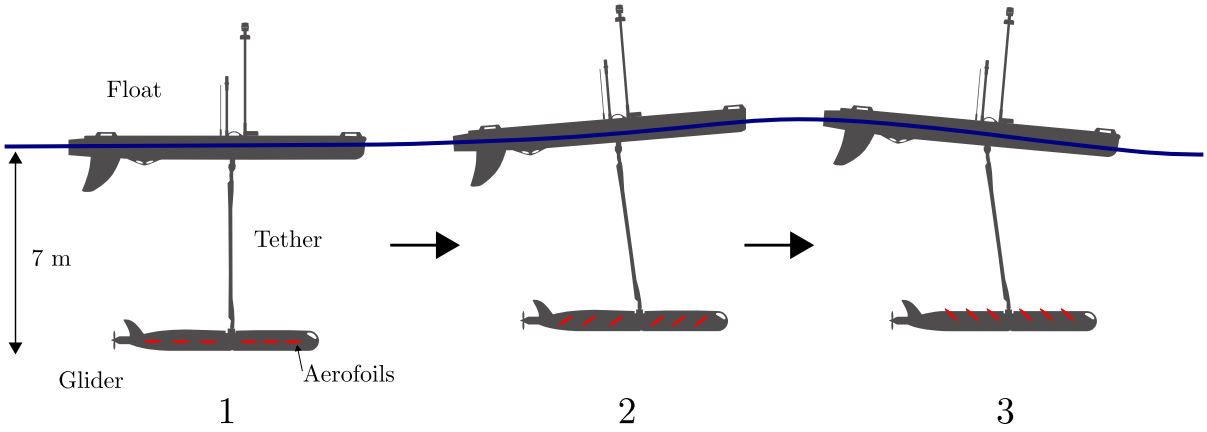

Figure 2.1: Wave Glider SV3 model in the three states of operation: (from left) 1. With a flat sea condition, the glider experiences no forward thrust and WG is stationary. 2. Positive heave pulls the buoyant float up, which also pulls up the glider via the tether. This upward pull results in a forward thrust due to the fins changing their orientation. 3. As WG goes into wave trough, weight of glider pulls down. Forward thrust is again achieved as fins change orientation (modified from [8]).

taken and where they are recorded. Therefore a conclusion of the study is that better results can be obtained using on-board sensors.

In another study, the direction wave spectrum is estimated by likening wave responses of a ship to those of a wave buoy [19]. The direction wave spectrum shows the mean direction that wind waves come from, commonly caused by distant storm systems. Although the platform used in this study is a ship, the approach of likening the platform to a wave buoy makes it possible to uses inertial sensors for sea state estimation. A similar analogy can be used in the case of the WG, to simplify modelling of the complex interaction between the platform and ocean dynamics.

2.1.2 Dynamic Modelling of the Wave Glider Platform

For improved estimation capabilities, a relatively detailed model of the platform is necessary. Such a model will allow for the discrepancy between measured responses and actual sea motions caused by the natural filtering of the platform to be accounted for, resulting in more accurate sea state estimates. Response amplitude operators (RAOs) are commonly used in translating responses to sea wave spectra [16, 20]. These are transfer functions that determine vessel behaviour due to certain sea state conditions, usually calculated for different ship motions and headings using computational fluid dynamics (CFD) methods. An alternative to using RAOs in conjunction with CFD is calculating vessel responses in real-time, using a detailed dynamic model of the platform derived through Lagrangian or Newton-Euler modelling.

Before the complex wave glider model is used in the sea state estimation process, a simpler model is used to verify correct operation of other estimation components. As such, a simpler model can be obtained by likening the platform to a wave rider buoy that can only heave, pitch, roll and yaw. This modelling approach has been taken in previous studies to simplify complicated dynamics of large vessels in sea state estimation [13]. Once the estimation has been verified, a dynamic model of the WG can be integrated.

As the WG is a hybrid system, developing a model is challenging as there are detailed modelling guides on either a fully submerged marine vehicle, or a regular surface vehicle. Limited in-depth modelling analysis exists for hybrids. Fossen [21] has separate detailed dynamic model derivations for single body surface vessels and for fully submerged vessels. Components of each of the models are utilised to develop a model for the WG.

2.2 Ocean Dynamics

Although at first glance, the vertical motion of the ocean surface seems unstructured and irregular, rigorous models have been developed to describe it as a superposition of simple harmonic sinusoids [22–26]. Fig. 2.2 (1) shows a regular wave train, which is not a true representation of the sea, as waves have a random aspect to them. Randomising the phases of the harmonics gives Fig. 2.2 (2), which is an irregular long-crested wave train. In reality, waves are best represented by Fig. 2.2 (3). These are termed short-crested waves, where in addition to random phases of the components, there is a spatial spreading of the waves that produces short peaks [27].

When describing ocean waves as a sum of harmonic sinusoids, it is more convenient to use the frequency domain to analyse ocean waves. That is, looking at the amount of energy contained in the waves at different frequencies.

2.2.1 The Ocean Wave Spectrum

Ocean waves can be separated into distinct categories, which occupy different sections of the ocean wave spectrum, shown in Fig. 2.3. Beyond the region of interest, at the lowest end of the spectrum, waves present in the oceans are tidal waves and seiches. Between 0.1 Hz to 3 Hz are wind-generated gravity waves which can be separated into three subcategories; swell, wind seas and capillary waves. This section of the ocean wave spectrum is the region of interest.

Power Spectral Density

The representation in Fig. 2.3 shows the amount of energy contained by ocean waves at different frequencies. As spectral representation is repeatedly used in this text, the concept of a power spectral density (PSD) is important to mention. It is defined as the Fourier transform of the

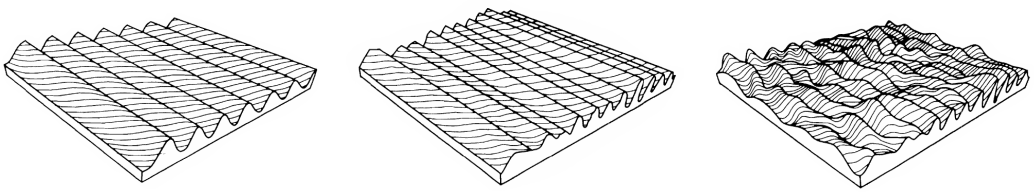

1. Uniform waves 2. Long crested random waves 3. Short crested waves

Figure 2.2: Three types of wave profiles: 1. Uniform waves, single frequency component from one direction. 2. Long crested random waves, multiple frequency components from one direction. 3. Short crested waves, multiple frequency components from multiple directions result in this type of sea state (modified from [27]).

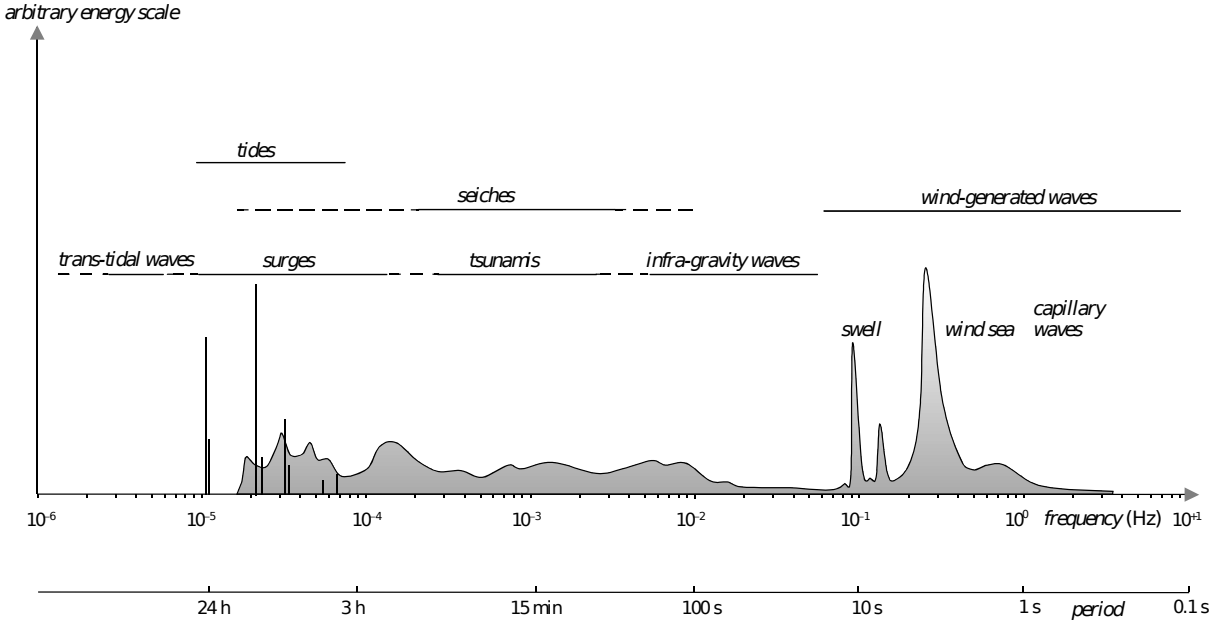

Figure 2.3: Full ocean wave spectrum showing frequencies and periods of the ocean surface's vertical motions. The region of interest is the wind sea portion of the wind generated waves (taken from [24]).

stationary auto-correlation function, $R(\tau)$, of the sea surface elevation [24, 28].

$$R(\tau) = E\{h(t)h(t-\tau)\}, \tag{2.1}$$

$$S(\omega) = \int_{-\infty}^{\infty} R(\tau)e^{-j\omega\tau}\mathrm{d}\tau, \tag{2.2}$$

taken on a finite time interval, $[-T, T]$. This is known as the Wiener-Khinchine Theorem, and allows use of the PSD to assess performance of the designed estimators off-line.

2.2.2 Wind Generated Ocean Waves

Linear wave theory is used to describe wind generated surface gravity waves [26]. This theory applies to water with idealised physical properties and with gravity as the only external force, explaining in detail the harmonic waves used in the stochastic description of the ocean. Linearity implies that the harmonics do not interact with one another as they propagate [24].

There are three types of waves in the wind-generated subcategory of ocean waves: capillary, wind sea, and swell waves. Their wavelengths range from a few centimetres to approximately 250 m.

Capillary waves are excluded from the study as their wavelength, at less than 10 cm, are shorter than the WG float dimensions [24]. The response of the float will be to filter out these short wavelength waves. Moreover, these waves dissipate quickly and hence are not useful for the navigation goal.

Wind seas have wavelengths ranging between 60 m to 150 m, and contribute a significant amount of energy in a narrow frequency band, shown in Fig. 2.3. This range is ideal for local trajectory planning, hence these waves are the focus of this study.

Capillary and wind sea waves occur in close proximity to the wind source. Further away, swell waves are formed as a result of this wind source. They are regular and rarely change direction, with wavelengths of approximately 250 m. Due to their low frequency, the vertical rate of swell waves is low and therefore they do not contribute much to the wave glider propulsion which is of interest. For these reasons, swell waves fall outside the region of interest, and hence they are not considered in this study.

Stationarity, Ergodicity, and Homogeneity of Ocean Waves

Random processes are used to describe all possible ocean wave realisations [24, 28]. They are formulated as wave models that generate wide-sense stationary (Gaussian) processes in time. A stochastic process is said to be wide-sense stationary if its mean and autocovariance are time invariant [28].

For these models to match the behaviour shown in Fig. 2.2 (3) adequately, ocean waves must also be stationary processes, which is not the case over long time intervals. However, by limiting the time horizon to less than 30 min, they can be considered approximately stationary, making this modelling approach valid under this condition [24]. In addition, the stochastic processes used must also meet the condition of ergodicity, meaning that averaging in time is equivalent to averaging an ensemble of experiments conducted [28]. Therefore, from one realisation, ergodicity implies that all statistical properties of the waves can be extracted.

Analogous to stationarity is homogeneity, which applies to the spatial dimensions. This condition must also be met when considering an area of the ocean surface to be governed by a stochastic process. As such, it is met within small space scales of approximately 10 km for wind generated ocean waves [24].

Ocean Wave Models

Under ideal conditions, the ocean wave frequency spectrum has a constant shape. Experiments have been conducted to determine an empirical expression for this shape. For the wind seas section of wind generated waves, the two prominent models used are the Pierson-Moskowitz (PM) and JONSWAP, shown in Fig. 2.4. The former is used for fully developed seas, whereas the latter is used for the transitional period towards full development [24, 29]. When the speed of the longest waves matches the wind speed, growth of waves slows down, and is referred to as a fully developed sea. At this stage, the local sea state is independent of the distance wind has blown over (fetch distance), and allows the wind to be used as the single parameter in the spectrum. The general form of the PM spectrum is

$$S(\omega_i) = \frac{A}{\omega_i^5} \exp\left(- \frac{B}{\omega_i^4} \right), \tag{2.3}$$

where A and B are calculated as shown in Eq. 2.4 and 2.5, with empirically derived, dimensionless constants, $\alpha = \ 8.1 \times 10^{-3}$, and $\beta = \ 7.4 \times 10^{-1}$ [29, 30].

$$A = \alpha g^2, \tag{2.4}$$

$$B = \beta \omega_0^4, \tag{2.5}$$

$$\omega_0 = g/U_{19.5}. \tag{2.6}$$

The PM spectral description is useful as it is parametrised by only one variable, $U_{19.5}$. This is the wind-speed at 19.5 m above the mean ocean surface, the height at which wind measurements were taken during the experiment. JONSWAP is a modification of the PM spectrum that enhances it to improve the fit when waves are not fully developed [30], expressed as

$$S_j(\omega_i) = S(\omega_i)\gamma^r, \tag{2.7}$$

where γ^r is the peak enhancement factor. In fetch limited conditions, the JONSWAP spectrum is a better fit, fetch being the distance over which wind blows with a constant velocity. When fetch is limited, seas do not fully develop.

$$\gamma = 3.3, \tag{2.8}$$

$$r = \exp\left[-\frac{(\omega - \omega_p)^2}{2\sigma^2\omega_p}\right], \tag{2.9}$$

$$\sigma = \begin{cases} 0.07, & \omega \leq \omega_p \\ 0.09, & \omega > \omega_p. \end{cases} \tag{2.10}$$

For the JONSWAP spectrum, the dimensionless constants obtained empirically are described as

$$\alpha_j = 0.0317\omega_p^{0.67}, \qquad \beta_j = \frac{5}{4}, \tag{2.11}$$

where ω_p is the peak frequency. The difference of the peak enhancement factor results in the JONSWAP spectrum having a much higher value at the peak frequency than the PM spectrum, depicted in Fig. 2.4.

From statistical methods used to describe sea waves, useful ocean wave simulations have been developed [31, 32]. Fig. 2.5 is a two dimensional slice showing how the complex appearance of ocean waves can be constructed by adding together a large number of sinusoidal components (frequencies) with random amplitudes, and phases, with respect to each other [26]. A PM spectral model is used to produce this realisation.

Wave Dispersion Relationship and the Deep Sea Condition

Surface gravity waves have a relationship linking their temporal and spatial propagation at any point in the wave field. Referred to as the wave dispersion relation, it is expressed as

$$\omega_i^2 = g|\vec{k}_i| \tanh(|\vec{k}_i|D), \tag{2.12}$$

where g is the acceleration due to gravity, while ω_i, and $|\vec{k}_i| = k_i$, are the respective temporal and spatial frequencies for a wave component, i. The spatial frequency, k_i, is also referred to as the wave number, expressed as

$$k_i = \frac{2\pi}{\lambda_i}, \tag{2.13}$$

where λ_i is the physical wavelength of a wave component. D in Eq. 2.12 is the depth to the ocean floor from the mean water level. When D is greater than half the longest wavelength present in the spectrum ($D > \lambda/2$), waves are defined as deep water waves. This allows a simplification of Eq. 2.12 to be made, since $\tanh(k_i D) \approx 1$, resulting in the dispersion relationship

$$\omega_i^2 \approx g k_i. \tag{2.14}$$

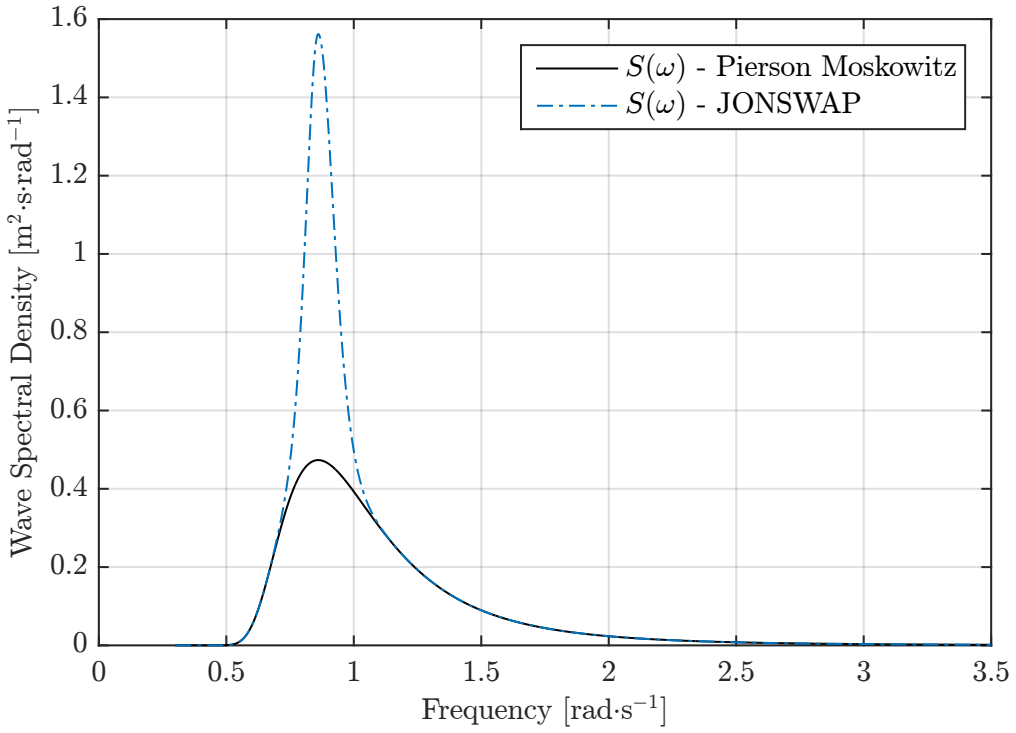

Figure 2.4: Pierson-Moskowitz and JONSWAP wave spectra for $U = 10\,\mathrm{m} \cdot \mathrm{s}^{-1}$. A peak enhancement factor, γ^r, causes the JONSWAP spectrum to have a much higher peak than the PM spectrum (modified from [24]).

2.3 State Estimation

The wave height spectrum at any point is spread over a range of frequencies. This spectrum can be obtained using the attitude and position of the WG on the sea surface. This is analogous to estimation of wave height and direction by three dimensional (3D) wave buoys [12]. For attitude estimation of the WG, the sensors available are a magnetometer and IMU. All measurements used are assumed to have additive Gaussian noise. Additionally, the acceleration and gyroscope measurements are assumed to have additional time-varying biases that must be estimated alongside the other states. Developing a sea state estimation strategy based on sensors commonly found on most marine platforms is advantageous, as the estimator can be extended easily and used on any platform with these sensors.

Parametric and Non-Parametric Estimation

Previous work has investigated attitude estimation techniques for a USV using IMU, GPS and compass measurements. One approach makes use of an EKF to estimate the position and attitude of the body in the body-fixed frame, $\{b\}$, with respect to the inertial North-East-Down (NED) frame, $\{n\}$ [33]. This is a purely kinematic approach, using only the IMU measurements for state propagation in the EKF while the GPS and compass measurements are used for corrections. For the WG, a similar approach to this would be to integrate the accelerations and angular rates obtained from an IMU to propagate the states, and to correct using magnetometer and GPS updates.

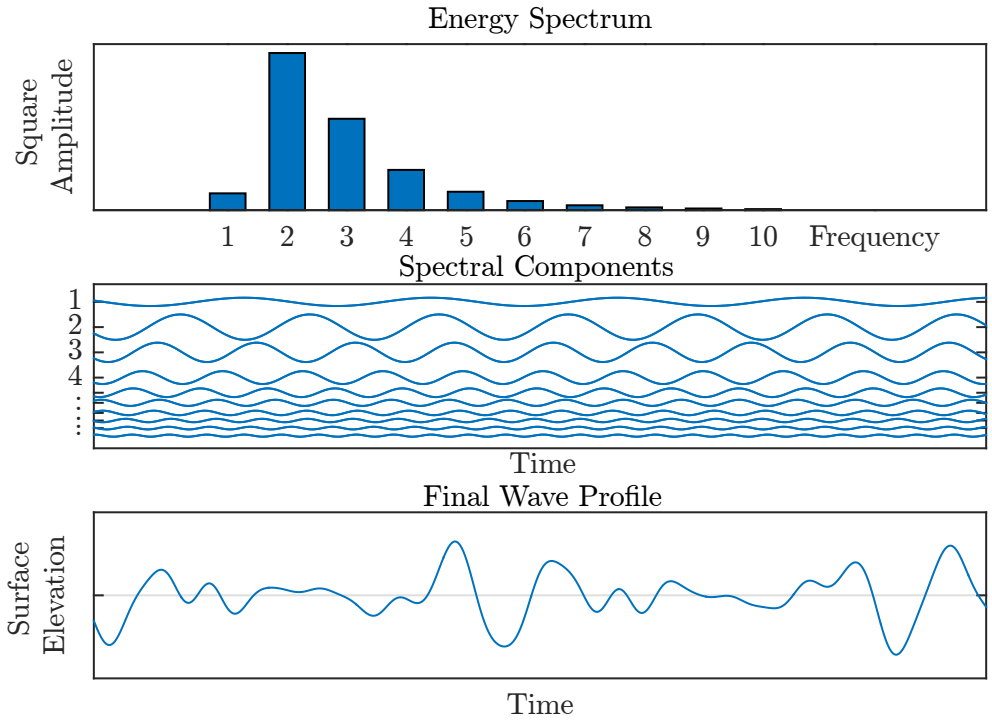

Figure 2.5: (Top) Magnitude of spectral components, forming a wind wave spectral shape; (Middle) Spectral components plotted as a function of time, with different phases; (Bottom) Resulting surface elevation from superposition of the spectral components (modified from [30]).

As this approach only makes use of measurements available without considering ocean behaviour, it is termed a non-parametric approach. To aid the estimation, a parametric approach can be taken. This makes use of an estimated wave spectrum and dynamic model to advance the states, while all the measurements are used as updates.

2.3.1 Sea State Estimation

In ocean engineering, the sea state is commonly characterised by three parameters; the significant wave height, H_s, mean wave period, and wave direction. The sea state can also be presented by describing the wave spectrum, which is a combination of the three parameters.

Estimation of the significant wave height, wave period, and wave direction has long been implemented on wave rider buoy platforms [12]. These buoys are fixed in position by a stabilization mooring. To measure wave height, the buoy uses an accelerometer oriented vertically. This particular buoy is stabilised in such a way that the platform remains almost horizontal under any extreme movement [12]. This simplifies the estimation of the wave height as rotations of this acceleration are not considered.

Wave buoys are limited in number and are not always able to provide estimates at the desired location, particularly in close proximity of the mobile platform in question. As a result, the sea state estimation methods used on wave buoys have been adapted and employed on a variety of other marine platforms, including ships and surfaced UUVs [10, 19]. The WG is considered analogous to a wave buoy floating on the surface, and dynamic modelling of the platform could

be used to take care of discrepancies in the wave response.

Similar research uses filtering approaches to estimate sea state parameters on large vessels with significant forward velocity, which must take into consideration the triple-valued function problem that arises from distortion in wave frequencies due to the Doppler effect [13]. In practice, the upper limits of the WG's speed is close to $1\,\mathrm{m}\cdot\mathrm{s}^{-1}$, and this is slow enough to consider the platform as being practically stationary, hence avoiding the triple value problem altogether.

H_s is not estimated directly as it is an averaged value that requires a long time span for calculation. It is only calculated off-line for comparison to existing models as it is not useful for the real-time nature of the estimator.

FFT based Methods

The sea wave spectrum is obtained following the Fast Fourier Transform (FFT) method on wave rider buoys, and more recently, on a surfaced UUV [10, 11]. A disadvantage of this approach is the long time span of recorded data that is required to calculate sea state parameters, taking upwards of 30 min (200 cycles) to produce one set of results.

For oceanographic purposes such as weather prediction, this time scale is acceptable. However, this is not useful for local trajectory generation for navigation and online tracking, which requires shorter time scales between 0.1 min to 2 min.

2.3.2 State Estimation

An alternative strategy for spectral and sea state estimation is to use a Kalman filter (KF) which minimises error between a model and measured variables (that depend on the temporal and spatial sea surface elevation). In previous work, off-line Kalman filtering has been used to estimate the direction spectrum for spectral updates, under fast changing sea state conditions, with the goal to use this information for advisory support, guidance and control systems. The time scale achieved ranges from 3 min to 10 min [15]. Although this is an improvement on the FFT method, it does not match the required time scale for prediction.

Kalman Filtering for the Best Linear Unbiased Estimates

Processing noisy measurement data and obtaining unbiased estimates of the sea state and other variables can be achieved using a Kalman filter. In the state model form, the continuous time random process is described as

$$\dot{\boldsymbol{z}} = F\boldsymbol{z} + B\boldsymbol{u}, \tag{2.15}$$

$$\boldsymbol{y} = H\boldsymbol{z} + D\boldsymbol{u}, \tag{2.16}$$

where F, B, H, and D are matrices, while u is a column vector of zero mean, unity variance white noise [28]. The vector state of the process is $\boldsymbol{z}$. From Eqs. 2.15 and 2.16, the discrete time model used in the estimation is derived in later chapters. Additionally, an Extended Kalman Filter (EKF) formulation, as shown in Eqs. 2.17 and 2.18, is used when either the process model

or measurement model contains nonlinearities.

$$\dot{\boldsymbol{z}} = f(\boldsymbol{z}, \boldsymbol{u}) + \mathrm{w}_k, \tag{2.17}$$

$$\boldsymbol{y} = g(\boldsymbol{z}) + \mathrm{v}_k, \tag{2.18}$$

where $f(\boldsymbol{z}, \boldsymbol{u})$ and $g(\boldsymbol{z})$ are the nonlinear state transition and measurement models, while w_k and v_k are zero mean noise vectors. Taking the partial derivatives of the state transition and measurement models with respect to the state vector in the EKF formulation gives the matrices

$$F = \frac{\partial f(\boldsymbol{z}, \boldsymbol{u})}{\partial \boldsymbol{z}}, \tag{2.19}$$

$$H = \frac{\partial g(\boldsymbol{z})}{\partial \boldsymbol{z}}. \tag{2.20}$$

The discrete time equivalents of Eqs. 2.17 and 2.18 are used in the filter, defined as

$$\boldsymbol{z}_{k+1} = f(\boldsymbol{z}_k, \boldsymbol{u}_k) + \mathrm{w}_k, \tag{2.21}$$

$$\boldsymbol{y}_k = g(\boldsymbol{z}_k) + \mathrm{v}_k, \tag{2.22}$$

where $\boldsymbol{z}_k$ is the process state vector at time t_k, while the measurement vector at time t_k is $\boldsymbol{y}_k$. The process noise and measurement error are w_k and v_k respectively [28]. Both w_k and v_k are assumed to be zero mean, with covariance matrix Q_k for the process, and R_k for the measurement, shown in Eq. 2.23 and 2.24 respectively.

$$E\{\mathrm{w}_k \mathrm{w}_i^T\} = \begin{cases} Q_k, & i = k \\ 0, & i \neq k \end{cases} \tag{2.23}$$

$$E\{\mathrm{v}_k \mathrm{v}_i^T\} = \begin{cases} R_k, & i = k \\ 0, & i \neq k \end{cases} \tag{2.24}$$

The discrete time EKF formulation can be represented by Eq. 2.25, where e^{FT} is the state transition matrix. The first two terms in the expansion of e^{FT} are taken in Eq. 2.26 to give an approximation of the state transition matrix, F_k [34]. The continuous measurement model, H, is also discretised to result in the discrete measurement matrix, H_k, in Eq. 2.28.

$$\boldsymbol{z}_k = e^{FT} z_{k-1}, \tag{2.25}$$

$$e^{FT} = (I + FT + \frac{1}{2}F^2T^2 + \dots) \approx I + FT = F_k, \tag{2.26}$$

$$\boldsymbol{z}_{k+1} = F_k \boldsymbol{z}_k + \mathrm{w}_k, \tag{2.27}$$

$$\boldsymbol{y}_k = H_k \boldsymbol{z}_k + \mathrm{v}_k. \tag{2.28}$$

From this, the recursive Kalman filter loop is formulated as shown in Algorithm 1. The inputs are the a priori estimate, $\hat{\boldsymbol{z}}_k^-$, and the corresponding a priori error covariance, P_{k+1}^-. The Kalman gain, K_k, is calculated on line 4 of the algorithm, after which the update stage of the filter is carried out on lines 7 and 10. The final stage before the filter loops back is the prediction of the next values, carried out on lines 13 and 14.

The Simple Oscillator

An important concept used in several sections of this work is the simple harmonic oscillator, depicted in Fig. 2.6. It can be represented by a second order differential equation, such that

Algorithm 1 Kalman filter loop

procedure KALMANFILTER($\hat{\boldsymbol{z}}_k^-$, P_{k+1}^-)
  while 1 **do**
    // Compute the Kalman gain.
    $K_k = P_k^- H_k^T (H_k P_k^- H_k^T + R_k)^{-1}$

    // Update estimate with measurement y_k.
    $\hat{\boldsymbol{z}}_k = \hat{\boldsymbol{z}}_k^- + K_k(\boldsymbol{y}_k - H_k \hat{\boldsymbol{z}}_k^-)$

    // Compute error covariance for updated estimate.
    $P_k = (I - K_k H_k) P_k^-$

    // Project sate and error covariance ahead.
    $\hat{\boldsymbol{z}}_{k+1}^- = F_k \hat{\boldsymbol{z}}_k$
    $P_{k+1}^- = F_k P_k F_k^T + Q_k$
  end

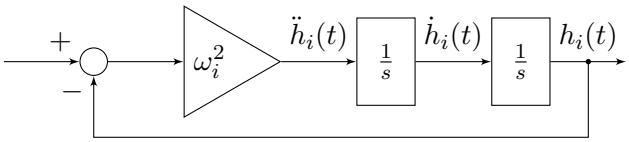

Figure 2.6: A standard implementation of an oscillator, producing continuous oscillations with constant amplitude once initiated.

$$h_i(t) = A\sin(\omega_i t + \gamma_i), \tag{2.29a}$$

$$\dot{h}_i(t) = A\omega_i \cos(\omega_i t + \gamma_i), \tag{2.29b}$$

$$\ddot{h}_i(t) = -A\omega_i^2 \sin(\omega_i t + \gamma_i) = -\omega_i^2 h_i(t). \tag{2.29c}$$

The amplitude of oscillations is A, while ω_i is the frequency, and γ_i is the phase relative to other oscillators [22]. In this form, the oscillator propagates indefinitely at the same amplitude. With the addition of a damping term, ζ_i, the amplitude of oscillations can either increase or decrease depending on the damping term's sign,

$$\ddot{h}_{\omega_i}(t) = -2\zeta_i \omega_i \dot{h}_i(t) - \omega_i^2 h_i(t). \tag{2.30}$$

This behaviour is similar to relaxation oscillators commonly used in electronic design [35].

Peak Frequency Estimation

The oscillator in Fig. 2.6 can be used to represent estimation of a sinusoid with unknown magnitude, phase and frequency [36, 37]. It is convenient to express the system above as three simultaneous first order differentials, as

$$\dot{z}_1 = z_2, \tag{2.31a}$$

$$\dot{z}_2 = -\omega^2 z_1 = -z_3 z_1, \tag{2.31b}$$

$$\dot{z}_3 = 0, \tag{2.31c}$$

where $z_1 = h_i$, $z_2 = \dot{h_i}$, and $z_3 = \omega_i^2$ [22]. The z_3 state is modelled as a random walk process, with zero mean noise w_{3k} [36]. If it is not slow varying, the loop will become highly nonlinear due to the term $z_3 z_1$ in Eq. 2.31b. This limitation is added as a design constraint when tuning the Kalman filter. These sets of equations can be written in state space form as

$$\dot{\boldsymbol{z}} = F\boldsymbol{z}, \tag{2.32}$$

$$\dot{\boldsymbol{z}} = \begin{bmatrix} 0 & 1 & 0 \\ -z_3 & 0 & 0 \\ 0 & 0 & 0 \end{bmatrix} \boldsymbol{z}. \tag{2.33}$$

Taking the partial derivative of the state transition matrix, F, in Eq. 2.33 results in

$$\frac{\partial F}{\partial \boldsymbol{z}} = \begin{bmatrix} 0 & 1 & 0 \\ -z_3 & 0 & z_1 \\ 0 & 0 & 0 \end{bmatrix}. \tag{2.34}$$

Discretising Eq. 2.34 by taking the two term approximation shown in Eq. 2.25, with T as the sampling period results in F_k, such that

$$\boldsymbol{z}_k = e^{FT} z_{k-1} \approx (I + FT) z_{k-1}, \tag{2.35}$$

$$\boldsymbol{z}_k \approx \left(\begin{bmatrix} 1 & 0 & 0 \\ 0 & 1 & 0 \\ 0 & 0 & 1 \end{bmatrix} + \begin{bmatrix} 0 & 1 & 0 \\ -z_3 & 0 & -z_1 \\ 0 & 0 & 0 \end{bmatrix} T \right) \boldsymbol{z}_k, \tag{2.36}$$

$$\boldsymbol{z}_k = \begin{bmatrix} 1 & T & 0 \\ -z_3 T & 1 & -z_1 T \\ 0 & 0 & 1 \end{bmatrix} \boldsymbol{z}_{k-1} + \begin{bmatrix} \mathrm{w}_{1k} \\ \mathrm{w}_{2k} \\ \mathrm{w}_{3k} \end{bmatrix}, \tag{2.37}$$

where w_{1k}, w_{2k}, and w_{3k} are the noise values for the respective states [34].

2.4 Assumptions Used in Theory and Modelling

From previous work on WG modelling and sea state estimation, assumptions have been made to simplify the formulation. In this text, these assumptions are evaluated and where possible, they will be discarded and handled with a more rigorous modelling approach.

2.4.1 Wave Glider Modelling

In modelling the WG-sub hybrid, Caiti et al. [17] made the assumption that the float and glider are rigid bodies with constant masses. As the payload is fixed on the WG, its centre of mass can be considered static, although possibly uncertain from one deployment to the next as the equipment used is mission dependent. To add to this, bio-fouling alters the mass of the vessel over time but is considered to be minimal.

Moreover, the tether linking the WG float and glider is considered to be in tension at all times, and lightweight. Hence it is modelled as a massless rigid body. This assumption is valid as the glider is much heavier than the float, which keeps the tether in tension most of the time. Tian et al. [38] made similar assumptions.

Kraus [9], in a masters dissertation, modelled a previous generation of the WG, making an assumption that the centre of mass is located in the middle of the tether. In addition, the whole system is modelled as a rigid light bar with two masses at either end, that can only yaw. This assumption is not used, as the modelling approach will be to consider the WG as three rigid bodies (each with their own mass) coupled by constraints.

2.4.2 Ocean Dynamics

The effect of swell is not considered in this investigation as these waves are assumed to have a negligible impact on the propulsion and short-term navigation of the WG. Hence only uni-modal wind wave spectra are considered in this work. This assumption is valid as these waves are at a low frequency, and not in the region of interest.

2.5 Literature Review Summary

This chapter covers the most relevant literature concerning sea state estimation on mobile marine platforms. Of note is the focus on spectral estimation methods that will provide prediction capabilities. Using these concepts, a dynamic model of the WG platform can now be developed, within the bounds of the assumptions just made.

This page has been intentionally left blank.

Chapter 3

The Wave Glider Model

Developing a dynamic model of the WG platform begins with defining the coordinate system used. Following this, platform dynamics are outlined, before presenting the final model.

3.1 Wave Glider Kinematics

Although not in the scope of the current project, it is envisaged that the WG model would be included in the estimation scheme. For this project, it is assumed that the WG float is at the sea-air boundary. Detailed models for single body USVs and UUVs are widely available [21]. However, this is not the case for the more complex case of UUV/USV hybrids. As such, aspects of these single body modelling approaches are used for the derivation of the multi-body hybrid system. The approach follows previous studies into dynamic modelling of the WG platform [17].

3.1.1 Notation and Coordinate Conventions

The naming conventions used in this text are derived from The Society of Naval Architects and Marine Engineers (SNAME) notation [39]. Table 3.1 shows nomenclature for the six DOF required to fully describe the orientation and motion of a rigid body. For a global fixed frame reference, the North-East-Down (NED) coordinate system is used, denoted as $\{n\}$. The body fixed frame, attached to the WG, is denoted as $\{b\}$ [21]. These frames are shown with respect to each other in Fig. 3.1.

Table 3.1: SNAME notation convention for the motion of marine vehicles [39].

DOF	Forces and Moments	Velocities	Attitude and Position
Surge	X	u	x
Sway	Y	v	y
Heave	Z	w	z
Roll	K	p	ϕ
Pitch	M	q	θ
Yaw	N	r	ψ

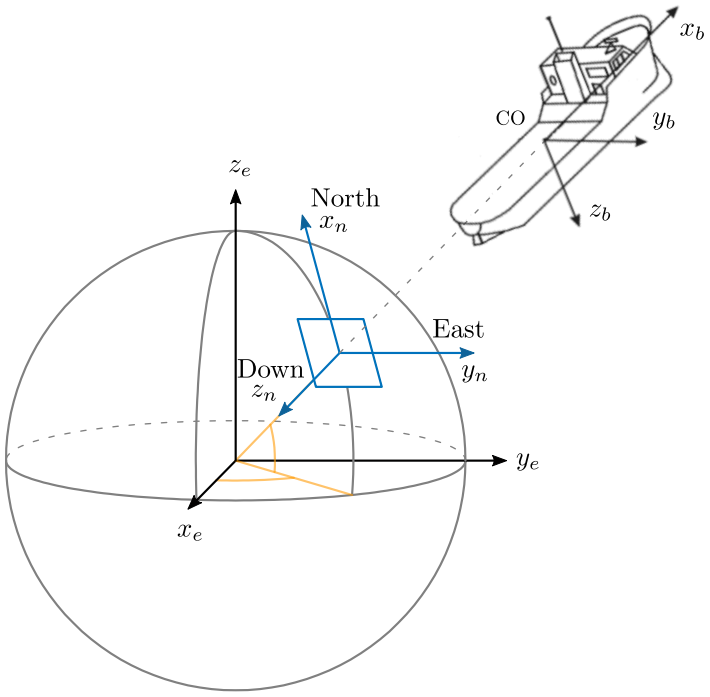

Figure 3.1: Earth Centred Earth Fixed (ECEF), North-East-Down (NED), and BODY reference frame systems, in relation to one another. All three frames of reference are commonly used in marine vessel modelling, where ECEF is denoted by subscript $\{e\}$, while NED is denoted by $\{n\}$, and BODY by $\{b\}$ (adapted from [21]).

3.1.2 Motion of a Rigid Body

Generalised Coordinates

The WG consists of two rigid bodies. To describe the position and orientation of the WG relative to a coordinate frame, twelve DOFs are required (six for each body). As these bodies are connected together by the tether, constraint equations can be used to link the coordinates to one another [17]. Using these constraints, the twelve DOFs can be represented by a smaller set of independent coordinates, known as generalised coordinates, and used to describe the WG [40].

The generalised coordinates used for the WG are the float position in the surge and heave axes, x_n and z_n respectively, and the float, tether, and glider orientation about the sway axis. These are θ_1, θ_2, and θ_3 respectively. This results in the generalised coordinate vector, $\vec{q}$, as

$$\vec{q} = \begin{bmatrix} x_n, & z_n, & \theta_1, & \theta_2, & \theta_3 \end{bmatrix}^T . \tag{3.1}$$

The remaining coordinates can always be calculated from this set of generalised coordinates using the constraint equations and coordinate transformations. Eq. 3.3 is used to calculate the

generalised velocities, $\vec{v}$, for a joint, $\vec{p}$, as

$$\vec{p} = p(\vec{q}, t), \tag{3.2}$$

$$\vec{v} = \frac{\mathrm{d}\vec{p}}{\mathrm{d}t} = \frac{\partial \vec{p}}{\partial \vec{q}}\frac{\mathrm{d}\vec{q}}{\mathrm{d}t} + \frac{\partial \vec{p}}{\partial t}\frac{\mathrm{d}t}{\mathrm{d}t}, \tag{3.3}$$

$$\frac{\mathrm{d}\vec{q}}{\mathrm{d}t} = \begin{bmatrix} \dot{x}_n, & \dot{z}_n, & \dot{\theta}_1, & \dot{\theta}_2, & \dot{\theta}_3 \end{bmatrix}^T. \tag{3.4}$$

Coordinate Transformation

The generalised coordinates of the WG can be formulated as a kinematic chain. Considering the WG as a serial link of rigid bodies allows it to be modelled using the same Lagrangian dynamic modelling approach taken for a multi-body pendulum. To describe this kinematic chain in a systematic way, the Denavit-Hartenberg (DH) convention is used [40].

The advantage of this formulation is that it provides a way to describe the pose of a platform with four parameters to relate one frame to the next. In comparison, other reference conventions use six parameters; three for translation and three for rotation [40]. The axes for the jth frame are labelled x_j, y_j, and z_j. Two adjacent frames are shown in Fig. 3.2, parametrised using DH. The four DH parameters used to reference two adjacent frames are as follows:

- d_j: distance from z_{j-1} to the common normal of the two frames (link length),
- θ_j: angle about z_{j-1}, from x_{j-1} to x_j,
- a_j: length of the common normal between the two frames, and
- α_j: angle about the common normal, from z_{j-1} to z_j.

Eq. 3.5 shows how these parameters are related by a homogeneous transformation, $\mathcal{T}$, from frame j, to frame $j-1$, composed of four simple transformations as

$$^{j-1}_{j}\mathcal{T} = T(z_{j-1}, d_j) \cdot R(z_{j-1}, \theta_j) \cdot T(x_j, a_j) \cdot R(x_j, \alpha_j), \tag{3.5}$$

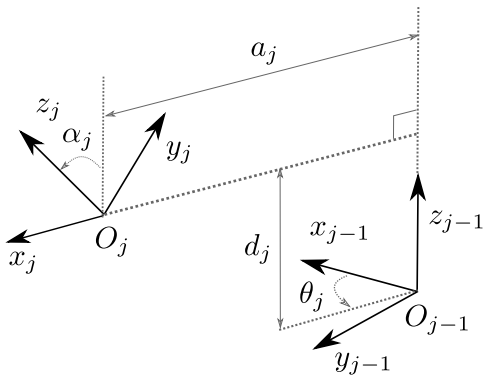

Figure 3.2: Formulation of Denavit-Hartenberg parameters, with O_j and O_{j-1} as the origin points of frame j, and frame $j-1$, respectively (modified from [41]).

where $T(z_{j-1}, d_j)$ represents a translation of length d_j along the z_{j-1} axis, while $R(z_{j-1}, \theta_j)$ represents a rotation of angle θ_j with respect to the z_{j-1} axis. For each reference frame, actuation is either along or about the z_i axis.

For each reference frame, actuation is either along or about the z_i axisFor these parameters to describe the relative pose of the frames completely, two constraints are required. Firstly, the x_j axis must be perpendicular to the preceding axis, z_{j-1}. Secondly, the x_j axis must intersect z_{j-1} [40]. The equivalent transformation can be written as

$$ {}^{j-1}_{j}\mathcal{T} = \begin{bmatrix} \cos\theta_j & -\sin\theta_j & 0 & a_j \\ \sin\theta_j \cos\alpha_j & \cos\theta_j \cos\alpha_j & -\sin\alpha_j & -\sin\alpha_j d_j \\ \sin\theta_j \sin\alpha_j & \cos\theta_j \sin\alpha_j & \cos\alpha_j & \cos\alpha_j d_j \\ 0 & 0 & 0 & 1 \end{bmatrix}. \tag{3.6} $$

The DH reference system is applied to the WG, where each degree of freedom is represented as a link in the system. The 2D WG model results in a six link robot. Table 3.2 represents all the reference frames (and hence links) considered to construct the dynamic model of the WG, with respect to the NED frame, using successive intermediary frames [40]. The forward (surge) motion of the WG float is represented by x_f, while the vertical (heave) motion is represented by z_f. The pitch of the WG float, tether, and glider, are represented by θ_f, θ_t, and θ_g, respectively. Fig. 3.3 shows the WG model with superimposed DH frames.

3.1.3 Wave Glider Parameters

The specifications for the WG platform required for populating the DH parameters are summarised in Table 3.3. As the tether is assumed to be light and rigid, it is assigned to be a zero mass. The length a_1 is the distance between the float's centre of gravity and attachment point of the tether. Similarly, a_3 is the distance between the glider's centre of gravity and attachment point of the tether. For the WG platform, both these values are zero, which simplifies the DH parametrisation. The length a_2 is the tether length, which is variable between 4 m to 20 m.

3.2 Wave Glider Dynamics

Once the kinematic equations of motion have been developed, they can be used in dynamic modelling [21]. Two possible modelling approaches for the the WG are Newton-Euler and Lagrange dynamic modelling. The Newton-Euler method models the forces exerted in the system on a component basis, while the Lagrange approach considers the total kinetic and potential energy of the system with generalised coordinates [40].

Table 3.2: Denavit-Hartenberg parameters for the Wave Glider platform.

Joint	Frames	d	θ	a	α
0	NED	0	$\frac{\pi}{2}$	0	$\frac{\pi}{2}$
1	Surge Motion	x_f	0	0	$-\frac{\pi}{2}$
2	Vertical Motion	z_f	$-\frac{\pi}{2}$	0	$-\frac{\pi}{2}$
3	Float Pitch	0	θ_f	a_f	0
4	Tether Pitch	0	$\theta_t - \theta_f$	a_t	0
5	Glider Pitch	0	$\theta_g - \theta_t$	$-a_g$	0

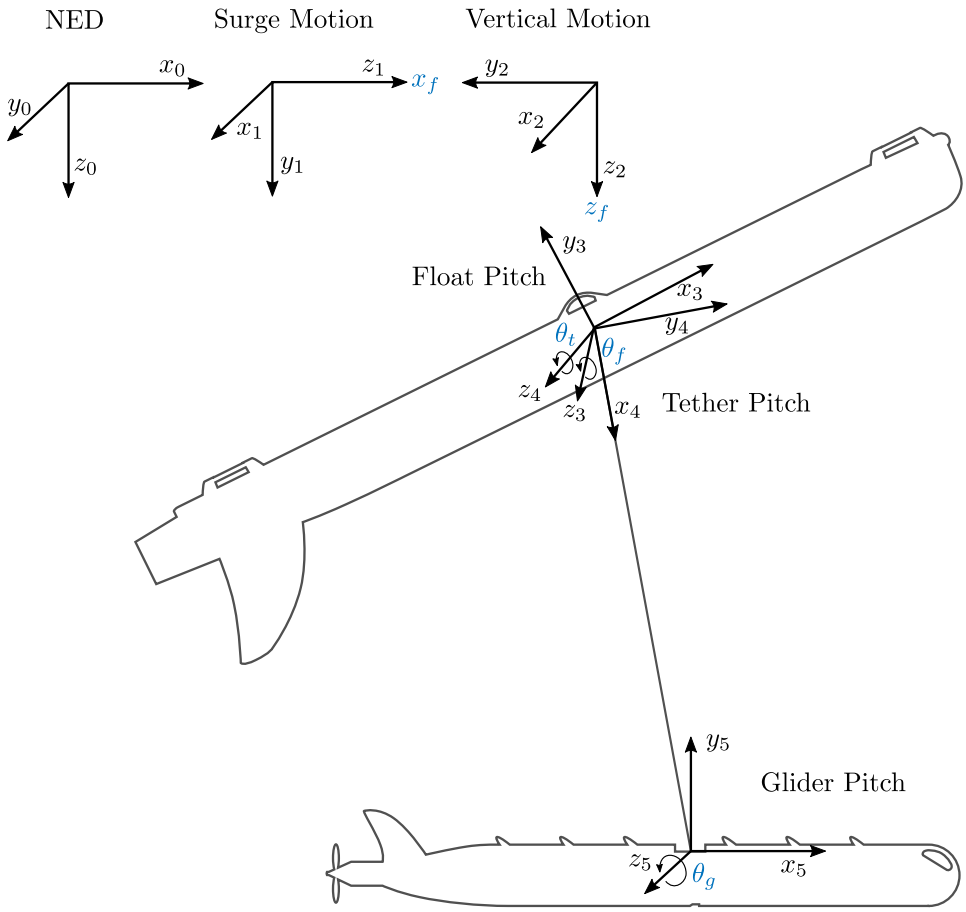

Figure 3.3: Wave Glider with Denavit-Hartenberg reference frames superimposed. The NED, surge motion, and vertical motion frames are translational, while the float, tether, and glider pitch frames are rotational. For each reference frame, actuation is either along or about the z_i axis (modified from [8]).

Table 3.3: Specifications for the Wave Glider platform (taken from [8]).

Specification	Float	Tether	Glider	Units
Mass	50	0	100	kg
Length	3.05	$4 - 20$	2.13	m
Width	0.81	0.10	1.42	m
Height	0.23	0.01	0.21	m

In addition, with Newton-Euler, handling of constraints such as conservative forces must be done explicitly, while Lagrange can handle these in a simpler way [42]. Furthermore, the Lagrangian method takes advantage of symmetry to produce less complex equations that are easier to understand. For these reasons, the Lagrangian method is preferred.

3.2.1 Lagrangian Energy Balance Equation

The dynamic model of the WG is described by the Lagrange equation as

$$M(\ddot{\vec{q}}) + C(\dot{\vec{q}})\dot{\vec{q}} + D(\dot{\vec{q}})\dot{\vec{q}} + \vec{g}(\vec{q}) = Q, \tag{3.7}$$

where M is the 5×5 inertia matrix, C is the 5×5 Coriolis and centripetal forces matrix, and D is the 5×5 damping matrix. The restorative gravitational and buoyancy forces vector is $\vec{g}$, while Q is a control vector that includes wind and wave forces, and all other external forces and friction imposed on the platform [21].

Populating the M, C, D and g matrices requires the Lagrangian, $\mathcal{L}$, which is formulated as the difference between kinetic and potential energy,

$$\mathcal{L} = \mathcal{K} - \mathcal{V}. \tag{3.8}$$

Eq. 3.8 encompasses the total energy in the system including all three rigid bodies. The kinetic energy, $\mathcal{K}$, is the sum of linear and rotational energies,

$$\mathcal{K} = \sum \left(\frac{1}{2} \dot{\vec{q}_l}^{\,T} M_l \dot{\vec{q}_l} + \frac{1}{2} \dot{\vec{q}_r}^{\,T} J_r \dot{\vec{q}_r} \right), \tag{3.9}$$

where M_l is the mass matrix, and J_r is the rotational inertia matrix. The generalised linear velocities are represented by $\dot{\vec{q}_l}$, while the generalised angular velocities are represented by $\dot{\vec{q}_r}$. The potential energy, $\mathcal{V}$, is the difference between the gravitational and buoyancy energies,

$$\mathcal{V} = \sum (M_l \vec{g} \vec{p} - \rho a \vec{g} \vec{p}), \tag{3.10}$$

where ρ is the density of water. The submerged depth of the float is represented by h in $\vec{p}$, which is multiplied by the wetted cross-section of the float, a, to give the submerged volume of the float responsible for generating the buoyancy force. The dynamic equations of motion are then represented by the Lagrange equation for each generalised coordinate [21],

$$\frac{\mathrm{d}}{\mathrm{d}t} \frac{\partial \mathcal{L}}{\partial \dot{\vec{q}}} - \frac{\partial \mathcal{L}}{\partial \vec{q}} = Q. \tag{3.11}$$

The matrices M, C, and $\vec{g}$, with $a_1 = a_3 = 0$, are defined as

$$M = \begin{bmatrix} m_0 + m_1 & 0 & 0 & -a_2 m_1 \sin(\theta_2) & 0 \\ 0 & m_0 + m_1 & 0 & -a_2 m_1 \cos(\theta_2) & 0 \\ 0 & & J_0 & 0 & 0 \\ -a_2 m_1 \sin(\theta_2) & -a_2 m_1 \cos(\theta_2) & 0 & J_1 + a_2^2 m_1 & 0 \\ 0 & 0 & 0 & 0 & J_2 \end{bmatrix}, \tag{3.12}$$

$$C = \begin{bmatrix} 0 & 0 & 0 & -a_2 m_1 \dot{\theta}_2 \cos(\theta_2) & 0 \\ 0 & 0 & 0 & a_2 m_1 \dot{\theta}_2 \sin(\theta_2) & 0 \\ 0 & 0 & 0 & 0 & 0 \\ 0 & 0 & 0 & 0 & 0 \\ 0 & 0 & 0 & 0 & 0 \end{bmatrix}, \tag{3.13}$$

$$\vec{g} = \frac{1}{100} \begin{bmatrix} 0 \\ -g(100m_0 + 100m_1 - \rho a h) \\ 0 \\ a_2 g \cos(\theta_2)(100m_1 - \rho a h) \\ 0 \end{bmatrix}, \tag{3.14}$$

where m_0 and m_1 are the float and glider masses respectively, and a_2 is the tether length. J_0, J_1, and J_2, are the rotational inertias of the float, tether, and glider respectively.

3.3 Wave Glider Modelling Summary

The five DOF model formulated in this chapter can be used for developing the sea state estimator. The model developed in this chapter is simulated with real values. The simulation results of the model under different conditions are presented in Chapter 8.

As the focus of this project is not wave glider modelling, added mass effects and further dynamic modelling of the WG are not presented. Modelling the effects of added mass are required for accurate representation of the WG dynamics. Presently, the WG is modelled as a massless cork floating on the air-sea boundary, which is sufficient for a preliminary study into the sea state estimation. An alternative higher DOF model of the WG has been developed independently to this study, that explores added mass effects, extending the dynamic modelling work covered in this text [43]. For the final path planning system, a model such as this should be combined with the state estimation to account for the glider responses to the sea.

Chapter 4

Ocean Dynamics

Rather than describing a single observation of the sea surface, the wave spectrum is used to describe the sea surface as a stochastic process. The benefits of this are that all possible observations can be described in a single model. In this chapter, the wave spectrum representation is explored and used as the basis for developing an ocean wave simulator.

4.1 Describing Ocean Waves

For short time scales of 15 min to 30 min, the conditions of stationarity and homogeneity described in Chapter 2.2.2 hold true and the following analysis can be carried out. Consider the free surface elevation, $\bar{h}(\vec{x}, t)$, at a location, $\vec{x} = [x, y]$, as a function of time, shown in Eq. 4.1. This describes the surface elevation as a sum of multiple harmonic components at different frequencies, propagating from a mean propagation direction, θ_j, relative to $\vec{x}$ [26]. For each frequency, ω_i, the random phase is $\bar{\gamma}_{ij}$, while $\bar{a}(\omega_i, \theta_j)$ is the random amplitude, where the over-bar denotes that these are random variables. The model is aptly referred to as the random phase and amplitude model [24].

$$\bar{h}(\vec{x}, t) = \sum_{ij} \bar{a}(\omega_i, \theta_j) \sin(\omega_i t + \vec{k}_i \cdot \vec{x} + \bar{\gamma}_{ij}), \tag{4.1}$$

$$\vec{k}_i = \left[|\vec{k}_i| \sin(\theta_j),\ |\vec{k}_i| \cos(\theta_j) \right]^T, \tag{4.2}$$

where ω_i is the angular frequency, and $\vec{k}_i$ the wave number. In Eq. 4.2, $|\vec{k}_i| = 2\pi/\lambda_i$, where λ_i is the spatial wavelength. This model has a total of three dimensions; two spatial and one temporal. However, it can be represented using only two indices, i for summing over frequencies, and j over directions using the angle θ_j. Initially, a single common direction for all waves is used as a simplifying assumption while developing the wave generator and subsequent estimator, hence the subscript, j, for θ is dropped.

The link between ω_i and $|\vec{k}_i| = k_i$ is the dispersion relationship for surface gravity waves in Chapter 2.2.2, and is approximated as $\omega_i^2 \approx g k_i$ for deep water waves [24]. Linear wave theory binds the spatial behaviour of waves to the temporal behaviour at any point in the wave field, and is used extensively in this text to simplify Eq. 4.1 and other equations derived from it.

4.1.1 The Random Phase and Amplitude Model

For each ω_i in Eq. 4.1, when the deep water condition is true, $\bar{\gamma}_{ij}$ is a random variable with a uniform distribution, $\bar{\gamma}_{ij} \sim \mathcal{U}(0, 2\pi)$ [24]. Hence, the phase spectrum is governed by the probability density function

$$f_\gamma(\gamma_i) = \frac{1}{2\pi} \qquad \text{for} \quad 0 < \gamma_i \leq 2\pi. \tag{4.3}$$

Due to the narrow band nature of the wind wave spectrum under consideration, each random amplitude is treated as being independent and following a random walk process [44]. It is governed by a Rayleigh distribution with the probability density function

$$f_a(a_i) = \frac{\pi a_i}{2\mu_i^2} \exp\left(\frac{-\pi a_i^2}{4\mu_i^2}\right) \qquad \text{for} \quad a_i \geq 0, \tag{4.4}$$

where in the case of wind waves, the single parameter used to characterise the distribution is the expected value of the amplitude, $\mu_i = E\{\bar{a}(\omega_i, \theta_j)\}$, for each frequency. This concept is borrowed from Rayleigh's assessment of sound amplitudes derived from multiple independent sources, and applied to ocean wave theory by Longuet-Higgins [44].

For each frequency in the wave spectrum, the phase will be a random draw from Eq. 4.3 while the random amplitude is drawn from Eq. 4.4. This process for generating a surface elevation observation is illustrated in Fig. 4.1 for a few wave components.

4.2 Ocean Wave Spectral Models

The variance density spectrum, obtained by taking the expectation of the squared amplitude in Eq. 4.1, is particularly important as it describes the collection of frequencies and their magnitudes present in the wave field. Eq. 4.5 is the variance density spectrum, which is a preferred representation over the amplitude spectrum, as it has stronger ties to physical quantities of waves; that is, wave energy is proportional to the variance of surface elevation [24].

$$\sum_{i=1}^{N} E\left\{\frac{1}{2}\bar{a}^2(\omega_i, \theta)\right\} = S(\omega_i, \theta), \tag{4.5}$$

where $\frac{1}{2}a^2(\omega_i, \theta)$ is the variance of a harmonic wave component, $h(\vec{x}, t)$, with amplitude a [24]. In Eq. 4.5, the variance of the surface elevation is equal to the sum of the individual variances. In the case of uni-modal and uni-directional wave spectra caused by wind, Eq. 4.5 can be approximated by the general wave spectrum equation discussed in Chapter 2.2.2,

$$S(\omega_i) = \frac{A}{\omega_i^5} \exp\left(-\frac{B}{\omega_i^4}\right). \tag{4.6}$$

The Pierson-Moskowitz (PM) spectral model can be formed from Eq. 4.6 for fully developed seas, with $U_{19.5}$ as the single input parameter. A and B are calculated as shown in Eq. 4.7 with empirically derived, dimensionless constants, $\alpha = 8.1 \times 10^{-3}$, and $\beta = 7.4 \times 10^{-1}$ [29, 30].

$$A = \alpha g^2, \qquad B = \beta \omega_0^4, \qquad \omega_0 = g/U_{19.5}. \tag{4.7}$$

Finally, the PM spectrum is expressed as

$$S(\omega_i) = \frac{\alpha g^2}{\omega_i^5} \exp\left(\frac{-\beta \omega_0^4}{\omega_i^4}\right). \tag{4.8}$$

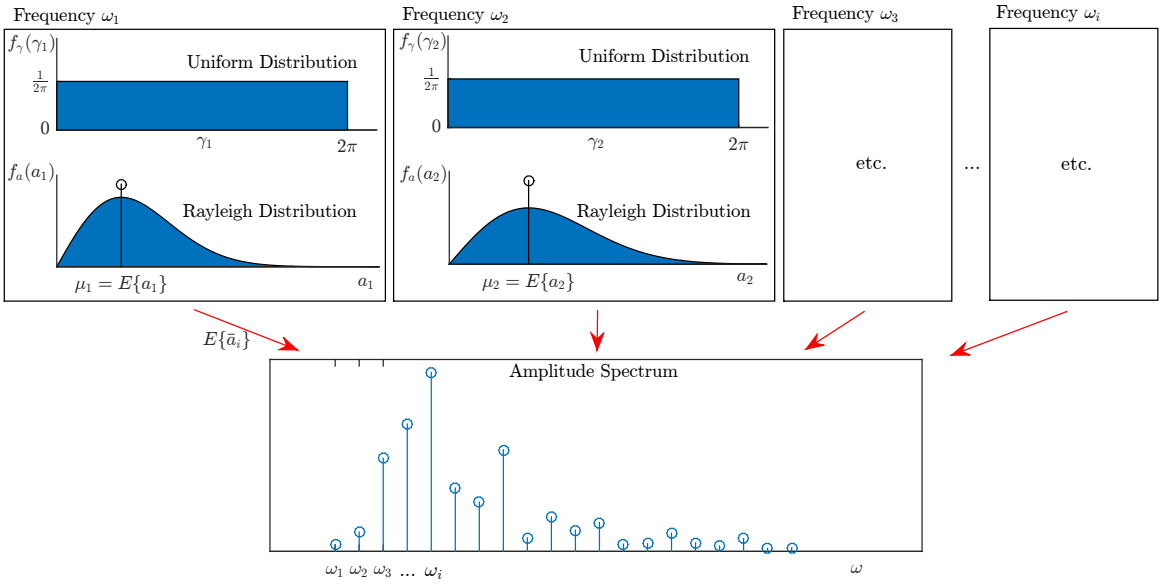

Figure 4.1: Realisation of the amplitude spectrum; for each frequency, phase is drawn from a random normal distribution, $\bar{\gamma}_{ij} \sim \mathcal{U}(0, 2\pi)$. Each random amplitude is drawn from a Rayleigh distribution with an expected value conforming to the spectral distribution used, such as the Pierson Moskowitz, JONSWAP e.t.c (adapted from [24]).

The peak of the spectrum is obtained by taking the derivative of Eq. 4.6, with respect to ω_i as

$$\frac{\mathrm{d}S(\omega_i)}{\mathrm{d}\omega_i} = \left(-5\frac{A}{\omega_i^6} + 4\frac{AB}{\omega_i^{10}} \right) \exp\left(\frac{-\beta\omega_0^4}{\omega_i^4} \right). \tag{4.9}$$

The turning point is found when $\frac{\mathrm{d}S(\omega_i)}{\mathrm{d}\omega_i} = 0$, which results in a peak frequency of

$$\omega_p = \sqrt[4]{\frac{4}{5}B}. \tag{4.10}$$

Eq. 4.6 represents the one dimensional variance density spectrum. That is, the energy at different frequencies along one spatial direction. Introducing more directions to the spectrum is done so with a spreading function. This is done by considering Eq. 4.8 as the spectrum in the direction of the wind, and assuming some spreading function, $D(\theta)$, that modifies the spectrum when moving away from the principal wind direction, as shown in Fig. 4.2.

The spreading function is dimensionless, and is unity when summed up along all directions from 0 rad to 2π rad, as $\int_0^{2\pi} D(\theta)\mathrm{d}\theta = 1$ [24]. An example of a spreading function used is shown in Eq. 4.11, as

$$D(\theta) = \begin{cases} \frac{2}{\pi}\cos^2(\theta) & \text{for } |\theta| \leq 90°, \\ 0 & \text{for } |\theta| > 90°, \end{cases} \tag{4.11}$$

where θ is the wave direction. This approximation indicates that the spreading gives a maximum amplitude in the wind direction, falling off gradually as the direction moves away from that point [45]. Inclusion of the spreading function gives the resulting two dimensional frequency-direction spectrum

$$S(\omega_i, \theta) = S(\omega_i)D(\theta). \tag{4.12}$$

Since a single common direction θ has been assumed in this dissertation, the spreading function is unity for all frequencies. In addition, only the uni-modal wave spectra is considered in this

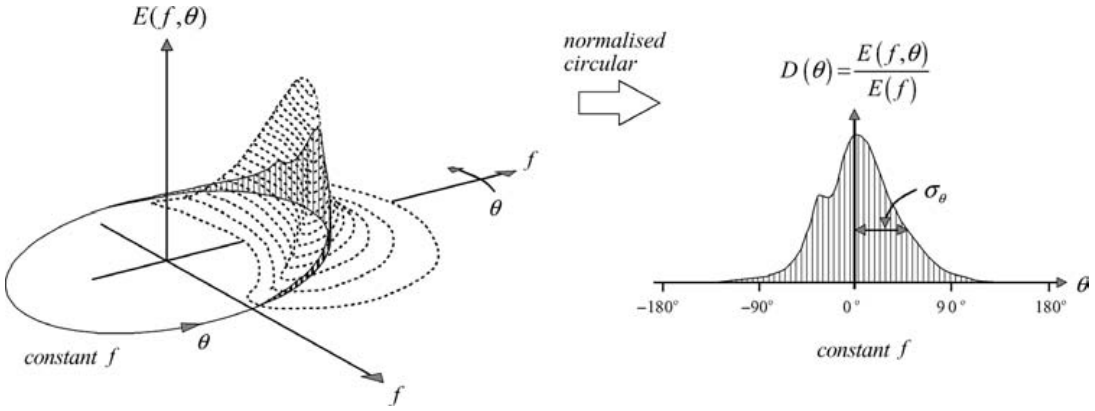

Figure 4.2: Directional energy distribution for a selected frequency component (taken from [24]).

dissertation. A bi-modal spectrum is one that has two modes, one from wind seas and the other from swell effects. The bi-modal case is not considered because swell waves are at lower frequencies and do not fall in the region of interest for short term navigation.

Fig. 2.3 shows the overlap of swell waves and wind seas. It is possible to partition the spectrum into a swell section (from $0.13\,\mathrm{rad}\cdot\mathrm{s}^{-1}$ to $1.26\,\mathrm{rad}\cdot\mathrm{s}^{-1}$) and wind wave section (from $0.63\,\mathrm{rad}\cdot\mathrm{s}^{-1}$ to $6.28\,\mathrm{rad}\cdot\mathrm{s}^{-1}$). In estimating parameters such as significant wave height that rely on obtaining normalised spectral shapes (JONSWAP, PM etc.), spectral partitioning helps separate out the contribution of swell, especially in the overlapping part of the spectrum [46]. For the estimation strategy presented in this work, spectral partitioning is not required as the estimation strategy does not attempt to fit a known spectral model onto the waves, but estimates the spectrum directly.

4.3 Ocean Wave Generator Development

Using the definition of a wave field in Eq. 4.1, it is now possible to design a wave generator that simulates ocean surface behaviour with statistical properties conforming to Eq. 2.3. Oscillators with discrete frequency components are initiated using initial conditions that conform to the desired wave spectrum. As the simulation runs, the wave spectrum can be altered by varying the wind speed, which subsequently changes the amplitudes and frequencies present. The final output of this generator is the sum of the wave height components, $h_i(t)$, taken at each time step to give the wave height at that point,

$$h(t) = \sum_i h_i(t). \tag{4.13}$$

4.3.1 Initial Conditions for the Generator

To select an observation from the modelled process, initial conditions for the wave generator, $h_i(0)$ and $\dot{h}_i(0)$, are calculated using Eq. 4.14 and 4.15. For each ω_i, a random phase, $\bar{\gamma}_i$, is chosen from a uniform distribution, $\mathcal{U}(0, 2\pi)$. Likewise, a random amplitude, $S_r(\omega_i, \theta)$, is chosen

from a Rayleigh distribution with an expected value $\mu_i = \sqrt{S_0(\omega_i, \theta)}$ [24].

$$h_i(0) = \sqrt{2\Delta\omega_i S_r(\omega_i, \theta)}\sin(\bar{\gamma}_i) \tag{4.14}$$

$$\dot{h}_i(0) = \sqrt{2\Delta\omega_i S_r(\omega_i, \theta)}\omega_i \cos(\bar{\gamma}_i) \tag{4.15}$$

In reality, the ocean wave spectrum contains all frequencies, rather than discrete points. Hence $\Delta\omega_i$ is the width of each frequency component required to make the simulated wave spectrum a variance density spectrum, which is a better representation of the true wave density spectrum [24]. Eq. 4.16 shows how a Rayleigh distributed variate, X, can be obtained from a uniform distribution, $\mathcal{U}(0,1)$. $S_r(\omega_i, \theta)$ is calculated in this way using the initial wave spectrum $S_0(\omega_i, \theta) = \mu_i^2$, as shown in Eq. 4.17. An example of a calculated realisation of $S_r(\omega_i, \theta)$ used in simulation is shown in Fig. 4.3.

$$X = \mu_i\sqrt{-2\log\left(\mathcal{U}(0,1)\right)} \tag{4.16}$$

$$S_r(\omega_i, \theta) = 2S_0(\omega_i, \theta)\log\left(2 - \mathcal{U}(0,1)\right) \tag{4.17}$$

The peak frequency and magnitude, ω_p and S_{ω_p}, are calculated online for a given wind speed $U_{19.5}$, which ranges from $1\,\mathrm{m}\cdot\mathrm{s}^{-1}$ to $20\,\mathrm{m}\cdot\mathrm{s}^{-1}$, corresponding to an ω_p ranging from $8.6\,\mathrm{rad}\cdot\mathrm{s}^{-1}$ to $0.4\,\mathrm{rad}\cdot\mathrm{s}^{-1}$ respectively. This range is found by using the peak frequency calculated in Eq. 4.10 with PM parameters, as

$$\omega_p = \frac{g}{U_{19.5}}\left(\frac{4}{5}\beta\right)^{1/4}, \tag{4.18}$$

$$S_{\omega_p} = S(\omega_p, \theta). \tag{4.19}$$

The normalised spectrum in Fig. 4.3 is scaled in frequency by ω_p, and correspondingly in magnitude by S_{ω_p} to give the desired variance density spectrum at any wind speed, Eq. 4.20. In this way, $U_{19.5}$ can be varied continuously while maintaining the initial conditions stated in Eq. 4.14 and 4.15.

$$\omega_i = \omega_p \cdot \boldsymbol{\omega}_0, \tag{4.20}$$

$$S_d(\omega, \theta) = S_r(\omega, \theta) \cdot S_{\omega_p}, \tag{4.21}$$

where $\boldsymbol{\omega}_0$ is an initial normalised vector of the frequency components used in the generator. The transient mechanism as sea state develops is not examined. Rather, $U_{19.5}$ is assumed to change slowly, and sea state changes in quasi steady-state.

4.3.2 Oscillators for Wave Generation

A standard implementation of an oscillator commonly found in electronic circuit designs is used to compose the wave height components. Once initiated, this oscillating system will continue to oscillate at set amplitudes and frequencies indefinitely, as

$$\ddot{h}_{\omega_i}(t) = -\omega_i^2(t)h_i(t), \tag{4.22}$$

where $\omega_i(t)$ is the frequency, $\ddot{h}_{\omega_i}(t)$ is the vertical acceleration, and $h_i(t)$ the instantaneous height component. However, an important feature for this generator to have is the ability to change as the wind speed input varies; that is, to adjust the wind speed continuously without restarting the generator with new initial conditions. This added functionality allows for validation of the peak frequency tracker discussed in Chapter 6.

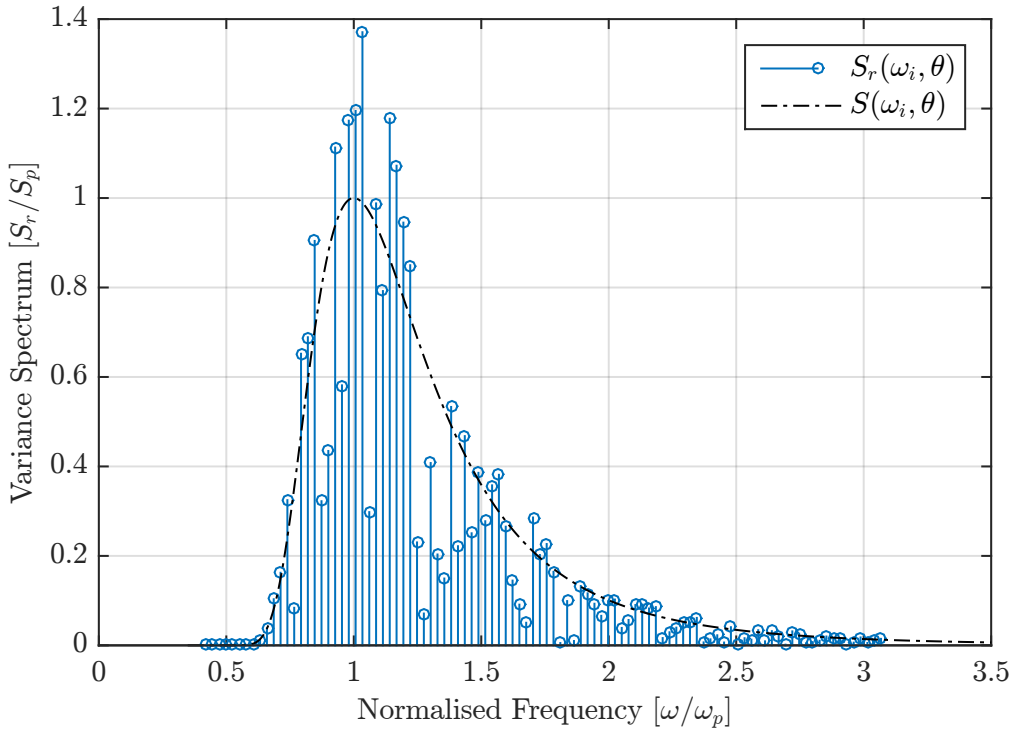

Figure 4.3: Realisation of a normalised variance spectrum with Rayleigh distributed magnitudes, $S_r(\omega_i, \theta)$. Multiplying each component with the width between successive components gives the variance density spectrum.

Adjusting the Wind Speed

Continuous adjustment of the wind speed is achieved by adding a damping term for each discrete frequency component, $\zeta_i(t)$, to the standard oscillator in Eq. 4.22, resulting in the second order damped oscillator in Eq. 4.23. Both $\zeta_i(t)$ and $\omega_i(t)$ are slow varying quantities. From this point on, they are referred to without the argument as ζ_i and ω_i. When ζ_i is (slightly) positive or negative, the amplitude of the oscillations will grow or diminish respectively, as shown in Fig. 4.4 where the growth of the envelope is $\exp(-2\zeta_i\omega_i t)$ [47].

$$\ddot{h}_{\omega_i}(t) = -2\zeta_i\omega_i\dot{h}_i(t) - \omega_i^2 h_i(t), \tag{4.23}$$

$$d = 2\zeta_i\omega_i, \tag{4.24}$$

where d is the term fed back in Fig. 4.5, with a scaling by $2\omega_i$ which makes the components adjust their amplitudes at a rate proportional to their frequencies.

Fig. 4.5 illustrates how the ζ_i values are calculated and used to change the amplitudes. The Fourier components of the current spectrum power are extracted using Eq. 4.25, then compared to the desired spectrum power in Eq. 4.19. The feedback network represented with dashed lines in Fig. 4.5 will produce the positive and negative damping terms for each component, ζ_i, that will drive the current spectrum power, $H_i(\omega, \theta)$, towards the desired set-point, $S_d(\omega, \theta)$. When $H_i(\omega, \theta)$ is equal to $S_d(\omega, \theta)$, ζ_i is driven to zero and the system is in steady-state. Fig. 4.5 shows that changes in wave height will always be smooth and continuous, since both ζ_i and ω_i affect $h_i(t)$ indirectly through two integrators, which introduces a low-pass effect.

$$H_i(\omega_i, \theta) = \frac{1}{2\Delta\omega_i}\left(\frac{1}{\omega_i^2}\dot{h}_i^2(t) + h_i^2(t)\right), \tag{4.25}$$

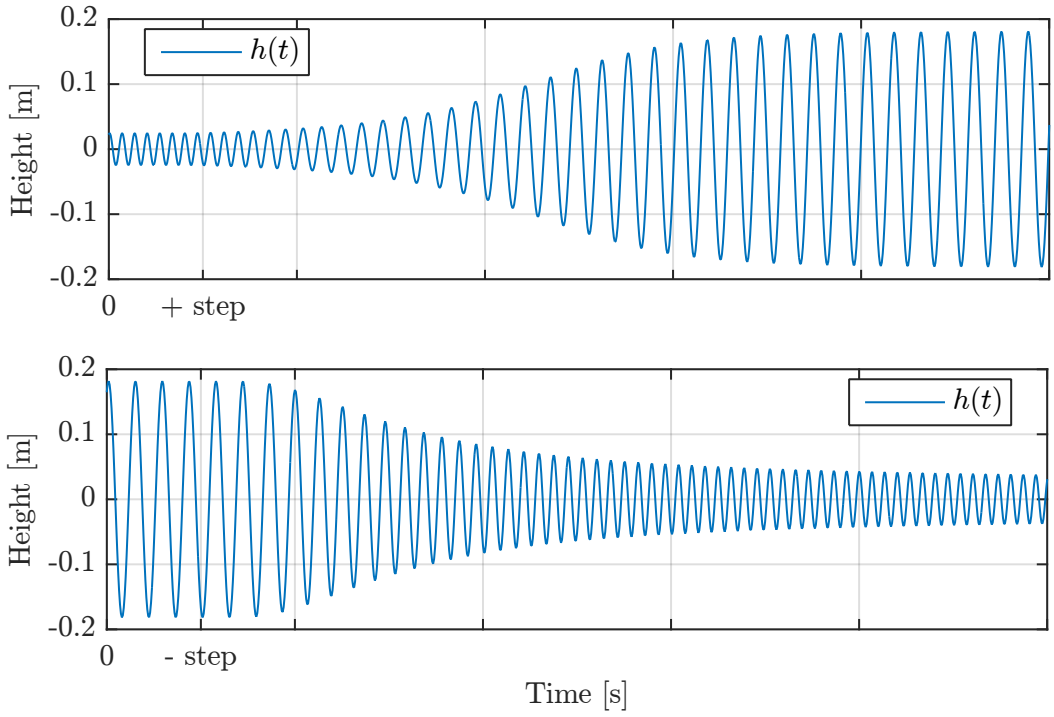

Figure 4.4: (Top) The amplitude of a single wave component increases while its frequency decreases, due to an instantaneous step change in wind speed from $7\,\mathrm{m}\cdot\mathrm{s}^{-1}$ to $15\,\mathrm{m}\cdot\mathrm{s}^{-1}$. (Bottom) When the step change is inverted, the amplitude decreases and the frequency increases. The rate of change for both situations is characterised by an exponential envelope, $\exp(-2\zeta_i\omega_i t)$, with a time constant of multiple hours.

where $\dot{h}_i(t)$ is the time derivative of $h_i(t)$, and $\Delta\omega_i$ the spacing between frequencies. This scaling factor is present to account for the discrete nature of the representation, whereas in reality all frequencies may be present in sea spectra.

Dynamics of the Damping Term

The dynamics of ζ_i set by the controller, $F(s)$, in Fig. 4.5, must be designed in such a way that waves grow or diminish at a rate representative of real ocean wave behaviour. The transfer function of the damping system takes incremental changes, $\Delta\zeta_i$, and translates them to wave height changes. Three conditions exist for ζ_i:

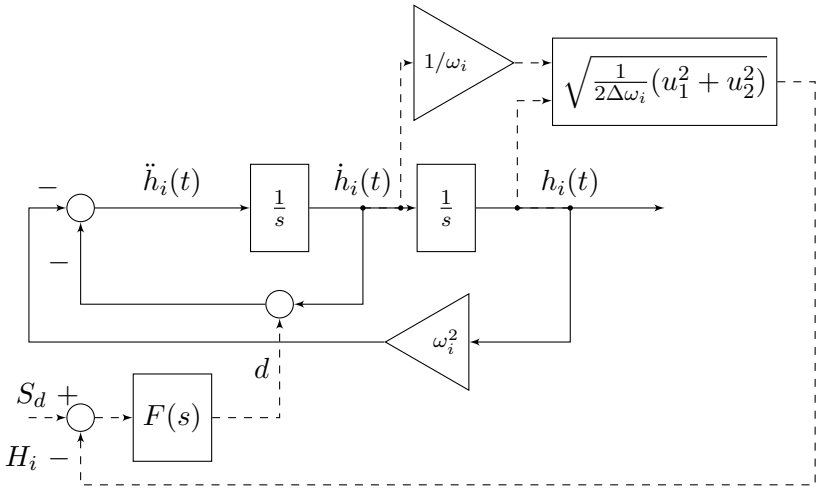

Figure 4.5: Composition of sea waves using damped sinusoidal components; two integrators in feedback produce oscillations at selected frequencies, ω_i, while the feedback term, $d = 2\zeta_i\omega_i$, is adjusted using a PI controller to track a desired set-point.

- $\zeta_i > 0$: amplitude of wave component increases while frequency decreases.
- $\zeta_i = 0$: amplitude of wave component remains the same (default value).
- $\zeta_i < 0$: amplitude of wave component decreases while frequency increases.

Following the PM spectral model, constant winds blow for prolonged periods of time and change gradually to produce the waves simulated in this study [29]. ζ_i is bounded to avoid an excessively large damping factor causing issues with the transitions. Eq. 4.26 is the plant model for the wave adjustment mechanism. It represents the transfer function from the Fourier component calculation, $H_i(\omega, \theta)$, to the damping term, ζ_i.

$$P(s) = -\frac{2\omega_i}{s} \tag{4.26}$$

A controller for the damping term is designed with the general form shown in Eq. 4.27. It is designed to have a slow reset time, as well as a low cross-over frequency of $0.03\,\mathrm{rad}\cdot\mathrm{s}^{-1}$, as shown in the inverse Nichols plot in Fig. 4.7. The phase margin at the cross-over frequency is 44°. Noise is present at frequencies above the region of interest. To attenuate this high frequency noise, a lag term with a cut off frequency of $0.12\,\mathrm{rad}\cdot\mathrm{s}^{-1}$ is used. It acts as a low pass filter and reduces the gain at high frequencies, resulting in the final form shown in Eq. 4.28

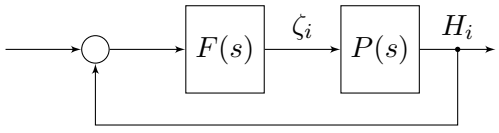

Figure 4.6: Control loop showing the transfer function, $P(S)$, between the damping term, ζ_i, and the Fourier components for each harmonic, H_i, with a controller, $F(s)$.

with the desired response speed.

$$F(s) = \frac{k}{s}\frac{(s+\frac{1}{\alpha T})}{(s+\frac{1}{T})} \tag{4.27}$$

$$F(s) = \frac{4.9\times10^{-5}}{s}\frac{(53.4s+1)}{(8.4s+1)} \tag{4.28}$$

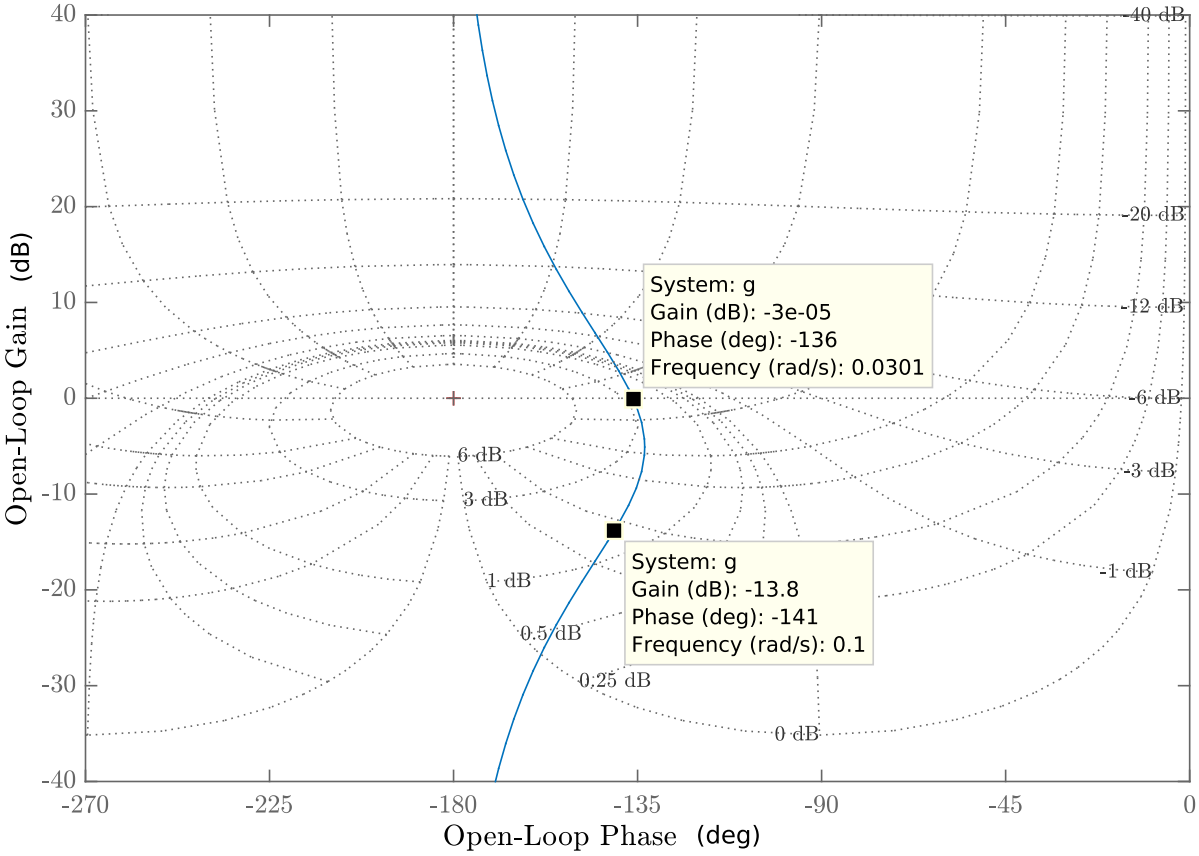

Figure 4.7: Inverse Nichols plot for wave generator filter, showing a gain cross-over frequency of $0.03\,\mathrm{rad}\cdot\mathrm{s}^{-1}$. To attenuate higher frequencies, a low pass filter is used with a cut-off frequency at $0.1\,\mathrm{rad}\cdot\mathrm{s}^{-1}$.

4.3.3 Wave Generator Output

A realisation of the wave height is shown in Fig. 4.8, with a step in the wind speed from $12\,\mathrm{m}\cdot\mathrm{s}^{-1}$ to $7\,\mathrm{m}\cdot\mathrm{s}^{-1}$. The transition is smooth, takes place over multiple wave lengths, but is faster than the typical changes experienced in reality. The figure also shows a 100 s sample of the longer waveform in detail.

This chapter set out to describe deep ocean waves and provide a method of simulating waves that are used for validation in the following chapters.

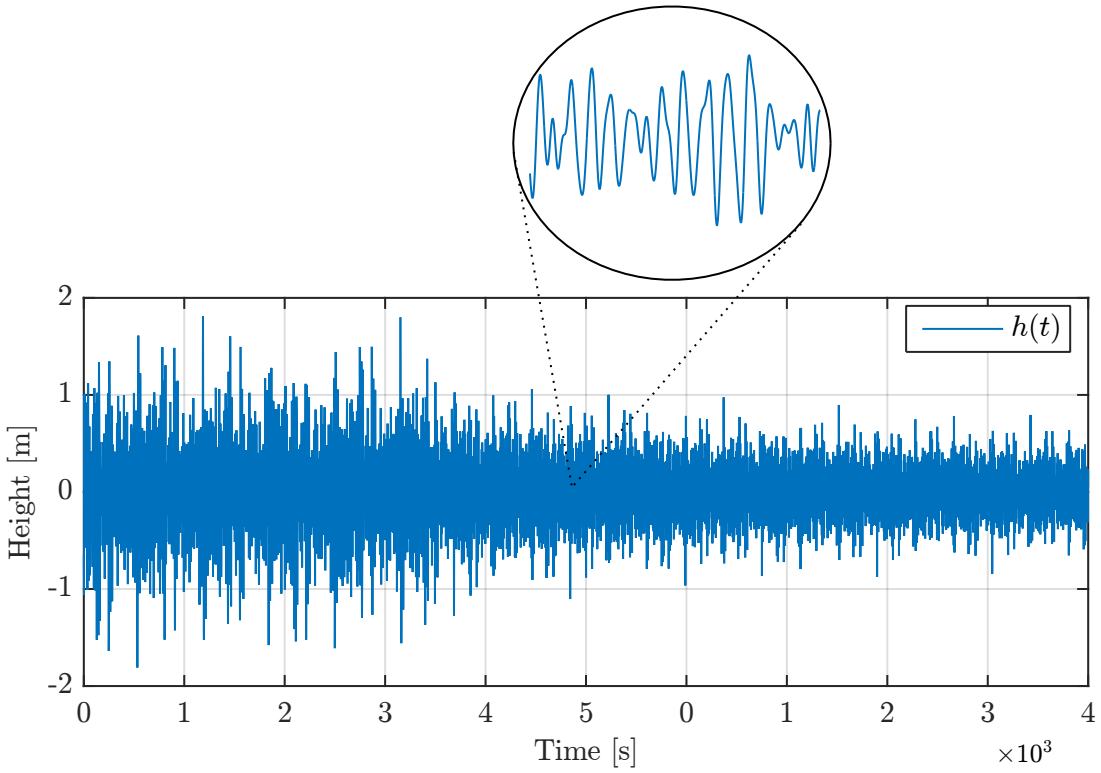

Figure 4.8: Wave generator output with a step change in wind speed from $12\,\mathrm{m}\cdot\mathrm{s}^{-1}$ to $7\,\mathrm{m}\cdot\mathrm{s}^{-1}$ at $t = 1.5\times10^{3}\,\mathrm{s}$. A 100 s section is zoomed in to show the wave elevation in detail.

Chapter 5

Spectral Estimation

This chapter describes in detail the filtering strategy developed for wave prediction. Firstly, an overview of the estimation strategy is presented. Following this, simplifying assumptions necessary for the filter to be set up are laid out, before discussing the final estimation strategy chosen for the system. Of particular importance in this chapter is the process and measurement noise analysis presented at the end.

5.1 Estimation Strategy Overview

The most common method of sea state spectrum estimation involves using the Fast Fourier transform (FFT). A benefit of using FFTs is the broad band of frequencies it can analyse. However, FFTs require long data records for smoothing. Hence, FFT results do not allow for on-line wave height estimation. The benefits provided in resolution and low noise come at the cost of time and the number of samples required to obtain each set of results [37]. Therefore the trade-off for the sea state estimation is between noise, fidelity, and speed of computation, where the FFT method prioritises low noise and high fidelity, for the sake of speed of calculation.

An alternative strategy makes use of an Extended Kalman filter (EKF) to estimate a few discrete parameters of the wave spectrum [15]. With less information to estimate, the online tracking task is made tractable, allowing for prediction capabilities. The idea behind this method is that the entire wind wave spectrum need not be estimated to provide a useable result. Hence this method prioritises speed of calculation over noise and resolution. Fidelity is moderately compromised, but can be kept to a level that is acceptable to allow for the ocean surface to be mapped adequately.

Fig. 5.1 shows an overview of the estimator interacting with the real world. From inertial strap-down measurements obtained on the mobile platform, a peak frequency estimator is used to extract the peak. It is fed into the EKF along with the inertial measurements to produce wave height estimates. The real world section shows the sea state and platform dynamics, both of which have been detailed in preceding chapters.

5.1.1 Motivation for Estimating the Peak Frequency

Uni-modal wind wave spectra generally consist of a single high energy peak. The three unknowns in estimating a sinusoid are magnitude, frequency and phase. It is possible to have a fixed

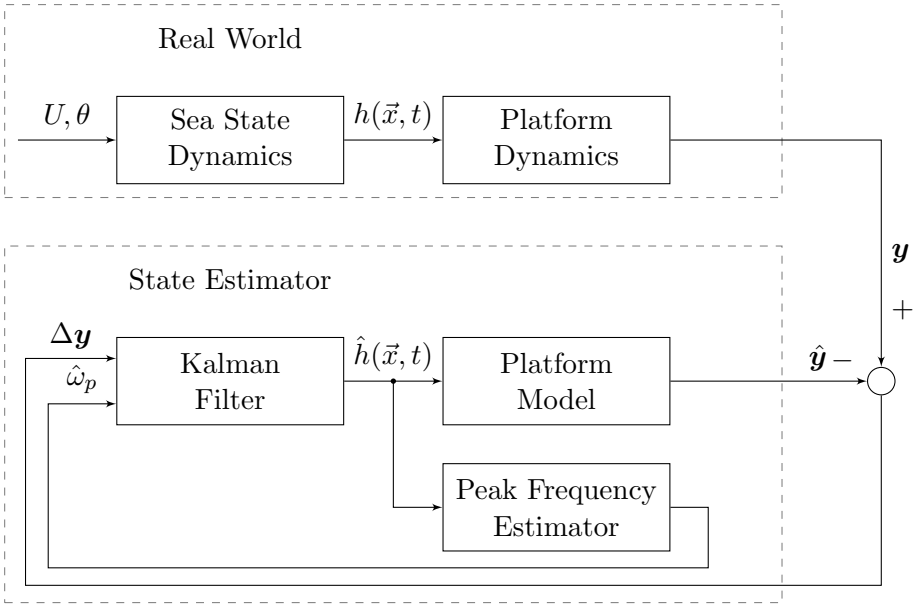

Figure 5.1: Complete overview of the estimation strategy, including the wave simulation section: (Wave Dynamics) simulated wave generator and platform dynamics produce measurements, $\boldsymbol{y}$; (State Estimator) measurements are compared to an estimate obtained using a platform model, Kalman filter, and peak frequency estimator. The peak frequency, ω_p is estimated from the Kalman filter output, which is used to capture energy for remaining frequencies surrounding the peak.

magnitude or frequency so that only two unknowns need to be estimated. With the fixed magnitude method, a spectral shape is calculated using a known spectral model such as PM or JONSWAP and used as an input. This is a parametric approach, which forces the estimator to fit the shape of a known spectral model [46].

If the spectral model used is a good representation of the ocean waves, then the error between the estimate and the sea wave spectrum will eventually be minimised and tracking achieved. The estimated quantities are the frequencies present in the spectrum and their respective phases. A problem with this method is that it attempts to fit the data onto a spectral model that is the expected variance, and not the actual value of the ocean wave spectrum. Due to this, the estimation strategy's performance is subject to the quality of the wave model used and will only approximate the true spectrum. In addition, multiple oscillators can end up tracking the same frequency component, resulting in unobservable states in the filter.

There is also the possibility of using a rational approximation of the spectrum, scaled by ω_p (through its relation with the wind speed, $U_{19.5}$). This is a noise whitening approach that seeks to answer the question: what filter is required such that a white noise input produces the desired wind wave spectrum? However, this could suffer from the same issues of incorrect fitting as using the PM or JONSWAP models. This method is not pursued in the present work. However an initial investigation into the noise whitening strategy is presented in Appendix A.

The alternative method of fixing the frequency points avoids this issue. The frequency components can be selected such that they never overlap, tracking the amount of energy contributed at those select frequencies to the overall ocean wave motion. This is a non-parametric approach that imposes fewer restrictions on the estimator. For this reason, the non-parametric approach is the preferred method, so that the estimator is not forced into a possibly incorrect spectral shape. Hence, using the general shape of the amplitude spectrum and its frequency range for varying wind speeds, the amplitude and phase of a few select frequencies in the range can be

estimated while using fixed frequency points [14, 16].

To ensure that the chosen frequency points will be in the correct range to capture most of the wave energy and hence give the estimator a starting point closer to the true spectrum, the peak frequency, ω_p, must be estimated [37]. Once obtained, the estimator's selected frequency components are centred around ω_p, where the bulk of the wave energy is located, and capture the remaining energy with lower error than if the peak frequency was unknown. In this chapter, it is assumed that the peak frequency estimate is available for use in the filter. A detailed procedure of obtaining the peak frequency is presented in Chapter 6.

5.1.2 Simplifying Assumptions for the Model

By considering only the vertical motion at a fixed point in space, it is possible to develop an estimator using the temporal behaviour. All rotations are restricted, as well as translation in heave and sway. The platform is treated as a cork floating on the ocean surface [13].

Adding rotations yields a model akin to a plank floating on the ocean surface, which has more spatial degrees of freedom. However, the platform is still considered to be stationary in the wave field, resulting in a platform model that can only translate vertically, roll, and pitch about its centre. The estimator developed is based on this 'plank' model, similar to the models used for 3D wave buoys that measure wave height and direction from heave, roll and pitch motions [48].

5.2 Developing State Equations

Following the standard development of an EKF outlined in Chapter 2.3.2, the state vector, once discretised and linearised, is shown in Eq. 5.1. F_k is the state transition matrix, while w_k is the associated zero mean, process noise vector, with variance Q_k.

$$\boldsymbol{z}_{k+1} = F_k \boldsymbol{z}_k + \mathrm{w}_k \tag{5.1}$$

5.2.1 Oscillator States

Provided that an estimate of the peak frequency is available, the amplitude, phase, and direction of wave components at frequencies surrounding the peak can be estimated to reconstruct the amplitude spectrum in Fig. 5.2. This is done using an EKF with a group of oscillators, $i = 1, 2, \ldots, n$, described by the second order differential Eq. 5.2 [36].

$$\ddot{h}_i(\vec{x}, t) = -\omega_i^2(t) h_i(\vec{x}, t) \tag{5.2}$$

Using two state variables at each frequency, $\omega_i(t)$, the phase and magnitude of each oscillator can be estimated. Hence wave height and its time rate of change, h_i and $\dot{h}_i$ respectively, are the state variables used for each frequency component,

$$\boldsymbol{z}(t) = \begin{bmatrix} h_1, & \dot{h}_1, & \cdots, & h_i, & \dot{h}_i, & \cdots, & h_n, & \dot{h}_n \end{bmatrix}^T. \tag{5.3}$$

The discrete time state transition model used for each frequency component oscillator, with T as the time step is represented in its exact form by

$$F_i = \exp\left(\begin{bmatrix} 0 & 1 \\ -\omega_i^2(t) & 0 \end{bmatrix} \cdot T \right). \tag{5.4}$$

The time varying squared term, $\omega_i^2(t)$, in the state differential equation results in a nonlinear state transition matrix shown in Eq. 5.4. For F_i to be considered linear, $\omega_i(t)$ must vary slowly. Chapter 6 details how the evolution of $\omega_i(t)$ is set such that a time-scale separation is achieved between $\omega_i(t)$ and the filter dynamics [49]. The time dependency of $\omega_i(t)$ is dropped from this point on, as it is considered constant with respect to the other dynamics of the filter. This means the linear representation in Eq. 5.1 can be used for the process equation.

5.2.2 Additional State Variables

Additional state variables required to complete the filter are the mean wave heading, θ, and accelerometer bias, b_a. Measurement biases of the three accelerometer axes are tracked and compensated by the 3×1 state variable, $\boldsymbol{b}_a$. Eq. 5.5 and 5.6 show the mean wave heading and bias state variables respectively, which are modelled as random walk processes. The resulting process model matrices for these state variables are shown in Eqs. 5.7 and 5.8. The associated process noise values for θ and $\boldsymbol{b}_a$, are w_θ and w_b respectively.

$$\theta_{k+1} = \theta_k + \mathrm{w}_\theta \tag{5.5}$$

$$\boldsymbol{b}_{a_{k+1}} = \boldsymbol{b}_{a_k} + \mathrm{w}_b \tag{5.6}$$

$$F_\theta = 1 \tag{5.7}$$

$$F_{b_a} = \begin{bmatrix} 1 & 0 & 0 \\ 0 & 1 & 0 \\ 0 & 0 & 1 \end{bmatrix} \tag{5.8}$$

They are appended to the oscillator state variables to give the total state vector

$$\boldsymbol{z}(t) = \begin{bmatrix} h_1, & \dot{h}_1, & \cdots, & h_i, & \dot{h}_i, & \cdots, & h_n, & \dot{h}_n, & \theta, & \boldsymbol{b}_a{}^T \end{bmatrix}^T, \quad i = 1, 2, \ldots, n. \tag{5.9}$$

Finally, F_i is repeated for n components and concatenated with $\mathrm{diag}(F_\theta,\ F_{b_a})$ to give the block diagonal matrix in Eq. 5.10, where n is the number of sinusoidal components used in the filter model. The size of F_k is dependent on how many frequency components are used in the estimator. For example, if three components are used, then $F_k \in \mathbb{R}^{10\times 10}$.

$$F_k = \mathrm{diag}(F_1, \cdots, F_i, \cdots, F_n, F_\theta, F_{b_a}), \quad F_k \in \mathbb{R}^{(2n+4)\times(2n+4)}. \tag{5.10}$$

5.2.3 Frequency Selection and Spacing

Only the peak frequency estimate is required in this estimation strategy. The remaining frequencies used in the filter are calculated using Eq. 5.11, a logarithmically distributed vector scaled by ω_p. Logarithmic spacing is used due to the concentration of wave spectrum energy at lower frequencies, shown in Fig. 5.2. Less energy is present at the higher frequencies than closer to the peak frequency, hence fewer components are used to capture this energy. The MATLAB log-space function from a frequency of 10^a to 10^b, with n points is used to obtain

$$\boldsymbol{\omega} = \omega_p \cdot \mathrm{logspace}(a, b, n). \tag{5.11}$$

Given several statistical models that fit a dataset, balance must be struck between goodness of fit and complexity for a given model to be an efficient representation. Increasing the number of frequency components in the estimator improves resolution and tracking accuracy. However, the complexity of the filter also increases as more components are added. In the context of

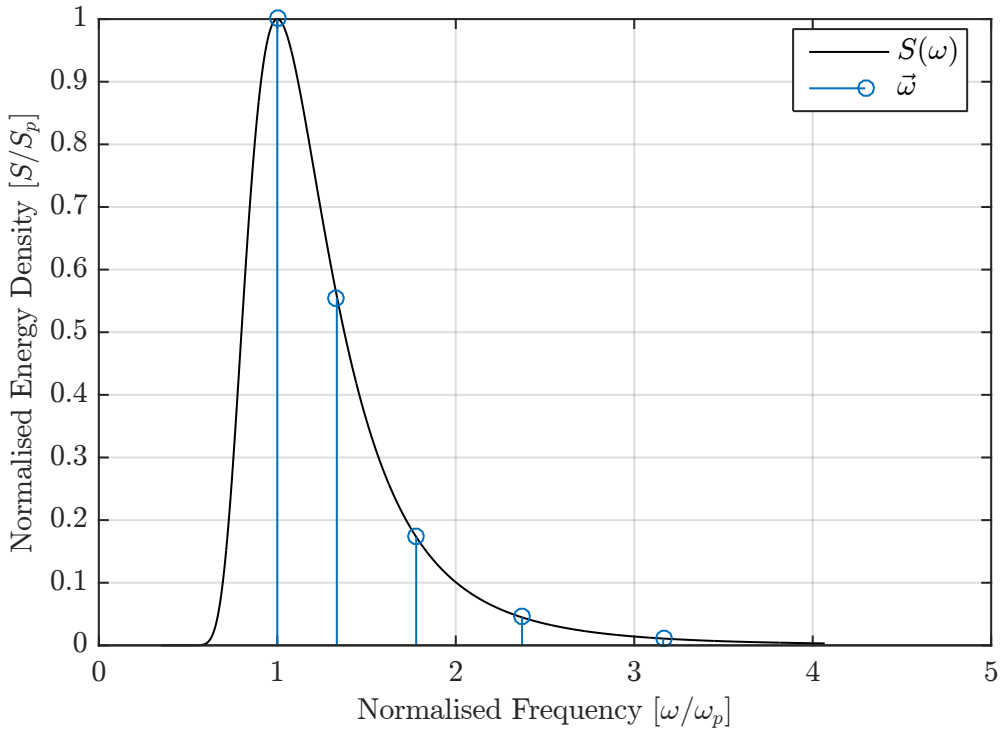

Figure 5.2: Normalised wave energy density spectrum, $S(\omega)$, shows the distribution of frequency points selected for the Kalman filter, shown by the stems. A logarithmic spacing emphasises the region where the majority of the energy is concentrated in the spectrum.

the estimator, increased complexity means a decrease in performance, such as the risk of losing observability of the system, an increase in tracking noise, as well as an increase in computational requirements.

Additionally, estimating at frequency points too close to one another leads to unobservable states, as the condition number of $\mathcal{O}$, which is its sensitivity of the estimator to inversion, gets worse. Hence it is necessary to carefully select the number of frequency components used in the filter. Further motivation for this is that when few measurements are available, a lower order Kalman filter will be faster at estimating the signal [36].

Using the Akaike Information Criterion (AIC) [50], an optimal number of components to use in the filter can be found. It will be optimal in that the best performance will be achieved with the least complexity possible. The AIC is used as a metric to compare models as it provides an estimate of relative information loss when a model is chosen to represent a dataset. With a penalty imposed on complexity of the model, the number of frequency components used in the filter is increased until the performance improvement is outweighed by increased complexity. The AIC is calculated as

$$\text{AIC} = 2n - 2l(Q), \tag{5.12}$$

where n is the number of parameters, in this case the number of frequency components used in the filter, and $l(Q)$ is the log-likelihood function in Eq. 5.13. Using this form, the AIC can be calculated directly from filter outputs, with wave height error covariance, P_{hh}, as the parameter

chosen for determining the index [51].

$$l(Q) = \frac{1}{2}\Big(- N \cdot \ln(\Gamma_{\Delta \underline{y}}) + \ln(P_{hh}) + N \Big), \tag{5.13}$$

$$\Gamma_{\Delta \underline{y}} = \frac{2\pi}{1+N} \sum_{i=0}^{N} (\underline{y} - \underline{\hat{y}})^2, \tag{5.14}$$

where N the number of samples taken, which is made as high as possible to avoid over-fitting the data. Truth and observed data in the residual sum of squares, $\Gamma_{\Delta \underline{y}}$, are $\underline{y}$ and $\underline{\hat{y}}$ respectively. Running sample data through the filter multiple times with increasing n parameter values yields the results in Fig. 5.3. The data used are wave realisations at a nominal wind speed of $10\,\mathrm{m} \cdot \mathrm{s}^{-1}$.

There is a downward trend in the index as the number of components is increased from an initial value of one. At six frequency components, the index reaches a minimum, after which the index begins to rise. This increase continues steadily as the number of components is increased, all the way up to a total of 18. At this point, the index begins to decrease once again. However, a deterioration in performance is already experienced at this stage, hence an increase of frequency components beyond 20 is not desirable and subsequently not chosen. Ultimately, the AIC dictates the optimal number of components to use in the estimator to be six, although there is a little play on either side of this number.

5.3 Developing Measurement Equations

Strap-down Micro Electro Mechanical Sensor (MEMS) measurements are available from a body-fixed IMU, which includes an accelerometer, gyroscope, and magnetometer. Information from these sensors can be related to the state variables being estimated by treating the measurement as the sum of sinusoids, where each individual contribution to the measurement is modelled by Eq. 5.2. In the discretised and linearised EKF model, measurements are described by

$$\boldsymbol{y}_k = H_k \boldsymbol{z}_k + \mathrm{v}_k, \tag{5.15}$$

where H_k is the measurement matrix, while v_k is the associated zero mean measurement noise vector with variance R_k.

5.3.1 Using the Acceleration Measurement

It is possible to measure height directly on the platform using a GPS or a barometer. Without these sensors, height must be estimated using indirect methods such as double integration of acceleration signals, which can provide relative height measurements. However, in high noise environments such as the ocean surface, small angle errors in IMUs can cause much larger errors in acceleration measurements. In addition, the relationship between the acceleration spectrum, $S_{aa}(\omega)$, and the height spectrum, $S_{hh}(\omega)$, are related by $G(s) = \frac{1}{s^2}$ [10], such that

$$S_{hh}(\omega) = |G(j\omega)|^2 S_{aa}(\omega), \tag{5.16}$$

$$S_{hh}(\omega) = \frac{1}{\omega^4} S_{aa}(\omega). \tag{5.17}$$

In this case, the plank position is obtained from double integration of the acceleration, where any small bias in the measurement will lead to large deviations over time, caused by integrator

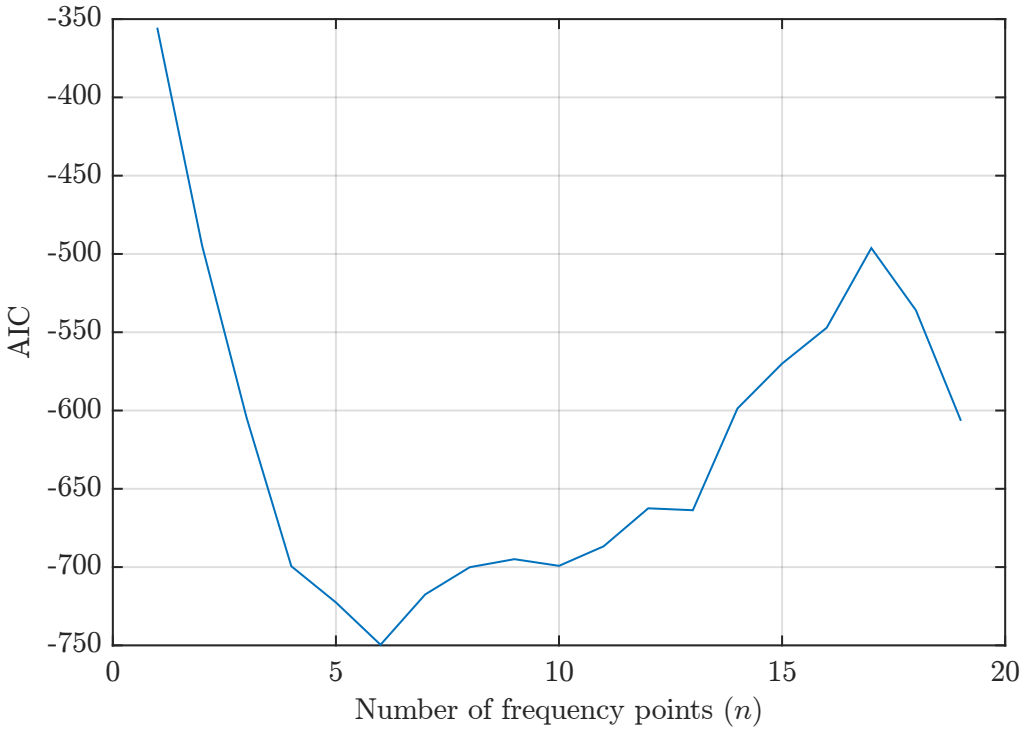

Figure 5.3: The number of frequency components used in the filter versus their AIC value. Having 6 frequency components in the filter gives the lowest AIC number. Although there is a dip in AIC above $n = 15$, there are observability issues experienced at that stage as components are too densely packed.

drift. For example, a persistent error of 0.1 rad in the angle can lead to an acceleration error of $0.98\,\mathrm{m}\cdot\mathrm{s}^{-2}$ from incorrectly rotating the gravity vector. If this is integrated over a period as short as 1 s, an error in the height estimate can be as large as 0.5 m. Hence, calculations that involve the integration of acceleration signals to obtain height estimates are undesirable.

The Zero Mean Sum

Fortunately, due to the interaction between buoyancy and gravity, the vessel will stay at a mean height of zero at the ocean surface. By including a fictitious measurement of the height, h_m, shown in Eq. 5.18, the filter can be tied to a zero mean value, which will stop any drift caused by integrating accelerations and angular rates.

$$h_m = 0 + \eta \tag{5.18}$$

The noise value, η for this measurement is the deviation of the wave height, $\eta = \sigma$. In this way, the measurement will be adjusted depending on the sea state. If η is less than the true deviation of the waves, h_m will be weighted more than the accelerometer measurement, resulting in suppression of the height estimate. On the other hand, if η is larger than the wave deviation, Eq. 5.18 will have a low weighting in the filter, and drift from the accelerometer measurement will be present in the estimate.

As wave power does not remain constant, η must be dynamic. Over time, the average power of the waves can be calculated and used to set η to match. The autocorrelation, $R_{hh} = \sigma^2$ at the

output, can be found by taking the inverse Fourier transform of $S_{hh}(jw)$ [28]. This can be used to gradually update the noise value of the zero mean measurement.

The zero mean assumption solves the issue of integrator drift in the model. Improving upon this, ocean waves can be assumed to follow a sinusoidal path. This is valid for deep sea waves, as the wave spectrum has a single peak. This modification can be achieved by using

$$h_i(\vec{x}, t) = \sqrt{2\Delta\omega_i S(\omega_i)}\sin(\omega_i t + \vec{k}_i \cdot \vec{x} + \gamma_i), \tag{5.19}$$

for the fictitious height measurement, as opposed to Eq. 5.18. The total wave height estimate is synthesised by summing up the component height state variables as

$$\hat{h} = \sum_{i=1}^{n} h_i, \tag{5.20}$$

which has a mean of zero by construction. Hence, the initial assumption made in Eq. 5.18 of a zero mean wave height measurement is not necessary and is not used. In this way, it is possible to obtain relative height estimates without double integration of the acceleration signal. Fig. 5.4 shows at which point in each oscillator, $\hat{h}_i$, is obtained for the sum. The summation of the height components takes into account the phase of each sinusoid, provided that the oscillator is tracking the signal.

Rotating Acceleration Measurements from Body to Inertial Frame

To obtain a_z^n, the vertical component of acceleration in the inertial frame used to synthesise the wave height, the measured body-frame acceleration signal must be rotated from its body-fixed frame, $\vec{a}^b$. Considering the mounting position of the sensor onboard the platform, the DH transformation in Eq. 5.21 is used to achieve the rotation, where $T(z_{j-1}, d_j)$ represents a translation of length d_j along the z_{j-1} axis, while $R(z_{j-1}, \theta_j)$ represents a rotation of angle θ_j with respect to the z_{j-1} axis [40].

$${}^{j-1}_{j}\mathcal{T} = T(z_{j-1}, d_j) \cdot R(z_{j-1}, \theta_j) \cdot T(x_j, a_j) \cdot R(x_j, \alpha_j) \tag{5.21}$$

$$\begin{bmatrix} a_x^n \\ a_y^n \\ a_z^n \end{bmatrix} = {}^{2}_{3}\mathcal{T} \cdot {}^{1}_{2}\mathcal{T} \cdot {}^{0}_{1}\mathcal{T} \cdot \vec{a}^b \tag{5.22}$$

Parameters for this transformation are shown in Table 5.1. From the inertial NED frame represented by joint 0, the vertical translation, h, is in joint 1, while roll, ϕ, and pitch, θ, are in joints 2 and 3 respectively.

Table 5.1: Table of Denavit-Hartenberg parameters for the estimator, with a transformation from the body frame, joint 3, to the NED frame, joint 0.

Joint	d	θ	a	α
0	0	0	0	π
1	h	$-\frac{\pi}{2}$	0	$\frac{\pi}{2}$
2	0	ϕ	0	$\frac{\pi}{2}$
3	0	θ	0	$-\frac{\pi}{2}$

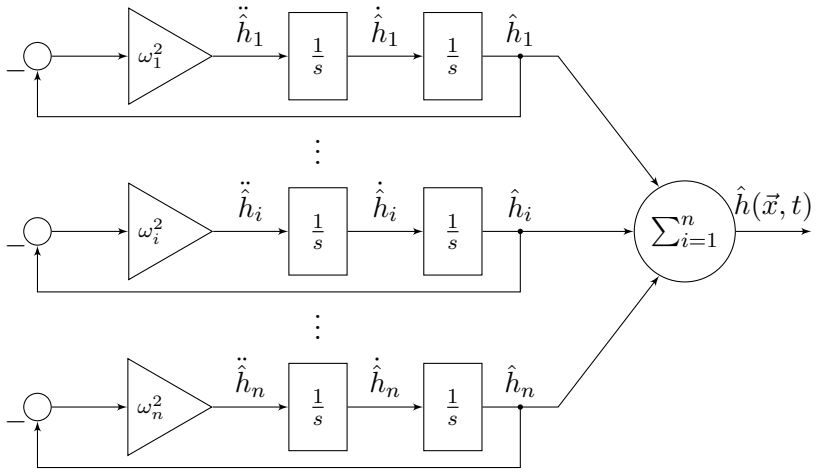

Figure 5.4: Total height estimate, $\hat{h}(\vec{x},t)$, is obtained by summing up the individual oscillator height outputs, $\hat{h}_i(\vec{x},t)$, where $i = 1 \dots n$. In the same way, the acceleration estimate, $\hat{\ddot{h}}(\vec{x},t)$, is obtained by summing up individual oscillator acceleration outputs, $\hat{\ddot{h}}_i(\vec{x},t)$.

5.3.2 Angular Rates

The gyroscope signal can be compared to the slope's time rate of change, $\dot{\vec{\Theta}}(\vec{x},t) = \mathbf{\Omega}(\vec{x},t)$, approximated by taking the time derivative of Eq. 5.28. Simplification of $\mathbf{\Omega}(\vec{x},t)$ in Eq. 5.23b is possible by using the dispersion relationship once again, as well as substituting $h_i(\vec{x},t)$ for $A_i \sin(\omega_i t + \vec{k}_i \cdot \vec{x} + \gamma_i)$, resulting in the angular rate measurement in Eq. 5.23c. $\Omega(\vec{x},t)$ represents the angular rate of the WG in the wave direction.

$$\mathbf{\Omega}(\vec{x},t) \approx \sum_{i=1}^{n} -A_i \omega_i \vec{k}_i \sin(\omega_i t + \vec{k}_i \cdot \vec{x} + \gamma_i) \tag{5.23a}$$

$$\mathbf{\Omega}(\vec{x},t) \approx \sum_{i=1}^{n} -\omega_i \vec{k}_i h_i(\vec{x},t) \tag{5.23b}$$

$$\Omega(\vec{x},t) \approx \sum_{i=1}^{n} \frac{-\omega_i^3}{g} h_i(\vec{x},t) \tag{5.23c}$$

5.3.3 Orientation from Magnetometer Measurements

The attitude of a body can be obtained using two vector measurements. Triaxial attitude determination (TRIAD) is an algorithm that determines the attitude of a body using only two vectors [52]. In the case of the WG, the two vector measurements used are a magnetometer reading that gives a North vector, and an averaged accelerometer reading giving a downwards gravity vector. The cross-product of these two vectors gives a third orthogonal vector, making a reference frame.

This attitude obtained from the TRIAD algorithm can be compared to the wave slope derived from Eq. 5.24a in the estimator. Although the magnetometer measurement is not used in the current study, a derivation of the slope is included for completeness.

Firstly, the slope is obtained by taking the partial derivative of Eq. 5.24a with respect to the spacial vector, $\vec{x}$. Following this, the wave slope vector, $\vec{\Theta}(\vec{x},t)$, is obtained by taking the arctangent of Eq. 5.24b.

$$h(\vec{x},t) = \sum_{i=1}^{n} A_i \sin(\omega_i t + \vec{k}_i \cdot \vec{x} + \gamma_i) \tag{5.24a}$$

$$\frac{\partial h(\vec{x},t)}{\partial \vec{x}} = \sum_{i=1}^{n} A_i \vec{k}_i \cos(\omega_i t + \vec{k}_i \cdot \vec{x} + \gamma_i) \tag{5.24b}$$

$$\boldsymbol{\Theta}(\vec{x},t) = \operatorname{atan}\left(\frac{\partial h(\vec{x},t)}{\partial \vec{x}}\right) \tag{5.24c}$$

The maximum slope expected is calculated in Eq. 5.25, by taking the shortest wavelength expected for wind waves, $\lambda_{\min} = 60\,\text{m}$, and the largest corresponding wave height, $h_{\max} = 5.10\,\text{m}$ [53]. Comparing the resulting slope from this calculation to an approximation obtained using Eq. 5.27 shows that the error in using the small angle approximation for the arctangent is approximately 0.2 %.

$$\Theta_{\text{measured}} = \operatorname{atan}\left(\frac{\mathrm{d}h_{\max}}{\mathrm{d}x_{\min}}\right) \tag{5.25}$$

$$\Theta_{\text{approx}} = \frac{\mathrm{d}h_{\max}}{\mathrm{d}x_{\min}} \tag{5.26}$$

$$\%_{\text{error}} = \frac{\Theta_{\text{approx}} - \Theta_{\text{measured}}}{\Theta_{\text{measured}}} \cdot 100 \tag{5.27}$$

Hence, the approximation $\operatorname{atan}(x) \approx x$ is used to simplify the slope calculation, resulting in Eq. 5.28. Simplifying this further, the dispersion relationship discussed in Chapter 4.1 is used. Substituting ω_i^2/g for $|\vec{k}_i|$ results in the magnetometer measurement in Eq. 5.29.

$$\boldsymbol{\Theta}(\vec{x},t) \approx \frac{\partial h(\vec{x},t)}{\partial \vec{x}} \tag{5.28}$$

$$\boldsymbol{m}(\vec{x},t) \approx \sum_{i=1}^{n} \frac{\omega_i}{g} \omega_i A_i \cos(\omega_i t + \vec{k}_i \cdot \vec{x} + \gamma_i) \tag{5.29}$$

The derivative state in the filter, $\dot{h}_i(\vec{x},t)$ in Eq. 5.30, can be substituted into Eq. 5.29 to give the final magnetometer measurement equation in Eq. 5.31.

$$\dot{h}(\vec{x},t) = \sum_{i=1}^{n} \omega_i A_i \cos(\omega_i t + \vec{k}_i \cdot \vec{x} + \gamma_i) \tag{5.30}$$

$$\boldsymbol{m}(\vec{x},t) \approx \sum_{i=1}^{n} \frac{\omega_i}{g} \dot{h}_i(\vec{x},t) \tag{5.31}$$

Fig. 5.5 shows how the wave height evolves over time and space. The slope of $h(\vec{x},t)$ is obtained by taking the partial derivative with respect to the spatial vector, $\vec{x}$, while the rate of change with respect to time is obtained by taking the partial derivative with respect to time t. In the current study, magnetometer measurements are not used, hence this is excluded from the measurement matrix.

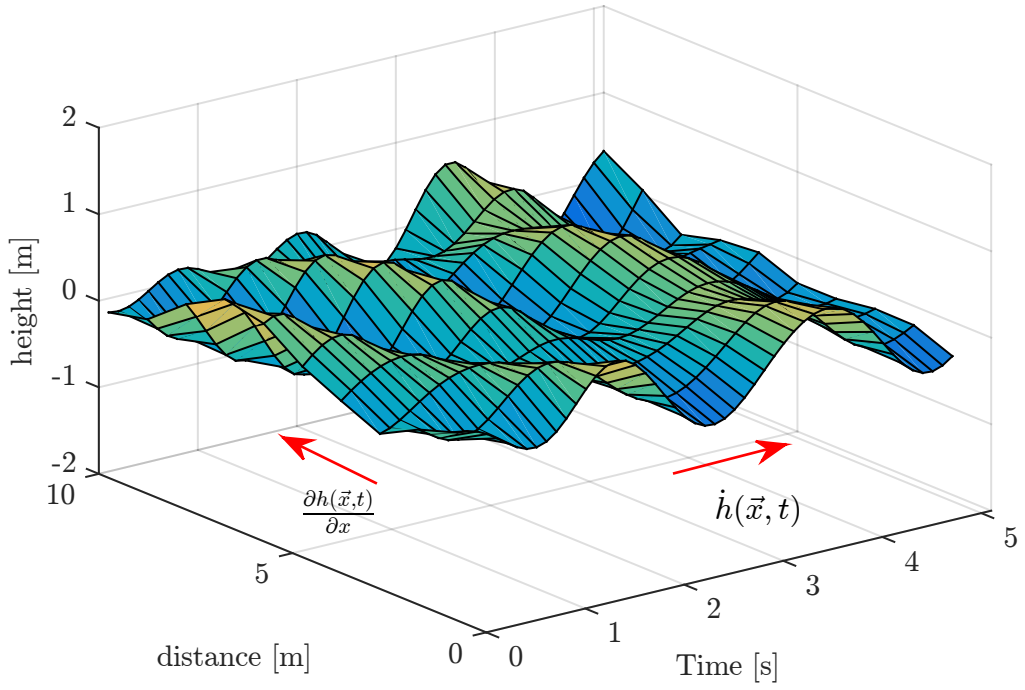

Figure 5.5: The time evolution of wave height as a function of a single spatial dimension, x. The slope direction, $\frac{\partial h(\vec{x},t)}{\partial x}$, and time rate of change, $\dot{h}(\vec{x},t)$, are shown by the red arrows.

5.3.4 Combining the Measurements

Eq. 5.32 is the combined measurement equation vector used to calculate the linearised measurement matrix, H_k in Eq. 5.33. H_k is calculated by taking the partial derivative of $\boldsymbol{y}(t)$ with respect to the state vector, $\boldsymbol{z}_k$. It consists of n 3×2 matrices for the frequency components, and one 3×2 matrix appended at the end for the θ and b_a state variables, where $i = 1, 2, \ldots, n$.

$$\boldsymbol{y}(t) = \begin{bmatrix} a_z^n \\ \Omega_y \\ \Omega_x \end{bmatrix} = \begin{bmatrix} \sum_{i=1}^{n} -\omega_i^2 h_i + g \\ \sum_{i=1}^{n} -\frac{1}{g}\omega_i^3 h_i \sin(\theta) \\ \sum_{i=1}^{n} -\frac{1}{g}\omega_i^3 h_i \cos(\theta) \end{bmatrix} \tag{5.32}$$

$$H_k = \frac{\partial \boldsymbol{y}(t)}{\partial \boldsymbol{z}_k} = \begin{bmatrix} -\omega_1^2 & 0 & -\omega_2^2 & 0 & \cdots & -\omega_i^2 & 0 & \cdots \\ -\frac{1}{g}\omega_1^3 \sin(\theta) & 0 & -\frac{1}{g}\omega_2^3 \sin(\theta) & 0 & \cdots & -\frac{1}{g}\omega_i^3 \sin(\theta) & 0 & \cdots \\ -\frac{1}{g}\omega_1^3 \cos(\theta) & 0 & -\frac{1}{g}\omega_2^3 \cos(\theta) & 0 & \cdots & -\frac{1}{g}\omega_i^3 \cos(\theta) & 0 & \cdots \end{bmatrix} \tag{5.33}$$

$$\begin{bmatrix} -\omega_n^2 & 0 & 0 & \sin(\theta) & 0 & \cos(\theta) \\ -\frac{1}{g}\omega_n^3 \sin(\theta) & 0 & \sum_{i=1}^{n} -\frac{1}{g}\omega_i^3 h_i \cos(\theta) & 0 & 0 & 0 \\ -\frac{1}{g}\omega_n^3 \cos(\theta) & 0 & \sum_{i=1}^{n} \frac{1}{g}\omega_i^3 h_i \sin(\theta) & 0 & 0 & 0 \end{bmatrix}$$

5.4 Process and Measurement Noise Calculations

Selecting appropriate values to populate the process noise matrix, Q_k in Eq. 2.23, and the measurement noise matrix, R_k in Eq. 2.24, is pivotal to optimal performance of the filter. Furthermore, the initial conditions for the error covariance matrix, P_0, is also important.

Meaningful values for process and measurement noise are estimated as there is no other reasonable method to derive them. Using a similar approach as in [54], sensible values for Q_k and R_k are found and used in the estimator.

5.4.1 Selection of Process Noise Values

Sources of uncertainty in the process model stem from discretisation and behaviour of the model. Assuming that the process noise states are uncorrelated, the discrete covariance matrix, Q_k, can be formed as a block diagonal matrix. The standard deviations, σ_{h_i} and $\sigma_{\dot{h}_i}$, are selected such that they correctly account for noise, the rate at which the state variable can change, and the effects of un-modelled dynamics. The resulting covariance matrix is shown in Eq. 5.35, where $\tilde{S}_{h_i}$ is the normalised wind wave spectrum amplitude to allow scaling of each component, and $\tilde{S}_{\dot{h}_i}$ its derivative.

$$Q_i = \begin{bmatrix} \sigma_{h_1}^2 \tilde{S}_{h_i} & 0 \\ 0 & \sigma_{\dot{h}_1}^2 \tilde{S}_{\dot{h}_i} \end{bmatrix} \tag{5.34}$$

$$Q_k = \text{diag}(Q_1, \cdots, Q_i, \cdots, Q_n, \sigma_\theta^2, \sigma_{\boldsymbol{b}_a}^2), \quad Q_k \in \mathbb{R}^{(2n+4)\times(2n+4)} \tag{5.35}$$

Process noise models are not available for the continuous model, hence the discrete noise values are inferred directly. This is carried out by considering each state variable component and assigning noise values depending on how the state is expected to evolve over time. On the basis that $\hat{h}$ may change by approximately 1 m in 10 min, a reasonable value for the height deviation of the peak frequency, σ_{h_1}, is calculated to achieve this rate of change as

$$\sigma_{h_1} T = \frac{1}{600}, \tag{5.36}$$

$$\sigma_{h_1} = 1.67 \times 10^{-2} \quad \text{[m/sample]}, \tag{5.37}$$

where T is the sampling rate of 0.1 s. Following this, each $\sigma_{h_i}^2$ must be scaled appropriately according to the height spectrum, ensuring that the contribution to the height by each component is weighted correctly. This is done by scaling the peak value, $\sigma_{h_1}^2$, with the respective normalised amplitude spectrum height, $\tilde{S}_{h_i}$, for each component.

The state variables h_i and $\dot{h}_i$ are coupled, as one is the time integral of the other. Hence it is not necessary to calculate both process deviations for each component, and the deviation for $\dot{h}_i$ can be set to zero, $\sigma_{\dot{h}_i}^2 = 0$. However, a possible benefit of having noise feed in from the derivative state is that it allows for smoother changes at the output, due to the integration. This can be verified through simulation of both cases under similar conditions.

Wind waves are produced from storms that develop over extended periods of time. As such, mean wave direction changes slowly over time. To assign a sensible noise value to this behaviour, a nominal storm that develops over a period of a day is used. Assuming that this storm can change the wave direction by π rad over this time, the noise value, σ_θ, that will allow this rate

of change to be achieved is

$$\sigma_\theta T = \frac{\pi}{3600 \cdot 12}\ , \tag{5.38}$$

$$\sigma_\theta = 7.27 \times 10^{-4} \quad \text{[rad/sample]}, \tag{5.39}$$

The selection of appropriate initial error covariance values is equally important for achieving good performance. The Ricatti equation in Eq. 5.40 is used to calculate P_k, where P_{k+1}^- in Eq. 5.41 is the prediction error covariance update.

$$P_k = (I - K_k H_k) P_k^- \tag{5.40}$$

$$P_{k+1}^- = F_k P_k F_k^T + Q_k \tag{5.41}$$

Assuming mean direction is uniformly distributed between $-\pi$ and π, and the wave direction is unknown, then the initial error covariance for this state, P_θ, can be calculated as

$$P_\theta = 2\int_0^\pi x^2 f(x)\mathrm{d}x, \tag{5.42}$$

$$P_\theta = 2\int_0^\pi x^2 \frac{1}{2\pi}\mathrm{d}x = \frac{\pi^2}{3}. \tag{5.43}$$

Bias is set to an initial value of zero, and a corresponding error covariance for the state is set as $P_{b_a} = 0$. For the h_i and $\dot{h}_i$ state variables, initial error covariance is constructed similarly to Q_i. Only P_{h_1} and $P_{\dot{h}_1}$ are selected, then the remaining values are calculated as

$$P_{h_i} = P_{h_1}\tilde{S}_i, \tag{5.44}$$

$$P_{\dot{h}_i} = P_{\dot{h}_1}\tilde{S}_{\dot{h}_i}\omega_i^2, \tag{5.45}$$

giving the initial error covariance matrix as a block diagonal matrix

$$P_0 = \mathrm{diag}(P_{h_1}, P_{\dot{h}_1}, \cdots, P_{h_i}, P_{\dot{h}_i}, \cdots, P_{h_n}, P_{\dot{h}_n}, P_\theta, P_{\boldsymbol{b}_a}), \quad P_k \in \mathbb{R}^{(2n+4)\times(2n+4)}. \tag{5.46}$$

5.4.2 Selection of Measurement Noise Values

Similarly, the measurement noise values of the sensors are assumed to be independent, resulting in a diagonal measurement noise matrix. Sensor noise and bias values are obtained from device manufacturers' datasheets. However, other sources of error larger than sensor accuracy are present and must be accounted for. Selection of covariances depends on operations applied to measured variables. For the acceleration, the noise value provided in the datasheet, $\boldsymbol{\eta}$, only forms part of the uncertainty. Eq. 5.47 shows how rotation errors in $T(\theta)$ used to obtain inertial frame acceleration, $\vec{a}^n$, from the measured body frame acceleration, $\vec{a}^b$, can play more of a role than the error given in the datasheet; meaning small uncertainties in rotations can cause large errors in acceleration to occur.

$$\vec{a}^b = T^{-1}(\theta)(\vec{a}^n + g) + \boldsymbol{\eta}, \tag{5.47}$$

$$\vec{a}^n = T(\theta)(\vec{a}^b - \boldsymbol{\eta}) - \vec{g}, \tag{5.48}$$

where $\vec{a}^b$ is the measured body frame acceleration, and a^n is the desired inertial frame acceleration. The angle's error contribution in acceleration can be shown by taking the covariance of

$\vec{a}^n = f(\theta, \vec{a}^b, \boldsymbol{\eta}, \vec{g})$ using the approximation in Eq. 5.49, such that

$$\text{cov}(a^n) \approx \left(\frac{\partial f}{\partial \theta}\right)^2 \sigma_\theta^2 + \left(\frac{\partial f}{\partial \eta}\right)^2 \sigma_\eta^2, \tag{5.49}$$

$$\text{cov}(a^n) \approx \frac{\partial (T(\theta))}{\partial \theta} \vec{a}^b \sigma_\theta^2 \left(\frac{\partial (T(\theta))}{\partial \theta} \vec{a}^b\right)^T + T(\theta) \sigma_\eta^2 (T(\theta))^T, \tag{5.50}$$

where σ_θ^2 is the covariance of θ, and σ_η^2 is the noise covariance [55]. The first term in Eq. 5.50 is the error in θ and can contribute the most to the error in acceleration. The noise value for the acceleration measurement, σ_a, is selected based on datasheet noise values for the accelerometer used, and un-modelled accelerations from vibration. For angular rate measurements, uncertainty due to the approximation used in calculating Eq. 5.23b is greater than the sensor accuracy values provided in the datasheet. Appropriate values for the angular rate measurements about the x and y axes, σ_x and σ_y respectively, are selected based on this larger uncertainty, resulting in $R_k = \text{diag}(\sigma_a^2, \sigma_x^2, \sigma_y^2)$.

A check for the noise value selected being of the correct order of magnitude is the Signal to Noise Ratio (SNR), which is the signal power divided by the noise power. An SNR less than approximately 0.1 results in poor tracking, with the estimate lagging the measurement, while an acceptable SNR is greater than 1 [36]. This is used as a check when assessing the performance of the filter. A summary of the process and measurement noise standard deviations is provided in Table 5.2, with a sampling time of $T = 0.1$ s.

Table 5.2: Summary of process and measurement noise standard deviations used in the filter, with $T = 0.1$ s.

Type	Parameter	Value	Unit (per sample)
Process	σ_{h_1}	1.67×10^{-2}	m
	σ_{h_2}	1.05×10^{-2}	m
	σ_{h_3}	5.68×10^{-3}	m
	σ_{h_4}	2.91×10^{-3}	m
	σ_{h_5}	1.47×10^{-3}	m
	σ_{h_6}	7.41×10^{-4}	m
	$\sigma_{\dot{h}_1}$	1.00×10^{-3}	$\text{m} \cdot \text{s}^{-1}$
	$\sigma_{\dot{h}_2}$	1.10×10^{-3}	$\text{m} \cdot \text{s}^{-1}$
	$\sigma_{\dot{h}_3}$	1.03×10^{-3}	$\text{m} \cdot \text{s}^{-1}$
	$\sigma_{\dot{h}_4}$	9.19×10^{-4}	$\text{m} \cdot \text{s}^{-1}$
	$\sigma_{\dot{h}_5}$	8.07×10^{-4}	$\text{m} \cdot \text{s}^{-1}$
	$\sigma_{\dot{h}_6}$	7.05×10^{-4}	$\text{m} \cdot \text{s}^{-1}$
	σ_θ	1.00×10^{-4}	rad
	σ_{b_a}	1.00×10^{-6}	$\text{m} \cdot \text{s}^{-1}$
Measurement	σ_a	9.30×10^{-4}	$\text{m} \cdot \text{s}^{-2}$
	σ_x	4.00×10^{-2}	$\text{rad} \cdot \text{s}^{-1}$
	σ_y	4.00×10^{-2}	$\text{rad} \cdot \text{s}^{-1}$

5.5 Observability and Stability of the Estimator

A system is said to be observable if all internal states can be determined from knowledge of the input and output of the system, over a finite period of time [56]. Eq. 5.53 shows the observability matrix of a linearised system, calculated using the state transition and measurement matrices, Eqs. 5.51 and 5.52 respectively.

$$F = \frac{\partial f(\boldsymbol{x}, \boldsymbol{u})}{\partial \boldsymbol{z}}, \tag{5.51}$$

$$H = \frac{\partial g(\boldsymbol{z})}{\partial \boldsymbol{z}}, \tag{5.52}$$

$$\mathcal{O} = \begin{bmatrix} H & HF & HF^2 & \cdots & HF^{n-1} \end{bmatrix}^T, \tag{5.53}$$

where n is the number of states. For the system to be observable, $\mathcal{O}$ must have full rank [57]. The number of unobservable states is the difference between the number of state variables and the numerical rank of $\mathcal{O}$. However, this is not a suitable method for systems that have more than a couple of states. Alternatively, the condition number of $\mathcal{O}$, which is its sensitivity to inversion, is used as a measure of observability [58].

If the oscillator frequencies were allowed to change independently of one another, a situation arises where more than one oscillator locks onto the same frequency, leading to unobservable states in the system. This problem is avoided in the fixed frequency configuration, where the states change in unison and do not overlap. However, as the components are grouped closer and closer together, the condition number of $\mathcal{O}$ increases, indicating an unobservable system.

5.6 Spectral Estimation Summary

From this analysis, the estimation strategy chosen is the non-parametric method. In addition, the zero mean sinusoidal sum assumption is used to avoid integration drift, while also reducing the work the estimator needs to do. As more parameters are used in the estimation, the system becomes unobservable. For this reason, a restriction is imposed on the number of frequency components used in the estimator. Chapter 6 gives an in-depth analysis of the peak frequency estimation method used to provide the Kalman filter with an estimate of ω_p.

This page has been intentionally left blank.

Chapter 6

Peak Frequency Estimation

In the previous chapter, the peak frequency of the wind wave spectrum is used in the estimation strategy. This chapter describes, in depth, methods of estimating the peak frequency. Firstly, a sinusoidal estimator is developed. After this, a phase-locked loop is designed to track the peak frequency. A discussion of the benefits given by each of these methods is presented.

6.1 Sinusoidal Estimator

Using noisy acceleration measurements, the peak frequency, ω_p, can be estimated using a three-state Extended Kalman filter [36]. Firstly, considering the ideal case in which the signal contains a single sinusoid, the formulation is as follows.

An estimator similar to the sinusoidal oscillator discussed in Chapter 5.2.1 is used, where Eq. 6.1 is the state equation used to track the sinusoid's amplitude and phase. The difference here is that the frequency, ω, of the sinusoid is not fixed. To track the frequency's evolution, a third state modelled as a random walk process of the unknown frequency squared, $p = \omega^2$, is added [36]. The resultant model in state space form in Eq. 6.4 shows the three states required for this estimator, namely the vertical displacement, h, its rate of change, $\dot{h}$, and p.

$$\ddot{h} = -\omega^2 h \tag{6.1}$$

$$\dot{p} = u_p \tag{6.2}$$

$$\boldsymbol{z} = \begin{bmatrix} h & \dot{h} & p \end{bmatrix}^T \tag{6.3}$$

$$\begin{bmatrix} \dot{h} \\ \ddot{h} \\ \dot{p} \end{bmatrix} = \begin{bmatrix} 0 & 1 & 0 \\ -p & 0 & 0 \\ 0 & 0 & 0 \end{bmatrix} \begin{bmatrix} h \\ \dot{h} \\ p \end{bmatrix} + \begin{bmatrix} 0 \\ 0 \\ u_p \end{bmatrix} \tag{6.4}$$

The rate at which the frequency state, p, can change is of particular importance. If it evolves at a rate in the same order of magnitude as the h and $\dot{h}$ states, the estimator's process model will no longer be slowly time varying, and will result in not being able to analyse Eq. 6.4 as if it is linear. Hence a time scale separation is required between the dynamics of p and the remaining two states [49]. This separation is possible, since the peak frequency dynamics have a time constant in the order of several hours, which is much greater than the time constant of the dynamics of height and its derivative [59].

The system dynamics matrix is obtained from Eq. 6.4 using Eq. 6.5. This equation is then discretised using the first two terms of the Taylor Series approximation, leading to the final form in Eq. 6.7, where T is the sampling period [36].

$$F = \frac{\partial f(\boldsymbol{z}, \boldsymbol{u})}{\partial \boldsymbol{z}} \tag{6.5}$$

$$F = \begin{bmatrix} 0 & 1 & 0 \\ -p & 0 & -h \\ 0 & 0 & 0 \end{bmatrix} \tag{6.6}$$

$$F_k = \exp(FT) \approx \begin{bmatrix} 1 & T & 0 \\ -pT & 1 & -hT \\ 0 & 0 & 1 \end{bmatrix} \tag{6.7}$$

For the measurement equations in Eq. 6.8, vertical acceleration is used. The linearised output matrix is shown in Eq. 6.9.

$$g(\boldsymbol{z}) = -ph \tag{6.8}$$

$$H = \frac{\partial g(\boldsymbol{z})}{\partial \boldsymbol{z}} = \begin{bmatrix} -p & 0 & -h \end{bmatrix} \tag{6.9}$$

6.1.1 Process and Measurement Noise

A non-zero noise value is associated with the p state, hence the continuous covariance matrix is

$$Q_c = \begin{bmatrix} \sigma_{h_i}^2 & 0 & 0 \\ 0 & \sigma_{\dot{h}_i}^2 & 0 \\ 0 & 0 & \sigma_p^2 \end{bmatrix}, \tag{6.10}$$

where the covariance, σ_p^2, determines the rate at which the frequency state will change. The states h_i and $\dot{h}_i$ can also vary, and are assigned corresponding covariance values $\sigma_{h_i}^2$ and $\sigma_{\dot{h}_i}^2$ respectively. As a slow changing frequency is desired, σ_p^2 must be relatively small [36]. The discretised equivalent of Q_c used in the Kalman filter is calculated as

$$Q_k = \int_0^T F_k Q_c F_k^T, \tag{6.11}$$

$$Q_k = \int_0^T \begin{bmatrix} 1 & \tau & 0 \\ -p\tau & 1 & -h\tau \\ 0 & 0 & 1 \end{bmatrix} \begin{bmatrix} \sigma_{h_i}^2 & 0 & 0 \\ 0 & \sigma_{\dot{h}_i}^2 & 0 \\ 0 & 0 & \sigma_p^2 \end{bmatrix} \begin{bmatrix} 1 & -p\tau & 0 \\ \tau & 1 & 0 \\ 0 & -h\tau & 1 \end{bmatrix} \mathrm{d}\tau, \tag{6.12}$$

$$Q_k = \begin{bmatrix} \frac{1}{3}\sigma_{\dot{h}}^2 T^3 + \sigma_h^2 T & \frac{1}{2}(\sigma_{\dot{h}}^2 - \sigma_h^2 p)T^2 & 0 \\ \frac{1}{2}(\sigma_{\dot{h}}^2 - \sigma_h^2 p)T^2 & \frac{1}{3}(\sigma_h^2 p^2 + \sigma_p^2 h^2)T^3 + \sigma_{\dot{h}}^2 T & -\frac{1}{2}h\sigma_p^2 T^2 \\ 0 & -\frac{1}{2}h\sigma_p^2 T^2 & \sigma_p^2 T \end{bmatrix}. \tag{6.13}$$

6.1.2 Propagation of States

State propagation of the h and $\dot{h}$ states is carried out using the nonlinear differential equations derived from Eq. 6.1, as opposed to using the fundamental matrix composed of linearised

equations, $\boldsymbol{z}_{k+1} = F_k \boldsymbol{z}_k$ [36]. This is the preferred method as numerical integration is more accurate than using the linearised equations, which are only necessary for calculating the error covariance, P_k, and Kalman gain, K_k. Algorithm 2 shows the Euler integration used for state propagation, the asterisk denoting values obtained from a numerical integration.

Algorithm 2 Euler integration for nonlinear state propagation

procedure StatePropagation($\dot{\hat{\boldsymbol{h}}}_{k-1}$, $\hat{\boldsymbol{h}}_{k-1}$, T_s)
  $\dot{\hat{\boldsymbol{h}}}^*_k = \dot{\hat{\boldsymbol{h}}}_{k-1}$
  $\hat{\boldsymbol{h}}^*_k = \hat{\boldsymbol{h}}_{k-1}$
  $T = 0$
  $T_p = 0.001$
  while $T < T_s$ **do**
    $\ddot{\hat{\boldsymbol{h}}}^*_k = -\hat{\boldsymbol{\omega}}^2 \circ \hat{\boldsymbol{h}}^*_k$
    $\dot{\hat{\boldsymbol{h}}}^*_k = \dot{\hat{\boldsymbol{h}}}^*_{k-1} + T\ddot{\hat{\boldsymbol{h}}}^*_k$
    $\hat{\boldsymbol{h}}^*_k = \hat{\boldsymbol{h}}^*_{k-1} + T\dot{\hat{\boldsymbol{h}}}^*_k$
    $T = T + T_p$
  end
  $\dot{\hat{\boldsymbol{h}}}_k = \dot{\hat{\boldsymbol{h}}}^*_k$
  $\hat{\boldsymbol{h}}_k = \hat{\boldsymbol{h}}^*_k$

For each time step T_s, the states will be propagated in this way, where T_p is the propagation period, and $\circ$ denotes an element wise multiplication. After the calculation performed in Algorithm 2, the vector states, $\hat{\boldsymbol{h}}_k$, and $\dot{\hat{\boldsymbol{h}}}_k$, are summed up to obtain the total height and its rate of change, respectively.

6.2 Phase-Locked Loop

The preferred peak frequency estimation technique is a Phase-Locked Loop (PLL), an automatic control system traditionally used for synchronisation purposes. It is used to estimate the peak frequency, ω_p, in the wave spectrum. Fig. 6.2 shows an overview of the PLL used to acquire ω_p, which is fed into a Kalman filter to estimate the amplitude, phase, and direction of frequency points scaled by ω_p, as shown in Fig. 6.1.

The PLL implementation provides the speed required for the overall prediction goal at the cost of bandwidth; it will only work over a very narrow band of frequencies. Thus, in this implementation, it is only used to obtain the peak frequency, then the Kalman filter can estimate the energy around that peak to generate a complete sea state estimate. The purpose of the PLL is to give the best guess of the possible location of the spectrum to allow the most energy to be captured by the Kalman filter and hence improve the overall estimation.

6.2.1 Phase-Locked Loop Components

A PLL comprises three main parts, namely a phase detector, loop filter, and a voltage controlled oscillator (VCO) [60]. To add to these elements, a bandpass pre-filter is included. Knowing the expected frequency range for the desired output allows band passing to reduce noise and

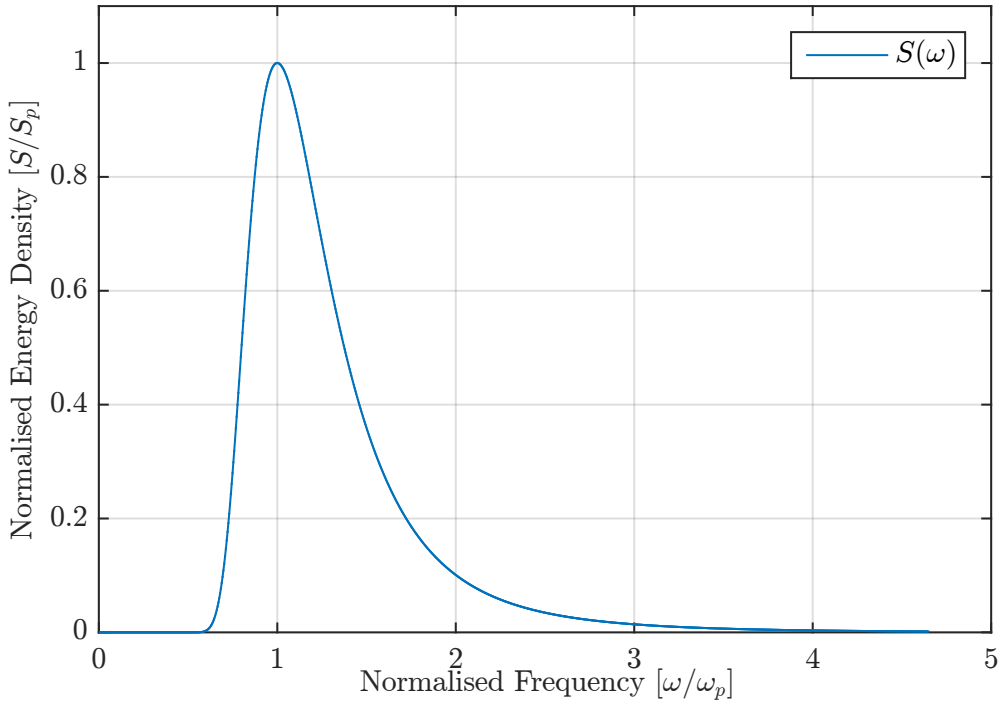

Figure 6.1: The normalised wave energy density spectrum, $S(\omega)$, has an invariant shape for different wind speeds.

unwanted signals entering the PLL system considerably [61]. The frequency range for wind generated waves is from $0.5\,\mathrm{rad}\cdot\mathrm{s}^{-1}$ to $6\,\mathrm{rad}\cdot\mathrm{s}^{-1}$.

Phase Detector

The phase detector compares the signal of interest, $u(t)$, to the direct (in-phase) and quadrature components of the VCO; D and Q, respectively.

$$D = \frac{1}{2\pi n}\int_0^{2\pi n} \sin(\omega t)u(t)\mathrm{d}(\omega t) \tag{6.14}$$

$$Q = \frac{1}{2\pi n}\int_0^{2\pi n} \cos(\omega t)u(t)\mathrm{d}(\omega t) \tag{6.15}$$

This integration over an integral number of cycles, n, can be implemented as shown in Fig. 6.2, using Eq. 6.16, where $T_f = 2\pi n/\omega_p$, and the phase error, ϵ, is computed using the four-quadrant arctangent in Eq. 6.17.

$$F(s) = \frac{1-\exp(-sT_f)}{sT_f}u(s) \tag{6.16}$$

$$\epsilon = \mathrm{atan2}(Q, D) \tag{6.17}$$

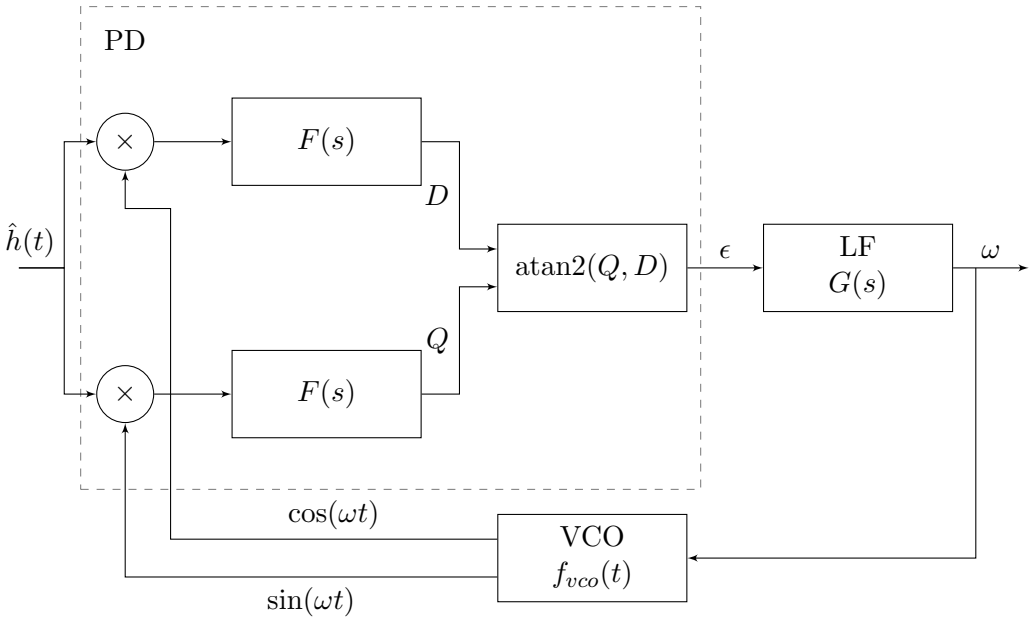

Figure 6.2: Phase-locked loop for estimating peak frequency, ω_p, of wind wave spectrum, using Phase Detector (PD), Loop Filter (LF) and Voltage Controller Oscillator (VCO) components.

Loop Filter

The PLL can be characterised by the plant model shown in Eq. 6.18, a system with a single integrator and gain contributions from the phase detector, loop filter and voltage controller oscillator as k_{pd}, k_{lf}, and k_{vco} respectively.

$$P(s) = k_{\text{pd}} k_{\text{lf}} k_{\text{vco}} \frac{1}{s}. \tag{6.18}$$

A time scale difference is required between the PLL loop bandwidth and the signal of interest's centre frequency for optimal performance [61]. To this end, the loop filter designed, $G(S)$, must have a low gain. This is achieved by setting the boundary condition for the gain cross-over frequency at least an order of magnitude lower than the dynamics of the Kalman filter. Hence the requirement set is a gain cross-over frequency of 0.02π rad $\cdot$ s^{-1} (0.01 Hz).

Furthermore for improved performance, high frequencies outside the region of interest must be attenuated. A roll-off at 0.2π rad $\cdot$ s^{-1} is added as another requirement for the loop filter. Eq. 6.19 is the resulting loop filter for the PLL, where the filter gain is sufficiently low, $K \approx 1 \times 10^{-5}$.

$$G(s) = K \frac{376.1s + 1}{s(0.05s + 1)} \tag{6.19}$$

Voltage Controller Oscillator

From the loop filter, a signal proportional to the frequency difference, ω_e, is fed to the VCO. In response, the VCO adjusts its frequency proportionally, driving the phase error to zero. With this type of behaviour, the VCO can be modelled as an integrator. Equation 6.20 is the model

of the VCO used to create a sinusoidal signal and its quadrature,

$$f_{vco}(t) = \exp(i(\omega_c t + w_e)), \tag{6.20}$$

where ω_c is the VCO's quiescent frequency. This completes the feedback loop in Fig. 6.2.

6.3 Peak Frequency Estimation Summary

The PLL uses height estimates from the Kalman filter to track the peak frequency, which is fed back into the Kalman filter. To maintain stability in this feedback loop, the PLL subsystem must appear linear and time invariant to the Kalman filter. The concept of time-scale separation is used to decouple the PLL and KF dynamics. Hence the PLL dynamics are slower than the dynamics of the Kalman filter presented in Chapter 5.

Furthermore, the response speed of the system can be improved at the cost of tracking noise. This trade off limits how fast the system can be while still producing a useful output, ultimately limiting the required prediction capabilities of a few wavelengths ahead.

The final peak frequency estimation method used is the PLL in a Kalman filter form, combining the benefits of the sinusoidal estimator and phase-lock strategy.

This page has been intentionally left blank.

Chapter 7

Experiment Design

This chapter describes in detail, experiments conducted to verify the theory laid out in the previous chapters. Enough detail is provided so that these tests can be replicated and verified for both the simulation (Section 7.1) and the wave tank experiment (Section 7.2).

7.1 Simulation Design

7.1.1 Matlab Simulation Environment

The system designed in previous chapters is set up for verification in the Matlab/Simulink simulation environment. Fig. 7.1 shows the general set-up of the simulation used in this text, comprising two main parts. In the first, waves are produced then passed through the full WG model, then measurements are taken from the point of view of the WG model. This is the simulation of real world behaviour. The second part is the estimator, where measurements are processed using a Kalman filter that feeds into a replica of the system, having a sea state estimator as well as a WG model.

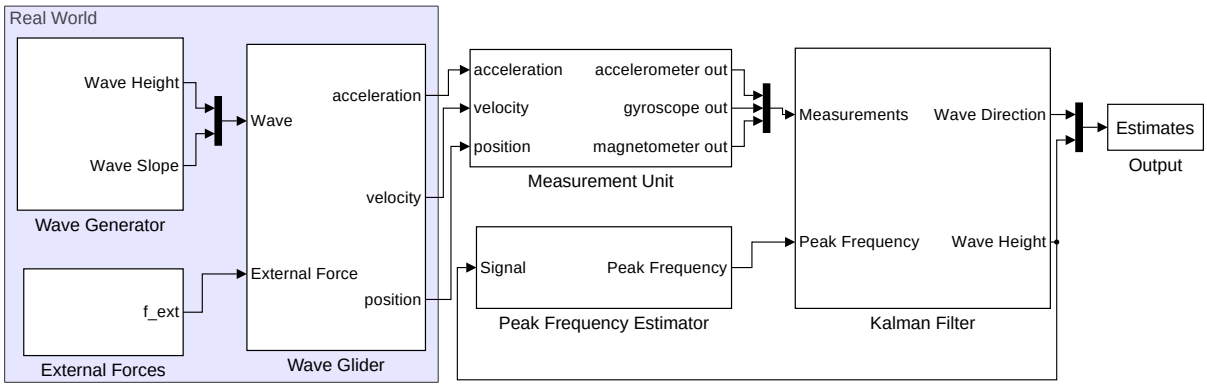

Figure 7.1: Overview of MATLAB simulation for wind wave generation and sea state estimation.

Simulation Parameters

A reasonable simulation time is required that provides efficient computation while avoiding aliasing of the signals. The highest frequency present in the wave spectra of interest of $f_{\max} = 1\,\text{Hz}$ gives a required minimum sampling time of 0.5 s to satisfy the Nyquist sampling criteria, shown in Eq. 7.2. This leads to a conservative simulation time of $T = 1 \times 10^{-1}\,\text{s}$ for ocean dynamics.

$$\Delta t = \frac{1}{f_{\max}} \tag{7.1}$$

$$f_{Nyquist} = \frac{1}{2\Delta t} \tag{7.2}$$

However, simulating the WG responses requires a smaller simulation time of $T = 1 \times 10^{-3}\,\text{s}$ to capture the faster dynamics present in the model.

7.2 Wave Tank Experiment Design

For proof of concept validation of the 2D sea state estimator, an experiment was set up in a narrow channel wave tank, shown in Fig. 7.5. The narrow width allows for long-crested random waves to be established.

7.2.1 Wave Generator

Two types of wave generators are commonly used, each with a different goal [62]. The first type, a flap wave generator, is used for modelling deep sea behaviour, while the second type, a piston wave generator, models shallow sea behaviour. These two generators are shown in Fig. 7.2. To model deep sea wind waves, the flap paddle generator is chosen, giving the correct orbital pattern similar to deep sea wind waves.

Once the type of wave generator is selected, the next design consideration is the paddle size. Guidelines dictate that it should extend at least 35 % of the hinge depth above the waterline. In addition, a recommended maximum displacement of $\pm 12°$ is used [62]. At a width of 80 mm, the waves generated are long-crested random waves, ideal for the conducted experiment. In addition, the tank length is long enough to have the three sections required for accurate replication of waves as follows:

1. A distance twice the hinge depth, directly in front of the paddle for the waves to reach steady-state (a fully developed condition).
2. A model zone that is long enough for the platform. As this experiment is for a stationary platform, this region need not be very long.
3. A wave absorption section to reduce the reflection of waves at the opposite end of the tank.

7.2.2 Measurement Platform

Considerations for the measurement platform are weight and buoyancy. To minimise the weight and maximise buoyancy, a combination of aluminium and polystyrene is used. The platform

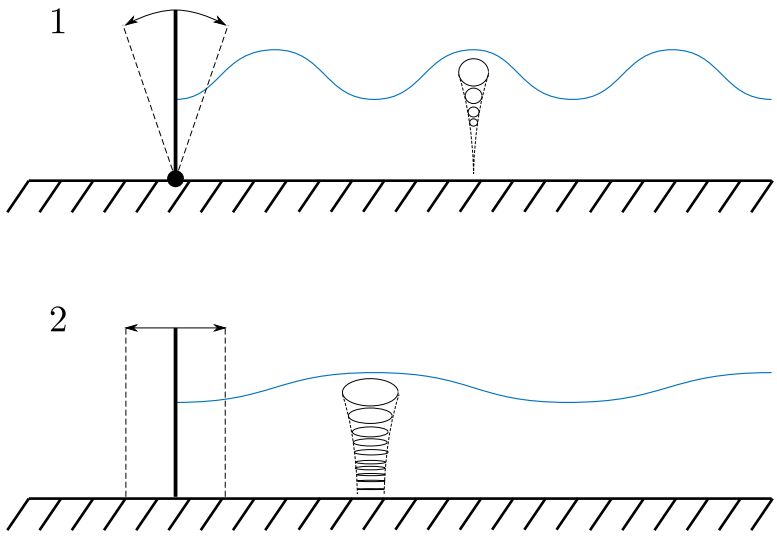

Figure 7.2: Wave generator types: (1) flap paddle generator for deep water waves, where most of the particle motion is observed at the surface. (2) piston generator for shallow water waves, with more horizontal motion of the water particles (adapted from [62]).

shape is designed to resemble the WG. However, to accommodate the sensing device, the height of the measurement platform is not to scale with the WG, which is acceptable as this dimension is of less importance.

To evaluate the performance of the estimator, height measurement reference data (ground truth) must be obtained. This is achieved using the measurement set-up shown in Fig. 7.3. A 1 m long beam, fixed to the tank at one end, uses a potentiometer as a hinge and hence allows the beam angle, α_1, relative to the tank to be measured. The other end of the beam is attached to the platform in the same way, allowing for the angle, α_2, to be measured relative to the beam. Using these two potentiometer readings, the pitch angle and height, θ_{pot} and h_m respectively, of the platform relative to the fixed tank frame can be calculated using Eqs. 7.3 and 7.5 to verify the estimator results.

$$\theta_{pot} = \alpha_2 - \alpha_1, \tag{7.3}$$

$$h_{pot} = R\sin(\alpha_1), \tag{7.4}$$

$$h_m = H - h_{pot}, \tag{7.5}$$

where H is the zero mean water level in the tank relative to the hinge fixed to the tank, h_{pot} is the calculated height from the potentiometer, and h_m is the final measured height. To eliminate any bias that arises in the height measurement, the mean height is subtracted from the measurements before being compared to the estimator results. The dimensions of the tank, platform and paddle are summarised in Table 7.2.

Matlab provides a sensor package that logs inertial sensor data from remote mobile devices directly into the workspace. For its ease of use, this package is used for the acceleration and angular rate measurements required. An added benefit to this is that the data are logged with a Coordinated Universal Time (UTC) stamp, which is used to synchronise data with other recording devices in the system. Matlab R2013a is used with the iOS Sensors v15.1 package for data

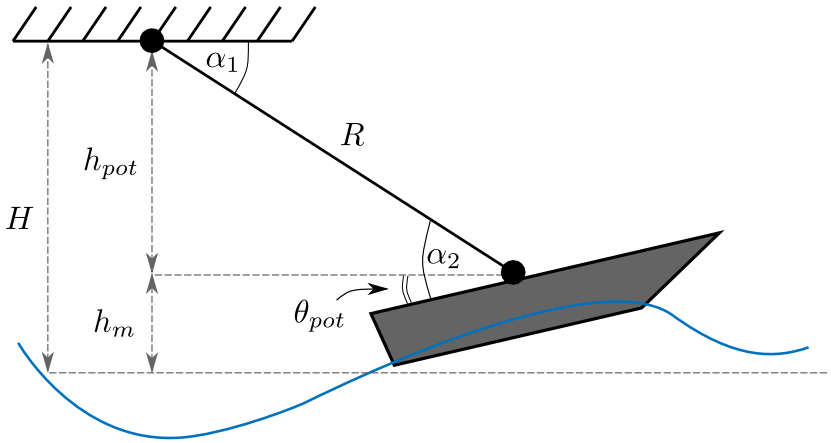

Figure 7.3: Measurement platform for wave tank experiment, with α_1 and α_2 as the angles to be measured. The height h_{pot} is calculated using α_1 and R. Finally, the difference between H and h_{pot} is computed as the final height, h_m.

acquisition. An iPhone 5 with iOS 10.1 operating system is used as the measurement device. It has an STMicroelectronics L3G4200D gyroscope, and an STMicroelectronics LIS331DLH Inertial Measurement Unit (IMU). The potentiometer readings are converted to angle measurements using a Particle Photon micro-controller shown in Fig. 7.4. The ADC count values for two known positions, 0° and 90° in Table 7.1, are taken and used to calculate the relationship between beam angle and voltage from the potentiometer. This device also records potentiometer values with a UTC stamp obtained from a Simple Network Time Protocol (SNTP) server, which is used to synchronise the potentiometer and IMU recordings.

7.2.3 Estimator

The 2D estimator developed in Chapter 6 is used in this experiment, with slight modifications. As the wave tank is located indoors and the scale of the experiment is small, GPS data are unreliable and hence not used. In addition, the spectral behaviour of deep sea wind waves cannot be reproduced due to the tank's dimensions. The model zone of the wave tank is 2 m, where the waves are regarded to be fully developed. If this is the longest wavelength, $\lambda_{\max}$, to be measured in the tank, a water depth, D, of at least 1 m is required to satisfy the deep sea condition, $D > \lambda/2$, explained in Chapter 2.2.2.

$$k_{\max} = 2\pi/\lambda_{\max} \tag{7.6}$$

$$\omega^2_{\max} = g k_{\max} \tanh(k_{\max} D) \tag{7.7}$$

Table 7.1: ADC calibration values used for potentiometers. The ADC count values for two known positions, 0° and 90°, are taken and used to calculate the relationship between beam angle and voltage from the potentiometer.

	0°	90°
α_1 Potentiometer	1764	343
α_2 Potentiometer	4090	2445

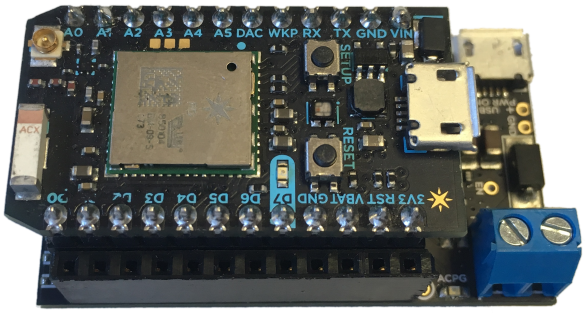

Figure 7.4: Particle Photon micro-controller used to record potentiometer values for angle and height calculations. The device is connected to the internet and allows for data collected to be time stamped using UTC time.

Table 7.2: Dimensions of the wave tank, paddle and platform used in the experiment.

	Length [mm]	Width [mm]	Depth [mm]
Tank	5000	80	250
Paddle	N/A	70	350
Platform	210	55	100

However, the wave tank has a depth of $D = 0.2\,\text{m}$, so Eq. 7.6 and 7.7 will give $k_{\max} = 3.14\,\text{rad} \cdot \text{m}^{-1}$ and $\tanh(k_i D) = 0.57$ respectively. Since $\tanh(kD) \not\approx 1$, it cannot be ignored and the full dispersion relationship in Eq. 7.7 must be used. The wave tank experiment is an illustration of the estimation strategy developed. By using the full wave dispersion relationship, the data obtained from the experiment will provide insight into the performance of the estimator when the deep sea condition is met.

Three measurement variables are required for the estimator to function, namely linear accelerations in heave and surge, and the angular rate about the pitch axis. The estimator states used are vertical height, $\boldsymbol{h}$, and its derivative, $\dot{\boldsymbol{h}}$. As the platform is restricted in roll and sway, the state for mean wave direction is omitted, resulting in a reduced state vector in Eq. 7.8. The four logarithmically distributed frequency points shown in Eq. 7.9 are chosen for the normalised frequency vector which is scaled by the peak frequency, ω_p.

$$\boldsymbol{z} = \begin{bmatrix} h_1, & \dot{h}_1, & h_2, & \dot{h}_2, & h_3, & \dot{h}_3, & h_4, & \dot{h}_4 \end{bmatrix}^T \tag{7.8}$$

$$\boldsymbol{\omega} = \omega_p \cdot \begin{bmatrix} 1, & 1.12, & 1.26, & 1.45 \end{bmatrix} \tag{7.9}$$

The body fixed acceleration measurements in Eq. 7.11 are transformed to the inertial frame using Eq. 7.10. Combining this acceleration with the angular rate measurement in Eq. 7.12 will give the measurement equation in Eq. 7.11. Following this, the measurement matrix, H, can

be constructed as shown in Eq. 7.14.

$$R_I^b = \begin{bmatrix} \cos(\theta) & 0 & \sin(\theta) \\ 0 & 1 & 0 \\ -\sin(\theta) & 0 & \cos(\theta) \end{bmatrix} \tag{7.10}$$

$$\vec{a}^b = R_I^b \begin{bmatrix} a_x \\ 0 \\ \Sigma_i - \omega_i^2 h_i \end{bmatrix} - \begin{bmatrix} 0 \\ 0 \\ g \end{bmatrix} \tag{7.11}$$

$$\Omega = \sum_i \frac{-\omega_i^3 h_i}{g} \tag{7.12}$$

$$\boldsymbol{g}(t) = \begin{bmatrix} \vec{a}^b \\ \Omega \end{bmatrix} \tag{7.13}$$

$$H = \frac{\partial \boldsymbol{g}(t)}{\partial \boldsymbol{z}} = \begin{bmatrix} -\omega_1^2 \cos(\hat{\theta}) & 0 & -\omega_2^2 \cos(\hat{\theta}) & 0 & -\omega_3^2 \cos(\hat{\theta}) & 0 & -\omega_4^2 \cos(\hat{\theta}) & 0 \\ -\omega_1^3/g & 0 & -\omega_2^3/g & 0 & -\omega_3^3/g & 0 & -\omega_4^3/g & 0 \end{bmatrix} \tag{7.14}$$

Additional states for estimating angles from angular rates are not needed in the filter, as they can be calculated using equations developed in Chapter 5.3. The angle estimate $\hat{\theta}$ is calculated using the current height derivative estimate, as shown in Eq. 7.15. Furthermore, the state for mean wave heading, ϕ, is excluded as the waves generated in the tank are planar regular waves encountered from a known direction. The final height estimate is calculated using Eq. 7.16.

$$\hat{\theta} = \sum_i \text{atan}\left(\frac{\omega_i \hat{\dot{h}}_i}{g}\right) \tag{7.15}$$

$$\hat{h} = [1, 0, 1, 0, 1, 0, 1, 0]\boldsymbol{x}. \tag{7.16}$$

7.3 Experiment Design Summary

Fig. 7.5 shows the final set-up for the wave tank experiment. The platform is suspended from a hinged bar fixed to the sides of the tank, measuring height from a constant reference. In the following chapter, the results obtained from the testing methods outlined are presented.

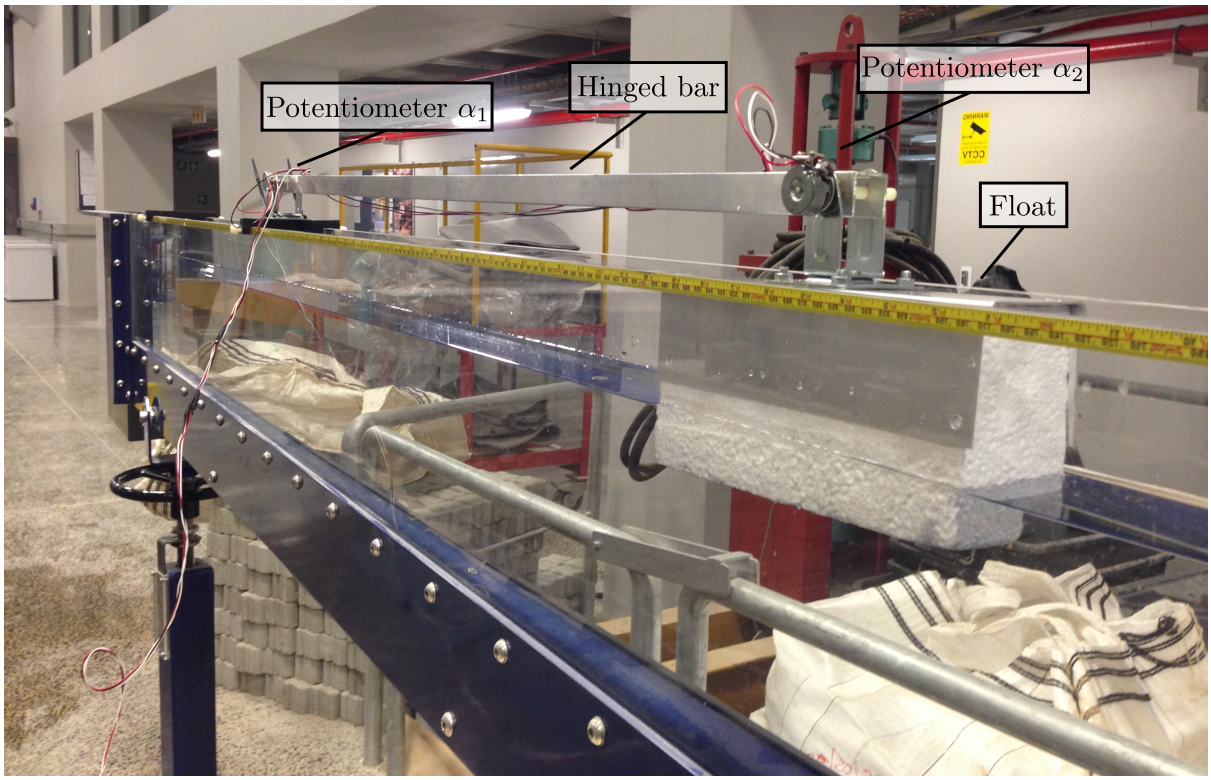

Figure 7.5: Platform taking measurements in the wave tank. Hinged bar is fixed to the sides of the tank, accurately measuring from a constant height reference.

Chapter 8

Results & Discussion

In this chapter, the results of simulations and experiments conducted are presented, with an accompanying discussion. Firstly, verification of the developed WG model is provided by way of impulse and step response simulations. Following this, a series of ocean wave generator simulations are provided to show how the platform responds to simulated wave action. These WG response simulations are passed to the estimator, which provides estimates of the original sea state input. Finally, evaluation of the estimator is shown using real world data obtained in a small scale experiment.

8.1 Wave Glider Dynamic Model

For the 2D model developed, the NED reference frame notation is adhered to, meaning a positive value for a z displacement corresponds to the WG moving downwards, while an x displacement is horizontal with respect to the sea surface.

8.1.1 Wave Glider Sea State Simulation

The WG model is subjected to a series of inputs to verify its performance. A sampling time of 1×10^{-3} s is used for the WG simulations. Firstly, the platform is initiated with no input forces in varying orientations. The velocity and position can be set directly in the model as initial conditions. This is useful for validation of the buoyancy force interaction. For instance, starting the simulation with the platform above the mean sea level results in falling for a short period, oscillating as it contacts the surface, and settling at a point where the buoyancy force generated by water displacement equals the weight of the vessel.

Fig. 8.1 shows the response of the platform when it is dropped from 0.1 m above the water surface. The platform initially oscillates due to the buoyancy force interacting with the weight. It reaches a settling point of 0.06 m, measured from the platform's centre of mass. This depth makes the submerged volume required to generate a buoyancy force equal to the platform weight.

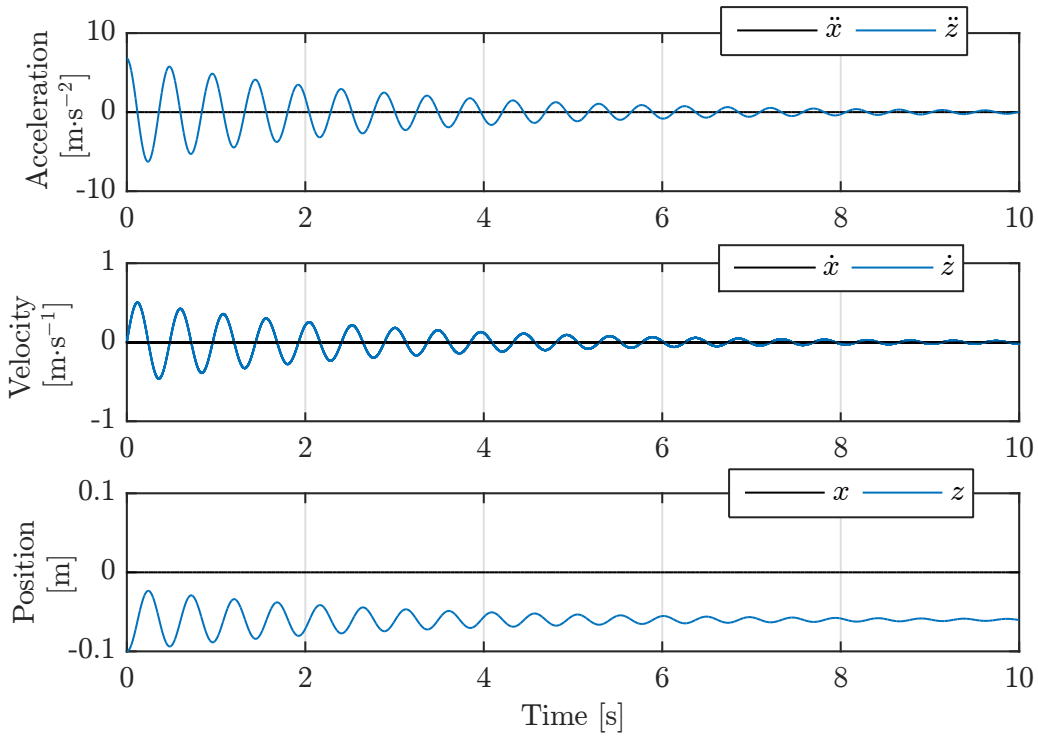

Figure 8.1: WG float dropped from 0.1 m above the mean ocean surface, resulting in some initial oscillations due to the buoyancy and gravity interaction. The platform's centre of gravity finally settles at 0.06 m, the depth required for buoyancy to counteract the platform's weight.

Following this, external forces and torques are applied as impulses and steps to the WG. Fig. 8.2 summarises the simulations conducted. At 1 s into the simulation, an impulse of 25 kN in the positive x coordinate is exerted on the WG as an initial test. The position settles at 2.5 m after 5 s.

Through field experiments conducted, the WG platform has been found to experience an average thrust force of 80 N [63]. This force is used in the step test as a more realistic simulation of forces experienced by the WG. At 10 s into the simulation, an 80 N step is exerted in the positive x coordinate, resulting in a step response in the velocity, and a subsequent ramp response in position. After 5 s, $\dot{x}$ settles at $0.8\,\mathrm{m}\cdot\mathrm{s}^{-1}$, while the position is a ramp.

The ocean wave generator takes in wind speed, $U_{19.5}$, and direction of arrival, θ, as inputs and produces deep sea waves. Fig. 8.3 shows the WG response to a sea state generated using a wind speed, $U = 10\,\mathrm{m}\cdot\mathrm{s}^{-1}$, at a mean direction of 0 rad. Due to the buoyancy-weight interaction, the CG of the WG finds equilibrium at 0.066 m below the ocean surface, visible as the slight height discrepancy in Fig. 8.3. Further simulations were carried out and the results of these are detailed in Appendix B.1.

8.1.2 Wave Glider Modelling

The initial WG model is designed using the Denavit-Hartenberg coordinate referencing system. Coupling in the different DOFs can be seen in the results, which is to be expected. An impulse in the x coordinate results in motion in that axis, as well as a response in the z coordinate.

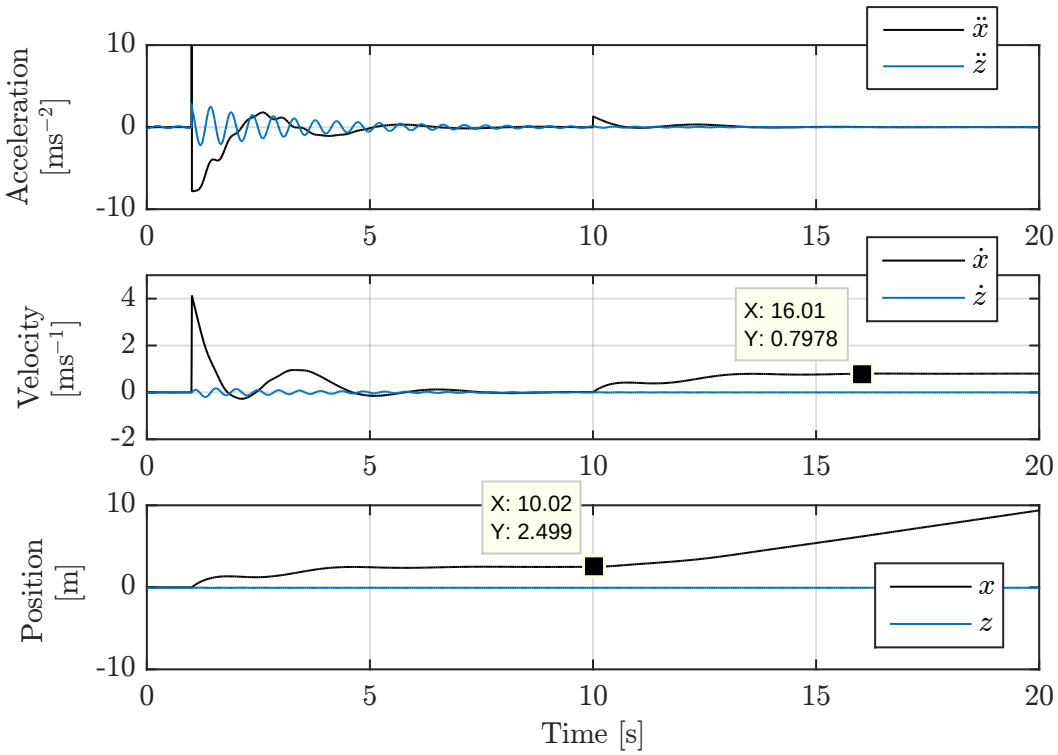

Figure 8.2: WG response to impulse and step input; (top) acceleration response, (middle) velocity response, (bottom) position response. At 1 s, impulse of 25 kN exerted on platform, settling after 5 s. At 10 s, 80 N step exerted in the x coordinate, resulting in a ramp response in x position, while the x velocity settles at $0.8\,\mathrm{m}\cdot\mathrm{s}^{-1}$.

The WG platform effectively acts as a filter, when comparing the inertial measurements to the true sea state. High frequency fluctuations such as capillary waves are not present in the WG response. This is evident when the WG is subjected to a fast changing sea state. As high frequency waves are not useful, this filtering behaviour is beneficial for the wave estimation goal.

8.2 Spectral Estimation

The simulation parameters used in the wave height estimation are summarised in Table 8.1. These include settings for the wind wave generator and configuration parameters of the peak frequency estimator and the Kalman filter. A sampling time of $T = 0.1\,\mathrm{s}$ is used for the estimator. The frequency points used are logarithmically spaced as logspace(0, 0.6, 6), resulting in

$$\omega = \begin{bmatrix} 1.0000 & 1.3183 & 1.7378 & 2.2909 & 3.0200 & 3.9811 \end{bmatrix} \mathrm{rad}\cdot\mathrm{s}^{-1}. \tag{8.1}$$

Since the spread of these components is not linear, the width of each component must be representative of the spacing. Fig. 8.4 shows how the spacing is calculated. Eq. 8.3 shows the width of each component, calculated using the geometric mean between successive components, Eq. 8.2.

$$\Delta\omega_i = \sqrt[2]{\omega_i \cdot \omega_{i+1}} - \sqrt[2]{\omega_i \cdot \omega_{i-1}} \tag{8.2}$$

$$\Delta\omega = \begin{bmatrix} 1.1482 & 0.3654 & 0.4817 & 0.6350 & 0.8371 & 0.9857 \end{bmatrix} \tag{8.3}$$

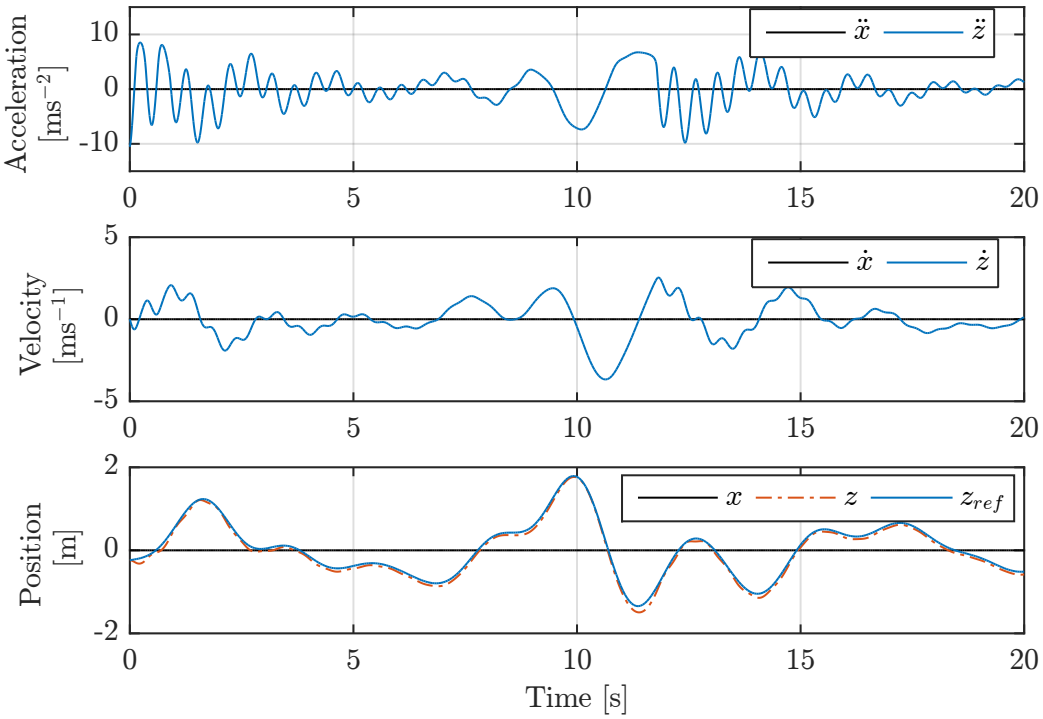

Figure 8.3: The WG response to ocean waves; generator initiated with $U = 10\ \mathrm{m \cdot s^{-1}}$.

The mean wave direction can be set in the generator from 0 rad to 2π rad. In addition, the wind speed can be set in the range of $1\,\mathrm{m \cdot s^{-1}}$ to $20\,\mathrm{m \cdot s^{-1}}$. Simulations with parameters in this range are presented. The results of further simulations conducted are listed in Appendix B.2.

8.2.1 Peak Frequency Estimation

The wave generator developed can dynamically change spectral shape in response to wind changes and this allowed the peak frequency estimator to be tested. The peak frequency estimation uses the height estimates from the Kalman filter to obtain an estimate of ω_p. This

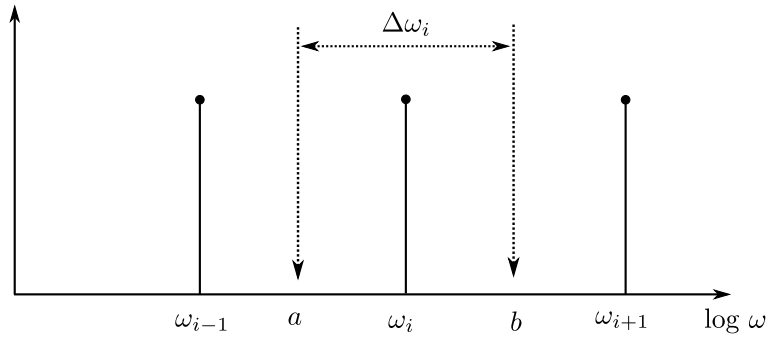

Figure 8.4: Calculation of the frequency component width, $\Delta\omega$, using the geometric mean.

Table 8.1: Simulation parameters for the wave generator, peak frequency estimator, and Kalman filter.

Parameter	Value	Unit
T	1×10^{-1}	s
θ	$0 - 2\pi$	rad
$U_{19.5}$	$1 - 20$	$\mathrm{m \cdot s^{-1}}$
ω	$\omega_p \cdot \mathrm{logspace}(0, 0.6, 6)$	$\mathrm{rad \cdot s^{-1}}$
ω_c	6×10^{-1}	$\mathrm{rad \cdot s^{-1}}$

feedback loop works provided that the peak estimator dynamics are much slower than the Kalman filter dynamics. The loop filter designed for this purpose achieves this goal. Estimation of a pure sinusoidal sea state is shown in Fig. 8.5. Locking onto the desired signal is achieved within 6 s, thereby providing an estimate of the frequency, $\hat{\omega}_p$.

Fig. 8.6 shows step changes in the wind speed, and the corresponding shift in the peak frequency, ω_p of the wind wave spectrum. At 1×10^4 s, a step from $12\,\mathrm{m \cdot s^{-1}}$ to $9\,\mathrm{m \cdot s^{-1}}$ results in ω_p changing from $0.7\,\mathrm{rad \cdot s^{-1}}$ to $0.95\,\mathrm{rad \cdot s^{-1}}$, and the estimate $\hat{\omega}_p$ following this change. When $U_{19.5}$ changes from $9\,\mathrm{m \cdot s^{-1}}$ to $13\,\mathrm{m \cdot s^{-1}}$ at 2×10^4 s, ω_p changes from $0.95\,\mathrm{rad \cdot s^{-1}}$ to $0.65\,\mathrm{rad \cdot s^{-1}}$, closely followed by $\hat{\omega}_p$.

8.2.2 Wave Height Estimation

The Kalman filter is initialised as stated in Chapter 5, with six frequency components scaled by the peak frequency. The initial $\hat{\omega}_p$ is the quiescent frequency of the VCO, ω_c. Due to the coupling of the h_i and $\dot{h}_i$ states, discussed in Chapter 5.4.1, it was stated that process noise could enter the system through either state. Simulations conducted on both scenarios show better performance when noise enters through h_i, as $\sigma^2_{h_i}$. Hence the preferred configuration is setting $\sigma^2_{\dot{h}_i} = 0$.

Wave Height Prediction

Fig. 8.7 shows the wave elevation, $h(t)$, at a fixed point in space against the estimated equivalent, $\hat{h}(t)$. The performance metric used in evaluating the estimator's performance is the error covariance of $\hat{h}(t)$, P_{hh}. It is calculated as shown in Eq. 8.5, and represents the uncertainties in the estimate.

$$C_h = \begin{bmatrix} 1 & 0 & 1 & 0 & 1 & 0 & 1 & 0 & 1 & 0 & 1 & 0 & 0 & 0 \end{bmatrix}, \tag{8.4}$$

$$P_{hh} = C_h P_k C_h^T, \tag{8.5}$$

where C_h is a measurement matrix extracting only the height contributions from the current error covariance, P_k, and leaving behind the velocity, angle, and bias covariances. Fig. 8.8 compares the vertical height signal from the wave generator, $h(t)$, to the estimated height with a standard deviation on either side, $\hat{h}(t) \pm \sigma_{\hat{h}}$.

Verifying the estimator's prediction capabilities requires projection of the height estimate τ s ahead, as $\hat{h}(t - \tau)$. For simulations carried out at varying wind-speeds and projection times, the deviation $\sigma_h = \sqrt{P_{hh}(t|_{t-\tau})}$ is shown in Table 8.2. Fig. 8.9 shows the height estimate at a

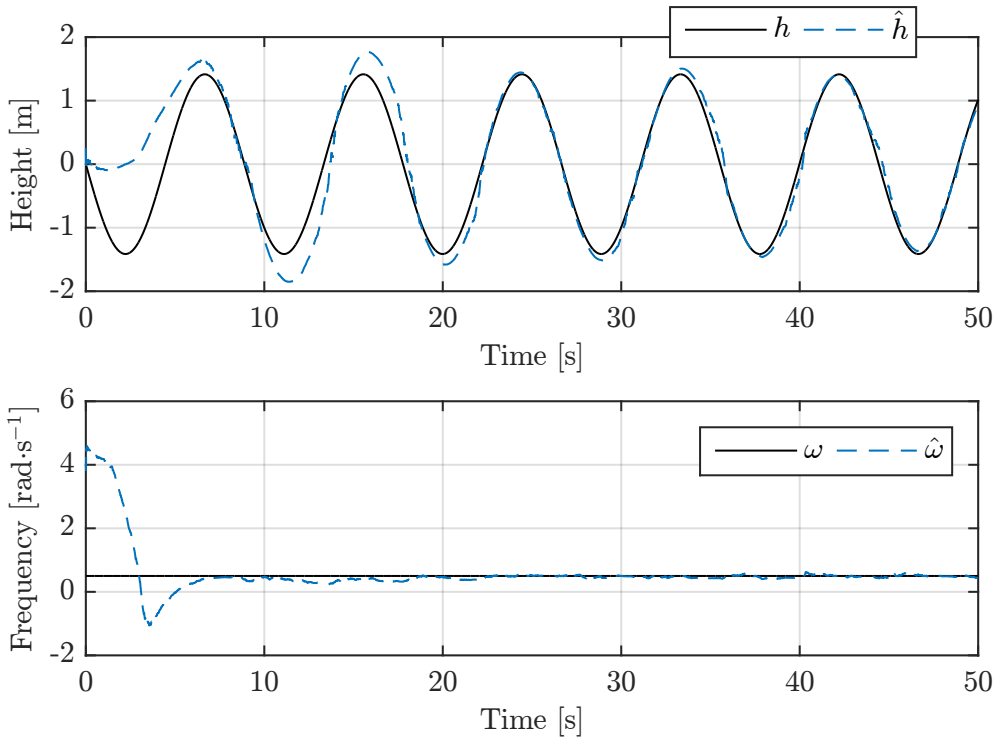

Figure 8.5: Estimation of a single sinusoid; (top) height estimate locks onto the desired height within 6 s; (bottom) estimator tracks a constant frequency of $0.5\,\mathrm{rad}\cdot\mathrm{s}^{-1}$.

projection time of $\tau = 10$ s and wind speed of $10\,\mathrm{m}\cdot\mathrm{s}^{-1}$. Again, the error covariance, $P_{hh}(t|_{t-\tau})$, of $\hat{h}(t|_{t-\tau})$ is used as the performance metric. For the one wave ahead wave estimate, when τ is less than 10 s, the height is estimated well with a mean square error of 0.49 m (for a wind speed of $10\,\mathrm{m}\cdot\mathrm{s}^{-1}$). This accuracy quickly declines as τ increases beyond 20 s. For a wind speed of $10\,\mathrm{m}\cdot\mathrm{s}^{-1}$, the mean square error of the height is 0.67 m. Although an increase in uncertainty can be seen as the projection time is increased, the divergence is small enough to allow for reasonable prediction at $\tau = 20$ s at wind speeds below $10\,\mathrm{m}\cdot\mathrm{s}^{-1}$. With wind speeds above $10\,\mathrm{m}\cdot\mathrm{s}^{-1}$, the error becomes significant, showing the upper limit of the prediction capability.

Table 8.2: steady-state wave height error, $\sqrt{P_{hh}(t|_{t-\tau})}$, for future projections, τ, at varying wind speeds, $U_{19.5}$.

$\sqrt{P_{hh}(t\|_{t-\tau})}$ [m]				
$U_{19.5}$ m · s^{-1}	8 m · s^{-1}	10 m · s^{-1}	12 m · s^{-1}	14 m · s^{-1}
τ s				
0 s	0.09	0.26	0.34	0.34
5 s	0.19	0.47	0.61	0.59
10 s	0.25	0.49	0.64	0.62
15 s	0.26	0.52	0.66	0.63
20 s	0.31	0.67	0.77	0.74

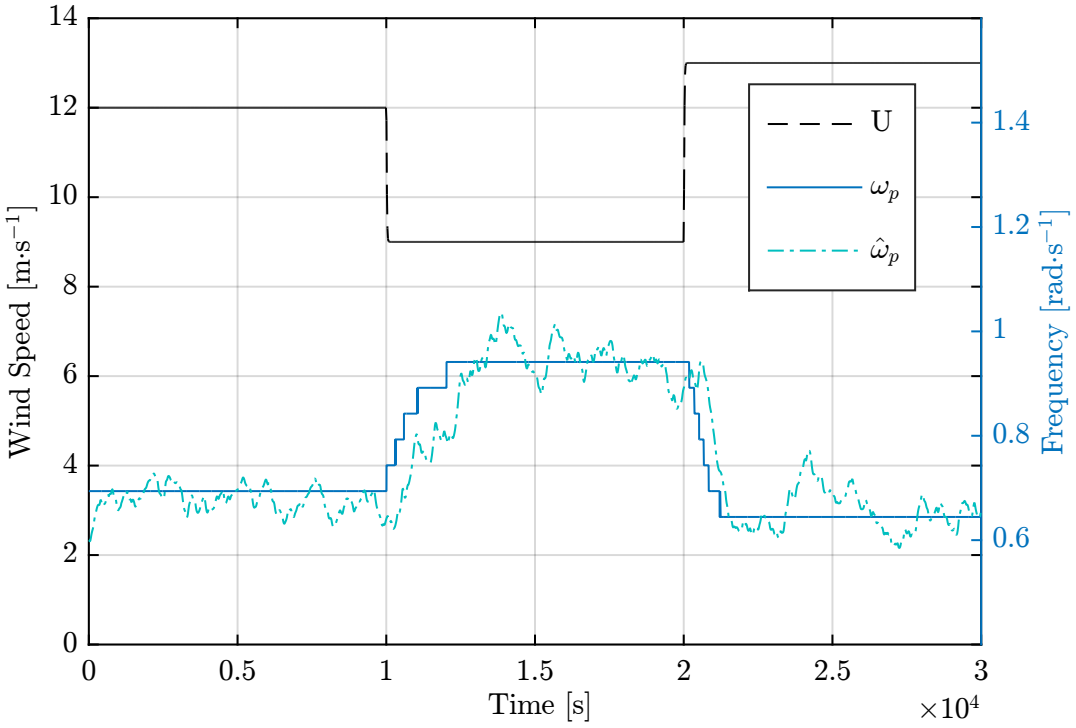

Figure 8.6: Response of peak frequency to changes in wind speed. Step changes in wind shown by the black dashed line (left axis); peak frequency, ω_p shifts due to changing winds, while PLL tracks this change slowly over time (right axis).

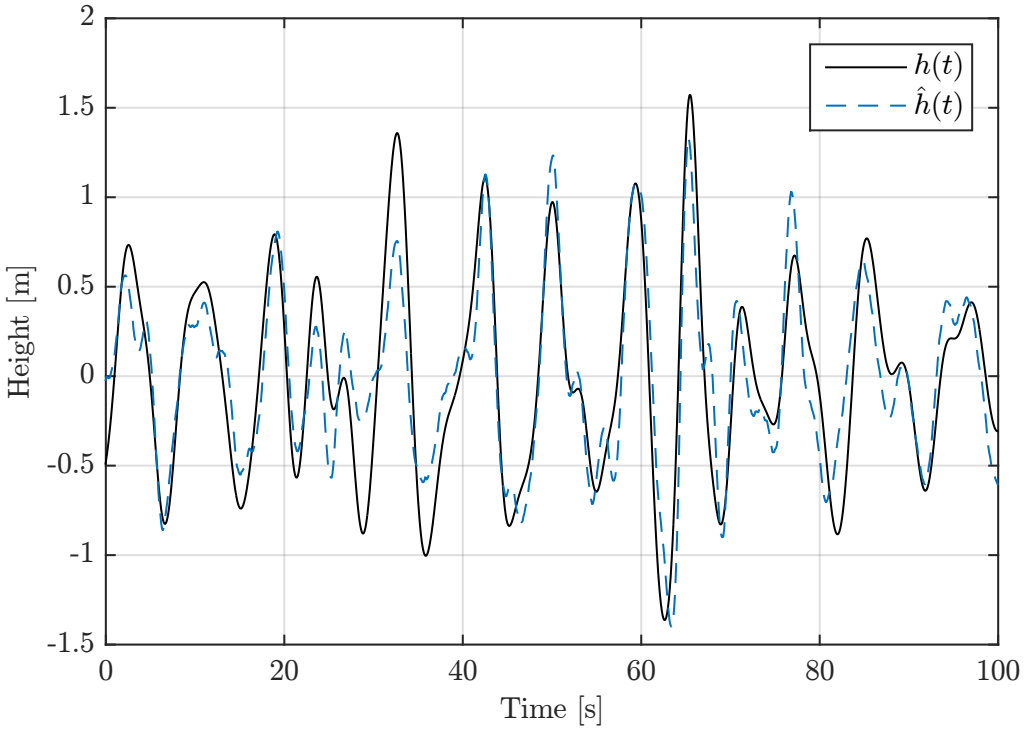

Figure 8.7: The generated wave heights, $h(t)$ at steady-state, compared to a current estimate from the Kalman filter, $\hat{h}(t)$.

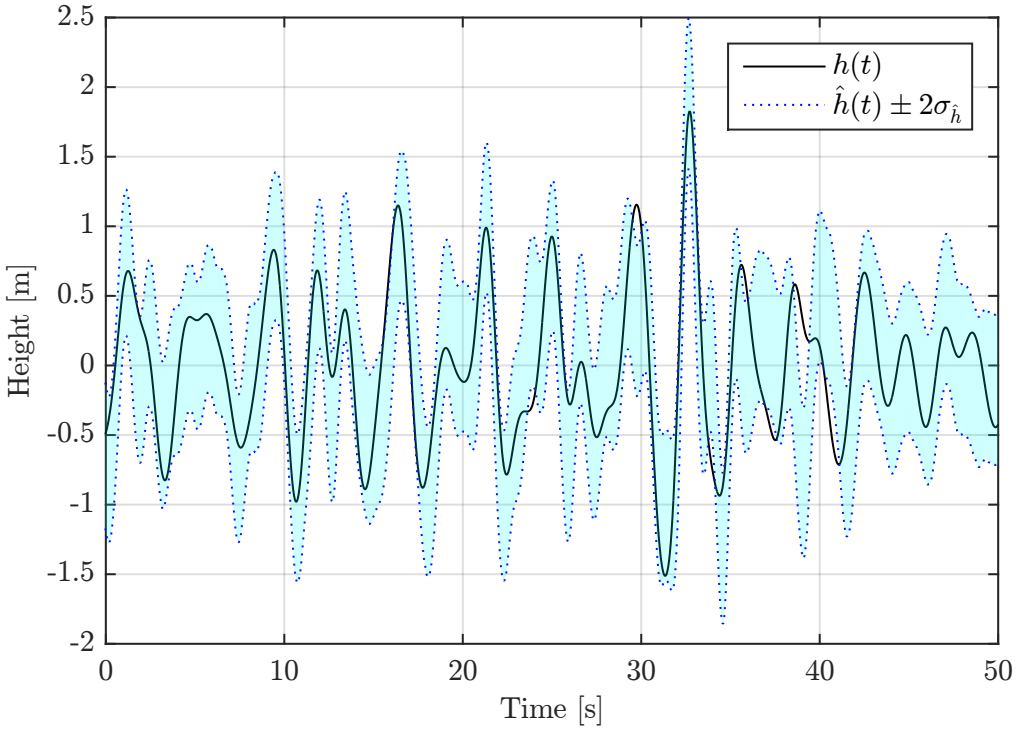

Figure 8.8: The wave generator height, $h(t)$ at steady-state, plotted against the standard deviation of the estimated height signal, $\hat{h}(t)$.

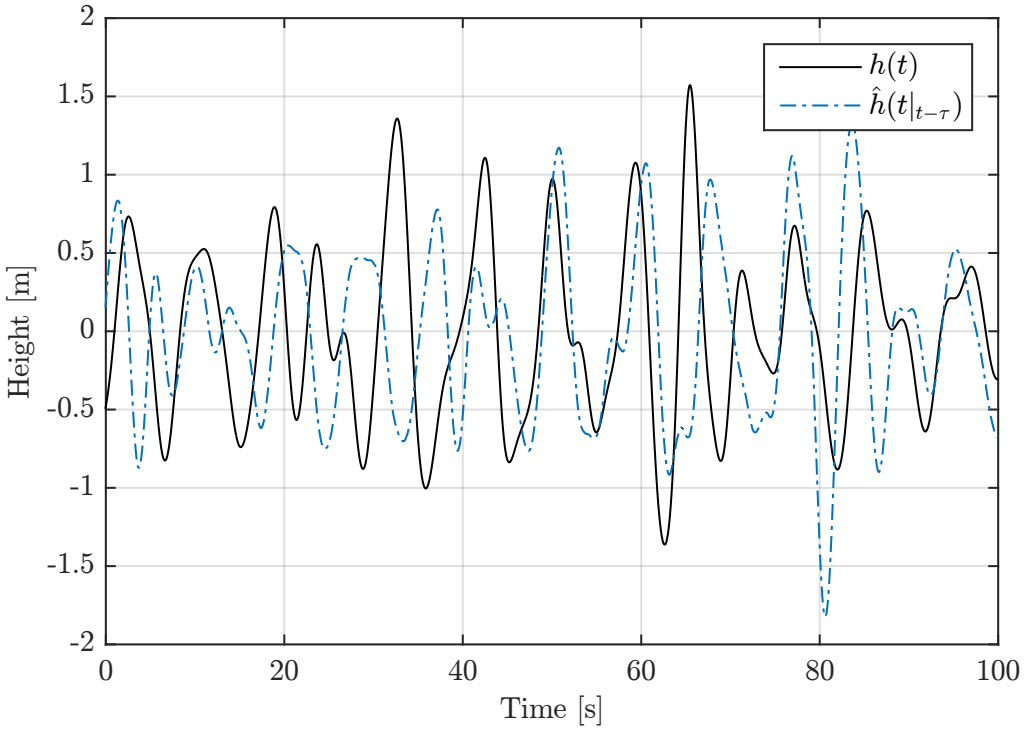

Figure 8.9: Generated wave heights, $h(t)$ at steady-state, compared to an estimate of the state made $\tau = 10$ s prior, $\hat{h}(t|_{t-\tau})$, to show prediction capabilities of the scheme.

Power Spectral Densities of Vertical Acceleration and Wave Height

Validation of the wave tracking capabilities requires taking a power spectral density (PSD) to compare the distribution of energy over the frequency range for the acceleration and wave height signals. The sampling window, $N = 1024$, for both PSDs in Figs. 8.10 and 8.11 is selected such that the lowest frequency estimated can be captured. It is calculated using the lowest frequency expected for wind waves, $f_{min} = 0.1$ Hz, as

$$T_w = \frac{1}{f_{min}}, \tag{8.6}$$

$$N = 2^{\text{npow}\left(\frac{nT_w}{T}\right)}, \tag{8.7}$$

where T_w is the sampling window required, T the sampling period, and n the total number of wavelengths to be captured. For computational efficiency, a power of two number is used, hence the next power of two function, npow(x), is used. It finds the next power of two above the value x, as npow$(x) =$ ceil$(\log_2(x))$, where ceil rounds up to the nearest integer.

Fig. 8.10 is a PSD of the acceleration estimate and the simulated acceleration PSD from the wave generator. Most of the energy at lower frequencies is captured by the filter, which translates to the majority of the energy being captured in the wave height spectrum, shown in Fig. 8.11, where a PSD of $h(t)$, $\hat{h}(t)$ and $\hat{h}(t-\tau)$ is taken. It illustrates good coverage of the entire frequency range surrounding the peak frequency.

Frequency Spacing and Component Selection

The selection and spacing of frequency components is of particular importance. The results of selecting a small number of frequency components to represent the sea wave spectrum are evident in Fig. 8.10, the acceleration PSD. An emphasis placed on estimating the lower frequencies where the bulk energy resides, results in the higher frequencies in the spectrum not being captured. However, in the height variance spectrum shown in Fig. 8.11, there is better coverage. The effects of neglecting the higher frequencies show up only as slight discrepancies when looking at the wave height estimation.

An example of incorrect frequency selection is shown in Fig. 8.12. In this experiment, conducted under the same conditions as in Fig. 8.7, the peak frequency is estimated correctly. However, the components surrounding the peak are not dispersed enough to capture the higher frequency components. This results in the estimator tracking the peak frequency component well, but poorly tracking the remainder of the spectrum.

Fortunately, the shape of the wind wave spectrum is the same for all wind speeds. This can be verified by normalising wave spectra for different wind speeds. Hence the best distribution of components was found when there was adequate coverage of the normalised wind wave spectrum, using Akaike's Information Criterion described in Chapter 5.2.3.

8.2.3 Angle of Arrival Estimation

The mean wave direction is also obtained from the filter. Fig. 8.13 shows the estimation of a constant mean wave direction of 0.25π rad with respect to the positive x coordinate. The filter is initiated with an angle of arrival estimate of 0 rad, and takes approximately 700 s to settle

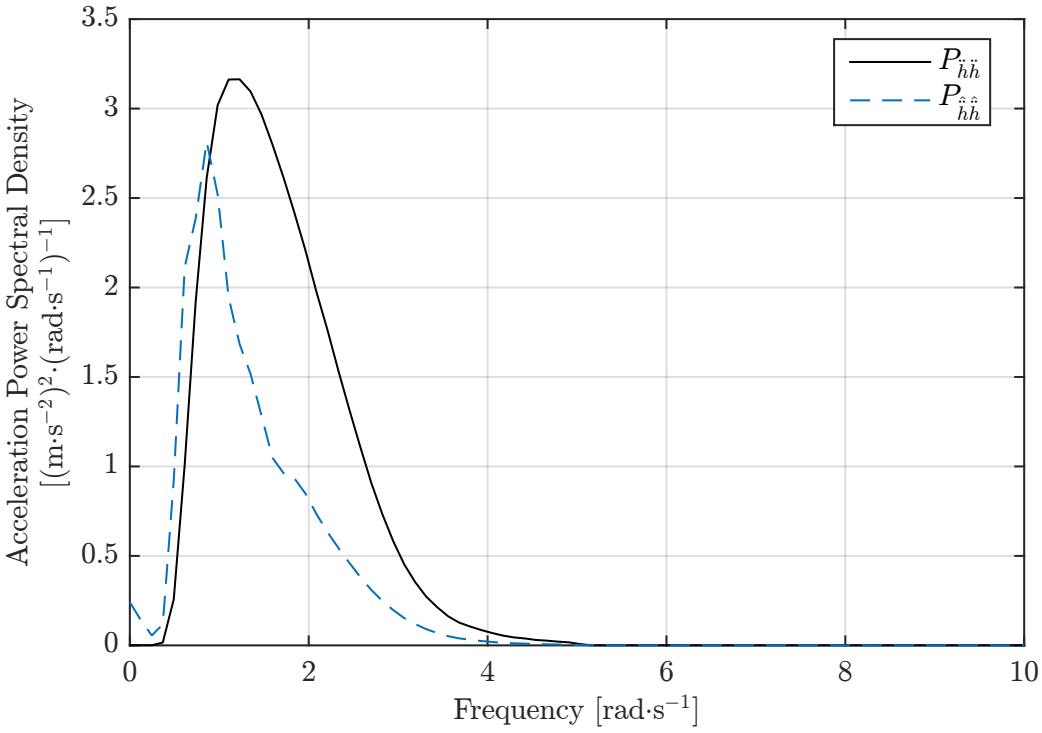

Figure 8.10: Power Spectral Densities of the sea state generator acceleration, $P_{\ddot{h}\ddot{h}}$, versus the estimated sea state acceleration, $P_{\hat{\ddot{h}}\hat{\ddot{h}}}$, with a difference in amplitude at higher frequencies caused by having few frequency components estimating at higher frequencies.

in response to the step change of 0.25π rad. This response time is acceptable, because wave direction is not expected to change rapidly over long periods of time. Further simulation results are provided in Appendix B.2.1.

8.3 Wave Tank Experiment Results

Fig. 8.14 shows the wave height estimates obtained from the wave tank experiment. The reference wave height obtained from the potentiometers is plotted against the wave estimate from the platform. A mean square error of 1.9134×10^{-4} m in the height estimate indicates that the height can be estimated with only acceleration and angular rate measurements. Fig. 8.15 shows a PSD taken of the wave height and the respective estimate, showing correct estimation of the peak frequency, as well as the surrounding components of the height variance spectrum.

Although the length of the wave tank was sufficient for the platform size used, a wave absorption zone section could not be practically implemented. This led to reflection of the generated waves, ultimately resulting in resonance. Furthermore, the experiment did not represent deep sea ocean waves. Furthermore, low excitation was observed with the small amplitude waves generated in the wave tank. In such an environment, implementing a gain scheduling technique would be useful when wave amplitude is low. Despite these limitations encountered with the wave tank experiment, the preliminary results obtained confirm the performance of the estimator, showing that the height can be estimated with only acceleration and angular rate measurements.

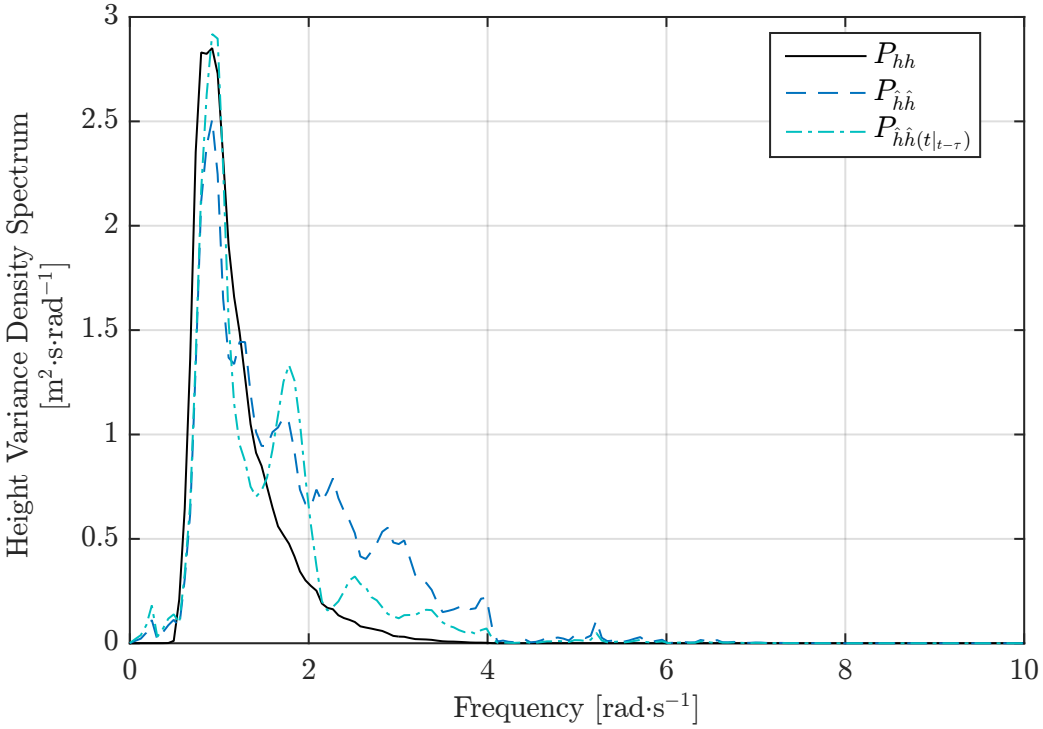

Figure 8.11: Power Spectral Densities of the true sea state height, P_{hh},estimated sea state height, $P_{\hat{h}\hat{h}}$, and the future predicted sea state height, $P_{\hat{h}\hat{h}(t|_{t-\tau})}$.

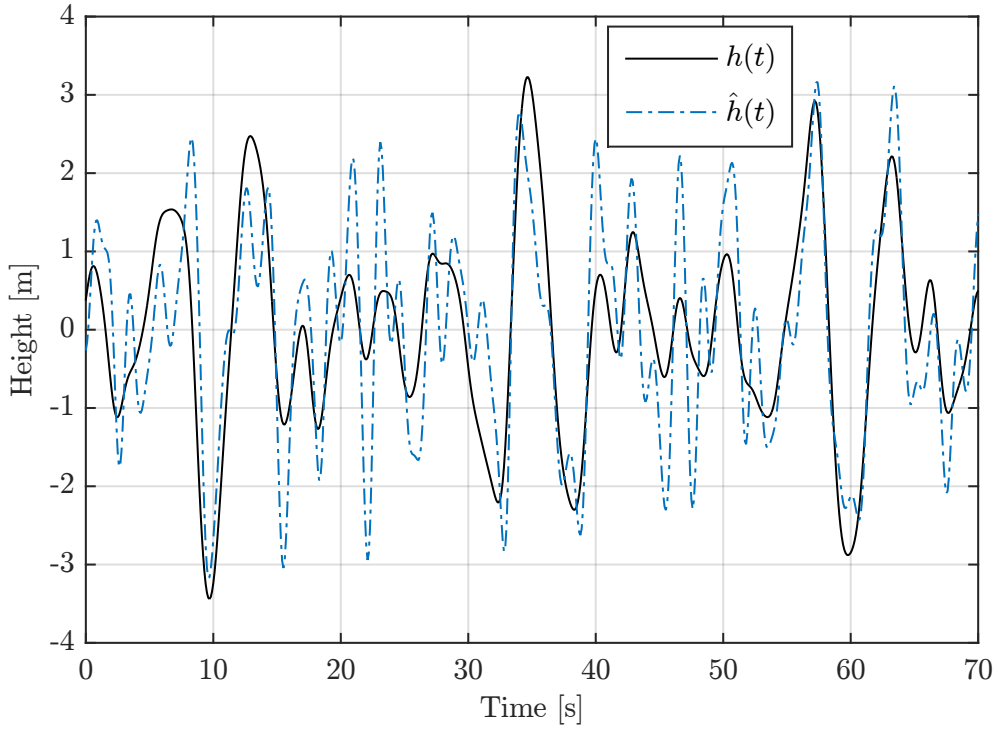

Figure 8.12: Frequency spacing and component selection example showing good tracking of the peak frequency. However, few components are present to track the higher frequencies, hence there is poor tracking where the signal is fast changing.

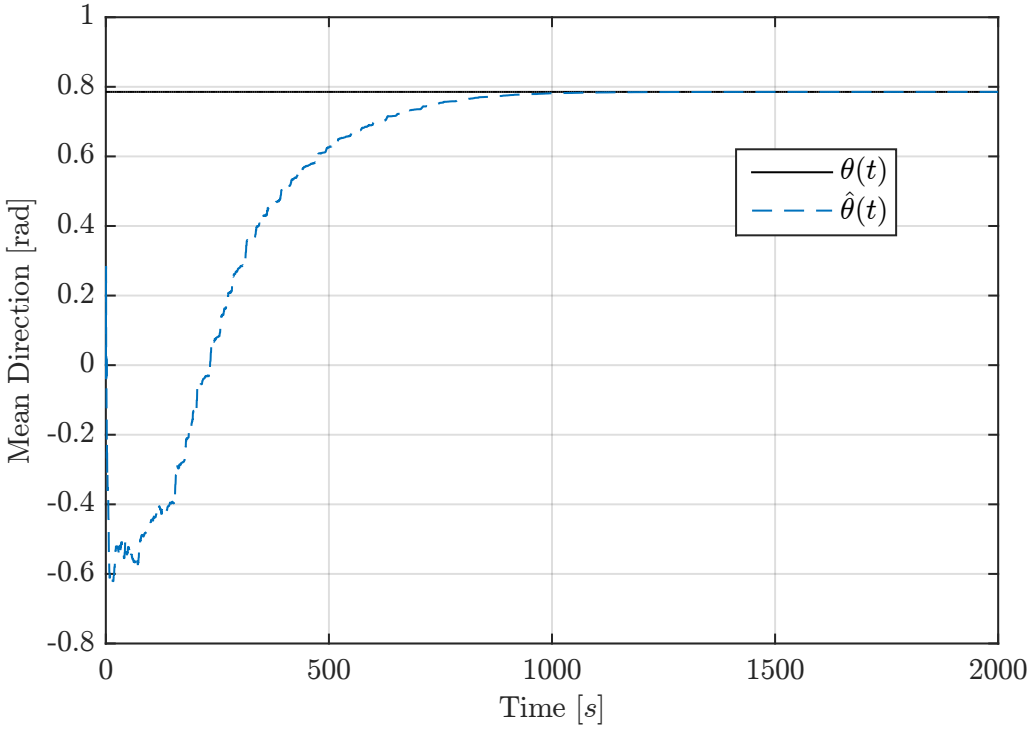

Figure 8.13: Kalman filter tracking the mean wave direction, set to a constant value of 0.25π rad from the positive x coordinate.

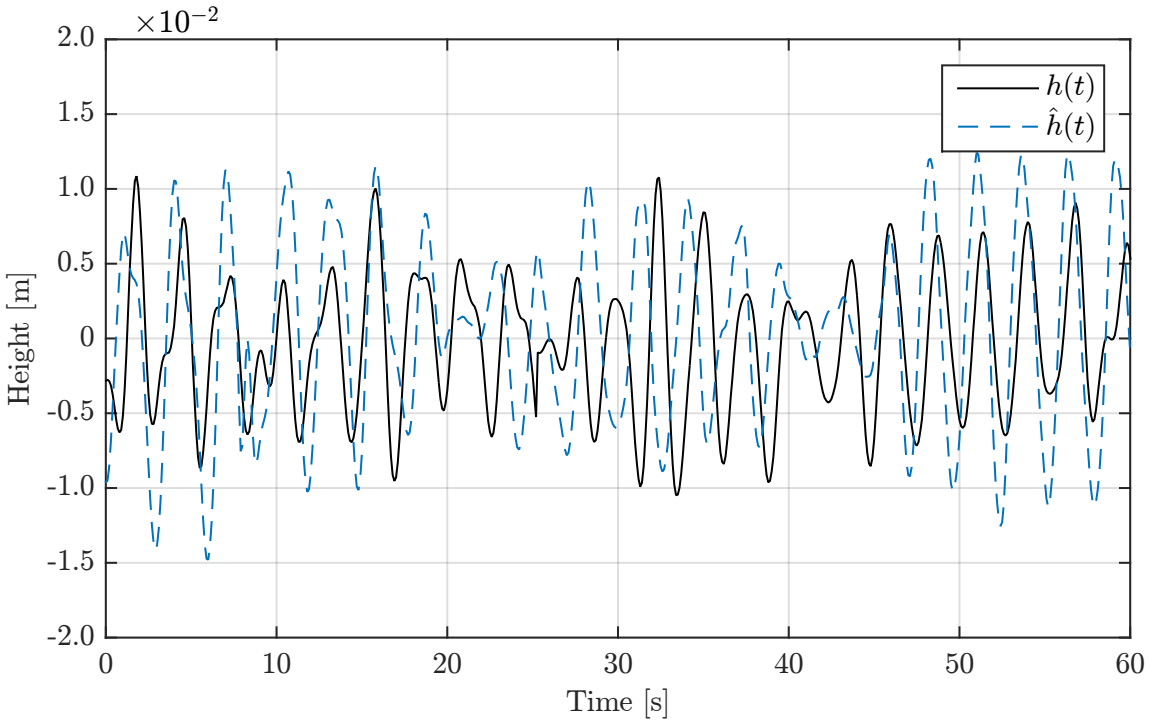

Figure 8.14: Wave height reference measured using potentiometers, $h(t)$, compared to a current estimate from the wave height estimator, $\hat{h}(t)$.

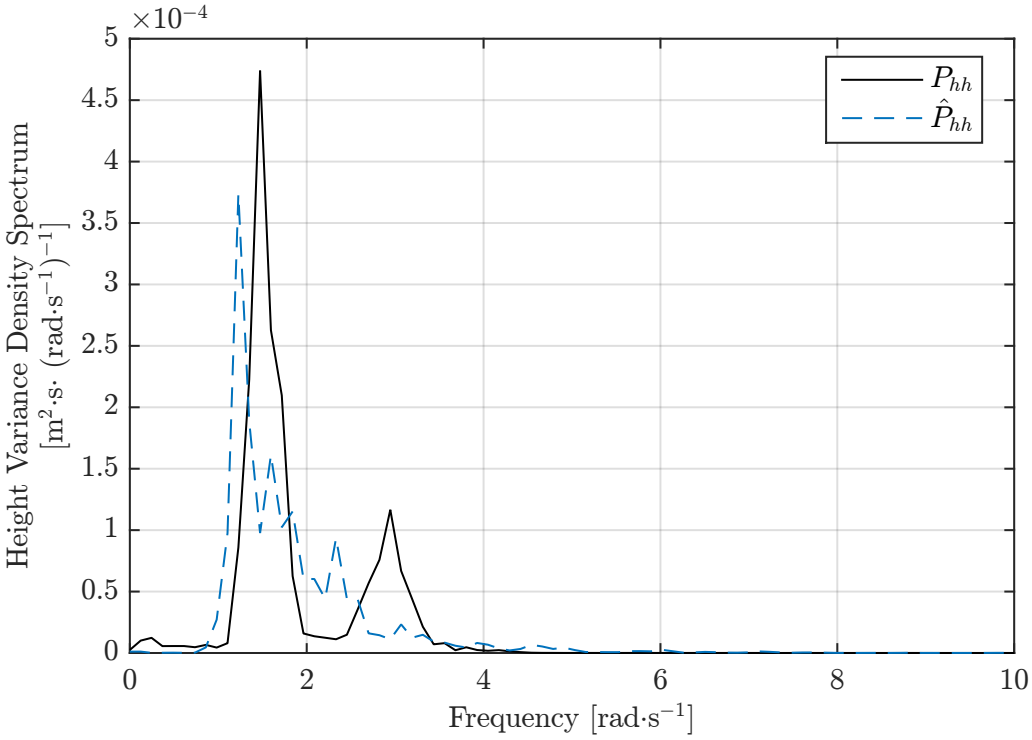

Figure 8.15: PSD of wave height reference measured using potentiometers, P_{hh}, compared to an estimate from the wave height estimator, $P_{\hat{h}\hat{h}}$.

This page has been intentionally left blank.

Chapter 9

Conclusion

The significance of this research in the greater wave glider project is to provide awareness of the local sea environment. Once this has been achieved, the navigation goal can take place. Ultimately, this brings the platform a step closer towards being fully autonomous, while also providing beneficial information about the local environment that was previously not possible. Conclusions based on the results obtained are presented in this chapter, before noting future work that must be conducted to extend the functionality achieved in this research.

9.1 Sea State Estimation from Inertial Platform Data

In Chapter 3, a 2D model of the WG was developed using Lagrangian dynamics. To validate this model and subsequent sea state estimation, a wind wave generator was developed. An important design criteria of the generator is the ability to change the wind speed and hence spectral shape during operation, which was achieved as detailed in Chapter 4.3.

A real-time sea state estimator was developed in Chapter 5 and 7, consisting of a Kalman filter and peak frequency estimator. This approach is of a relatively low order and shows promise as an alternative to Fourier transform methods for short term sea state estimation. The approach taken was to estimate individual components of the greater spectrum. Preliminary investigations were made into alternative methods, but this was decidedly the best method for the task at hand. However, for the sake of completeness, these other avenues can be explored to uncover any hidden benefits not immediately evident.

The results obtained in simulation demonstrate the ability to predict wave height a few cycles ahead. Moreover, preliminary results obtained in the wave tank experiment provide further validation, showing that the height can be estimated with only acceleration and angular rate measurements.

This research set out to provide sea state information for path planning and per-wave navigation of mobile marine platforms. Through the use of inertial measurements of a WG robotic platform, estimation of the local wave height and angle of arrival in real time has been achieved by a filter based sea state estimator. This is demonstrated by the development of the dynamic model, wind wave generator, and the spectral estimator.

9.2 Future Work

Future work for the project involves integration of mobile platform models, namely a detailed dynamic model of the WG platform [43]. In addition, this approach will be extended to consider a moving platform, 3D, and multi-modal waves.

In this work, only acceleration and angular rate measurements were used to obtain height estimates. A possible improvement in performance can be gained by including the GPS sensor to provide height measurements.

Lastly, an investigation into alternative spectral estimation techniques, such as the noise whitening technique outlined in Appendix A, can be carried out. This method was not pursued as it restricted the estimation to the spectral shape of whichever wave model used. The limitation of this is the dependence on accuracy of representation by the wave model used. Provided that the model used is a good approximation of the true ocean wave spectrum, this method becomes a viable option.

9.3 Recommendations

On the basis of the foregoing conclusions, the following recommendations for proceeding with the research are made:

- Integrate a detailed dynamic model of the WG platform. This will allow the response of the platform to wave action to be identified and accounted for.
- Extend the work to 3D, and consider the platform as moving through the wave field.
- Investigate the effects of multi-modal waves on performance of the estimator.
- Incorporate GPS and barometric pressure measurements into the estimator.

This page has been intentionally left blank.

Bibliography

[1] C. R. German, M. V. Jakuba, J. C. Kinsey, J. Partan, S. Suman, A. Belani, and D. R. Yoerger, "A long term vision for long-range ship-free deep ocean operations: Persistent presence through coordination of autonomous surface vehicles and autonomous underwater vehicles," *2012 IEEE/OES Autonomous Underwater Vehicles (AUV)*, 2012.

[2] S. Frolov, J. Bellingham, W. Anderson, and G. Hine, "Wave Glider - a platform for persistent monitoring of algal blooms," *Oceans 2011*, pp. 1–5, 2011.

[3] T. Daniel, J. Manley, and N. Trenaman, "The Wave Glider: Enabling a new approach to persistent ocean observation and research," *Ocean Dynamics*, vol. 61, no. 10, pp. 1509–1520, 2011.

[4] R. Hine and P. McGillivary, "Wave powered autonomous surface vessels as components of ocean observing systems," *Proc. of PACON*, pp. 1–9, 2007.

[5] T. A. Villareal and C. Wilson, "A comparison of the Pac-X Trans-pacific Wave Glider data and satellite data (MODIS, Aquarius, TRMM and VIIRS)," *PLoS ONE*, vol. 9, no. 3, 2014.

[6] J. E. Manley, "Unmanned surface vehicles, 15 years of development," *Oceans 2008*, pp. 1–4, 2008.

[7] L. Lenain and W. Kendall Melville, "Autonomous surface vehicle measurements of the ocean's response to Tropical Cyclone Freda," *Journal of Atmospheric and Oceanic Technology*, vol. 31, pp. 2169–2191, 2014.

[8] Liquid Robotics, "Liquid Robotics products Wave Glider SV3." `https://www.liquid-robotics.com/platform/how-it-works/`, 2013.

[9] N. Kraus and B. Bingham, "Estimation of Wave Glider dynamics for precise positioning," *Oceans 2011*, pp. 1–9, 2011.

[10] A. Alvarez, "Assessment of sea wave spectra using a surfaced glider," *Deep-Sea Research Part I: Oceanographic Research Papers*, vol. 102, pp. 135–143, 2015.

[11] Datawell, "Datawell Waverider reference manual," tech. rep., Datawell BV, Heerhugowaard, 2009.

[12] Datawell, "Datawell Waverider reference manual," tech. rep., Datawell BV, Heerhugowaard, 2012.

[13] U. D. Nielsen and D. C. Stredulinsky, "Sea state estimation from an advancing ship - a comparative study using sea trial data," *Applied Ocean Research*, vol. 34, pp. 33–44, 2012.

[14] R. Pascoal and C. G. Soares, "Non-parametric wave spectral estimation using vessel motions," *Applied Ocean Research*, vol. 30, pp. 46–53, 2008.

[15] R. Pascoal and C. G. Soares, "Kalman filtering of vessel motions for ocean wave directional spectrum estimation," *Ocean Engineering*, vol. 36, pp. 477–488, 2009.

[16] U. D. Nielsen, "A concise account of techniques available for shipboard sea state estimation," *Ocean Engineering*, vol. 129, pp. 352–362, 2017.

[17] A. Caiti, V. Calabró, S. Grammatico, A. Munafó, and M. Stifani, "Lagrangian modelling of an underwater wave glider," *Oceans 2011*, pp. 6–9, 2011.

[18] P. Ngo, J. Das, J. Ogle, J. Thomas, W. Anderson, and R. N. Smith, "Predicting the speed of a Wave Glider autonomous surface vehicle from wave model data," *2014 IEEE/RSJ International Conference on Intelligent Robots and Systems*, pp. 2250–2256, 2014.

[19] U. D. Nielsen, *Estimation of Directional Wave Spectra from Measured Ship Responses*. PhD thesis, Technical University of Denmark, Lyngby, Denmark, 5 2005.

[20] T. I. Fossen, *Marine Control Systems: Guidance, Navigation, and Control of Ships, Rigs and Underwater Vehicles*. Trondheim: Marine Cybernetics, 2002.

[21] T. I. Fossen, *Handbook of Marine Craft Hydrodynamics and Motion Control*. Trondheim: John Wiley & Sons, 1st ed., 2011.

[22] J. Falnes, *Ocean Waves and Oscillating Systems: Linear Interactions Including Wave-Energy Extraction*. Cambridge University Press, 2002.

[23] D. Hauser and H. E. Krogstad, *Measuring and Analysing the Directional Spectrum of Ocean Waves*. De Bilt: Koninklijk Nederlands Meterologisch Instituut, 2005.

[24] L. Holthuijsen, *Waves in Oceanic and Coastal Waters*. Delft: Cambridge University Press, 2007.

[25] L. Linnett, S. Clarke, B. Calder, and Y. Rzhanov, "The generation of a time correlated 2D random process for ocean wave motion," *6th International Conference on Image Processing and it's Applications*, vol. 2, no. 443, pp. 623–626, 1997.

[26] O. M. Phillips, *Dynamics of the Upper Ocean*. London: Cambridge University Press, 2nd ed., 1966.

[27] E. C. Bowers, "Short Crested Seas in Harbour Modelling," tech. rep., Maritime Engineering Department of Hydraulics Research, 11 1987.

[28] R. G. Brown and P. Y. C. Hwang, *Introduction to Random Signals and Applied Kalman Filtering*. John Wiley & Sons, 1997.

[29] W. J. Pierson and L. Moskowitz, "A proposed spectral form for fully developed wind seas based on the similarity theory of S. A. Kotaigorodskii," tech. rep., U.S. Naval Oceanographic Office, 10 1963.

[30] S. Massel, *Ocean Surface Waves: Their Physics and Prediction*. Advanced Series on Ocean Engineering, World Scientific Publishing Company, 2013.

[31] J. Tessendorf, "Simulating ocean water," *Association for Computing Machinery SIGGRAPH*, vol. 1, no. 2, p. 5, 2001.

[32] G. A. Mastin, P. A. Watterberg, and J. F. Mareda, "Fourier synthesis of ocean scenes," *IEEE Computer Graphics and Applications*, vol. 7, 1987.

[33] G. Hitz, F. Pomerleau, F. Colas, and R. Siegwart, "Relaxing the planar assumption: 3D state estimation for an autonomous surface vessel," *The International Journal of Robotics Research*, 2015.

[34] E. Eitelberg, *Optimal Estimation for Engineers.* NOYB Press, 1991.

[35] P. Horowitz and W. Hill, *The Art of Electronics.* Cambridge: Cambridge University Press, 2nd ed., 2008.

[36] P. Zarchan and H. Musoff, *Fundamentals of Kalman Filtering: A Practical Approach.* American Institute of Aeronautics and Astronautics, Incorporated, 2000.

[37] D. J. W. Belleter, R. Galeazzi, and T. I. Fossen, "Experimental verification of a global exponential stable nonlinear wave encounter frequency estimator," *Ocean Engineering*, vol. 97, pp. 48–56, 2015.

[38] B. Tian, J. Yu, A. Zhang, F. Zhang, Z. Chen, and K. Sun, "Dynamics analysis of wave-driven unmanned surface vehicle in longitudinal profile," *Oceans 2014 - Taipei*, 2014.

[39] SNAME, "Nomenclature for treating the motion of a submerged body through a fluid," tech. rep., The Society of Naval Architects and Marine Engineers, New York, 1950.

[40] B. Siciliano and O. Khatib, *Springer Handbook of Robotics.* Springer, 2008.

[41] R. Deits, "Denavit Hartenberg analysis, part 5: Assigning coordinate frames," 2012.

[42] J. V. José and E. J. Saletan, *Classical Dynamics: A Contemporary Approach.* Cambridge University Press, 1998.

[43] G. Rampersadh, "Sea-state interaction based dynamic model of the Liquid Robotic's Wave Glider (submitted for publication)," Master's thesis, University of Cape Town, 2017.

[44] M. S. Longuet-Higgins, "On the statistical distribution of the heights of sea waves," *Journal of Marine Research*, vol. 11, no. 3, pp. 245–266, 1952.

[45] S. R. Massel, "On the geometry of ocean surface waves," *Institute of Oceanology of Polish Academy of Sciences*, vol. 53, pp. 521–548, 2011.

[46] N. Montazeri, U. D. Nielsen, and J. J. Jensen, "Estimation of wind sea and swell using ship-board measurements - a refined parametric modelling approach," *Applied Ocean Research*, vol. 54, pp. 73–86, 2016.

[47] K. Hasselmann, T. P. Barnett, E. Bouws, H. Carlson, D. E. Cartwright, K. Enke, J. A. Ewing, H. Gienapp, D. E. Hasselmann, P. Kruseman, A. Meerburg, P. Muller, D. J. Olbers, K. Richter, W. Sell, and H. Walden, *Measurements of Wind-Wave Growth and Swell Decay during the Joint North Sea Wave Project (JONSWAP).* Hamburg: Deutsches Hydrographisches Institut, 1973.

[48] K. E. Steele, C. Teng, and D. W. C. Wang, "Wave direction measurements using pitch-roll buoys," *Ocean Engineering*, vol. 19, pp. 349–357, 1992.

[49] M. Vidyasagar, *Nonlinear Systems Analysis.* Classics in Applied Mathematics, Society for Industrial and Applied Mathematics, 2nd ed., 2002.

[50] H. Akaike, "Likelihood of a model and information criteria," *Journal of Econometrics*, vol. 16, pp. 3–14, 1981.

[51] K. Yonekawa and M. Kawahara, "Application of Kalman filter finite element method and AIC," *International Journal of Computational Fluid Dynamics*, vol. 17, no. 4, 2003.

[52] F. L. Markley, "Attitude determination using two vector measurements," tech. rep., NASA Technical Documents, 1998.

[53] J. P. Le Roux, "Characteristics of developing waves as a function of atmospheric conditions, wave properties, fetch and duration," *Coastal Engineering*, vol. 56, pp. 479–483, 2009.

[54] E. Boje and M. Petrick, "Application of the extended kalman filter to a lysine hydrochlorination process," *Control Engineering Practice*, vol. 8, pp. 291–297, 2000.

[55] A. Papoulis, *Probability, Random Variables, and Stochastic Processes*. McGraw-Hill Series in Systems Science, McGraw-Hill Book Company, 1965.

[56] R. E. Kalman, "On the general theory of control systems," *IRE Transactions on Automatic Control*, vol. 4, pp. 481–492, 1959.

[57] Y. Bar-Shalom, X. Rong-Li, and T. Kirubarajan, *Estimation with Applications to Tracking and Navigation: Theory Algorithms and Software*. John Wiley & Sons, 2001.

[58] C. C. Paige, "Properties of numerical algorithms related to computing controllability," *IEEE Transactions on Automatic Control*, vol. 26, pp. 130–138, 1981.

[59] P. Kokotović, H. K. Khalil, and J. O'Reilly, *Singular Perturbation Methods in Control - Analysis and Design*. Society for Industrial and Applied Mathematics, 1999.

[60] W. F. Egan, *Phase-Lock Basics*. Wiley-IEEE Press, 2nd ed., 2007.

[61] D. Abramovitch, "Phase-locked loops: A control centric tutorial," *American Control Conference*, vol. 6, 2002.

[62] Edinburgh Designs, "Wave Generators." `http://www.edesign.co.uk/waves/`, 2016.

[63] N. D. Kraus, "Wave glider dynamic modeling, parameter identification and simulation," Master's thesis, University of Hawai'i, 2012.

This page has been intentionally left blank.

Appendix A

Alternative Estimation Strategies

The wind wave spectrum, $S(\omega)$, represents the expected values and variance of wave amplitudes. This works to our advantage, in that the estimation scheme can be characterised completely in the frequency domain, and use a single parameter (wind speed, U_{19}). The following two approaches make use of this fact.

A.1 Spectral Shaping Approach

The spectral shaping approach makes use of noise whitening. The problem is formulated by asking what filter, $P(\omega)$, gives the output of a random process, $h(x,t)$, when the input is white noise, w_n [28]. By using a product sum of polynomials, the shape of the wind wave spectrum can be approximated. The product sum used is of the form

$$P(\omega) = k \prod_{i=1}^{3} \left(\frac{1}{(s/\omega_i)^2 + 2\zeta(s/\omega_i) + 1} \right), \tag{A.1}$$

where k is a gain factor, ω_i is the frequency, and ζ is a damping term. Eq. A.1 is used to estimate the wind wave spectrum, which represents the power, as

$$\hat{S}(\omega) = |P(\omega)|^2. \tag{A.2}$$

Fig. A.1 shows an overview of the approach. A white noise, n_w, drives the estimation process, and K represents Kalman filter gains. The term $K\Delta y$ is driven to zero as the wave estimate approaches the real wave system.

Hence this alternative approach makes use of a polynomial, fitted onto a wind wave spectral model shape, as opposed to estimating individual Fourier components. This generates waves with the correct statistical properties. The disadvantage of this approach is that if the model chosen to represent the ocean wave spectrum is not representative of the true behaviour, then the estimation will be limited by this, no matter how well it works. Hence the method is not currently pursued.

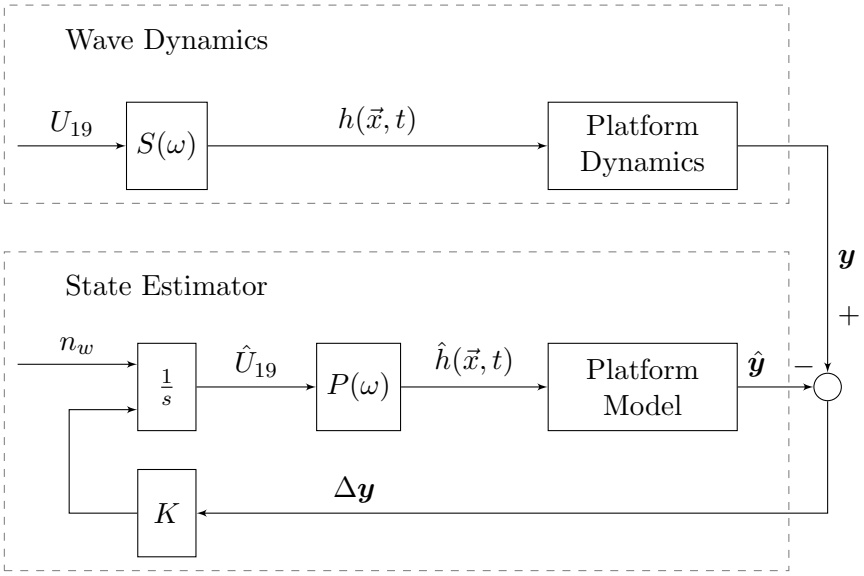

Figure A.1: Overview of the spectral shaping approach for sea state estimation. The term $K\Delta y$ is driven to zero as the wave estimate approaches the real wave system.

This page has been intentionally left blank.

Appendix B

Additional Simulation Results

In this section, further simulations conducted expand upon the results chapter. These include simulations of the WG dynamic model, wind wave generator, and sea state estimator.

B.1 Wave Glider Simulations

B.1.1 Impulse and Step Tests

The velocity and position can be set directly in the model as initial conditions. This is useful for validation of the buoyancy force interaction. Fig. B.1 and B.2 show the response of the platform when it is dropped from 1 m above the water surface, with the float at an angle of $\frac{\pi}{4}$ rad to the horizontal plane. The platform initially oscillates due to the buoyancy force interacting with the weight, while also experiencing a righting moment. It reaches a settling point of 0.06 m, measured from the platform's centre of mass. This depth makes the submerged volume required to generate a buoyancy force equal to the platform weight. As expected, there is a minor response in the x coordinate as a result of coupling, but zero response for any initial x position.

External forces and torques are applied as impulses and steps to the WG. Fig. B.3 is the response of the WG to an impulse of 10 kN in the positive x coordinate at 1 s in the simulation. The position settles at 1 m after 5 s.

In Fig. B.4, a 0.1 kN force step in the positive x coordinate is exerted on the WG at 1 s into the simulation. This results in a step response in the velocity, and a subsequent ramp response in position. After 5 s, $\dot{x}$ settles at $1\,\mathrm{m}\cdot\mathrm{s}^{-1}$, while the position is a ramp. This response is due to the velocity dependent damping, $F = \beta v$, that results in no further acceleration.

The WG is subjected to a sinusoidal input at an angle of arrival of 0 rad (purely from the positive x coordinate). Fig. B.5 shows the sinusoidal response of the WG. Once the platform reaches steady-state, it follows the sea surface motion represented by the pure sinusoid, in the x coordinate. In addition, the angle, θ_1, follows the same motion at π rad out of phase with the x position, shown in Fig. B.6.

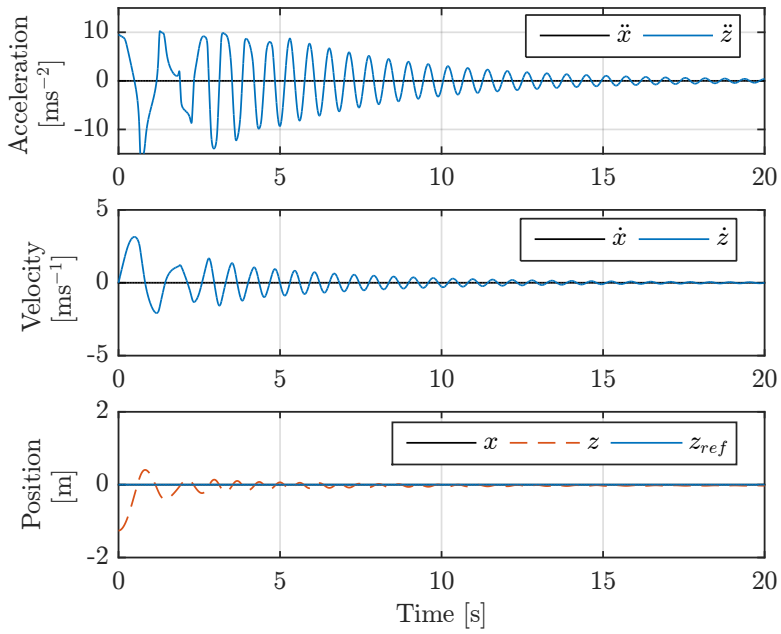

Figure B.1: WG float dropped from 1 m above the mean ocean surface, resulting in some initial oscillations due to the buoyancy and gravity interaction. The platform's centre of gravity finally settles at 0.06 m, the depth required for buoyancy to counteract the platform's weight.

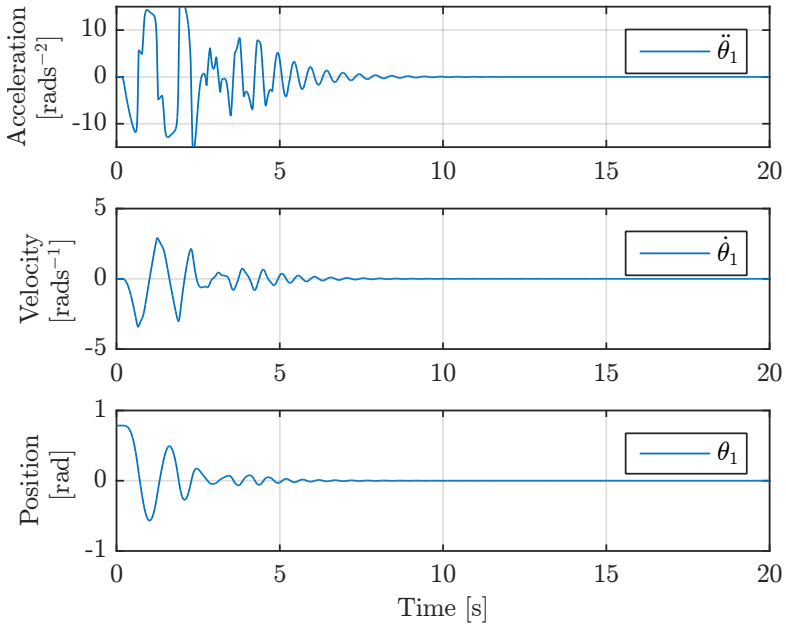

Figure B.2: WG float dropped from 1 m above the mean ocean surface with the float at an angle of $\frac{\pi}{4}$ radian, resulting in some initial oscillations due to the buoyancy righting moment, finally settling at 0 rad.

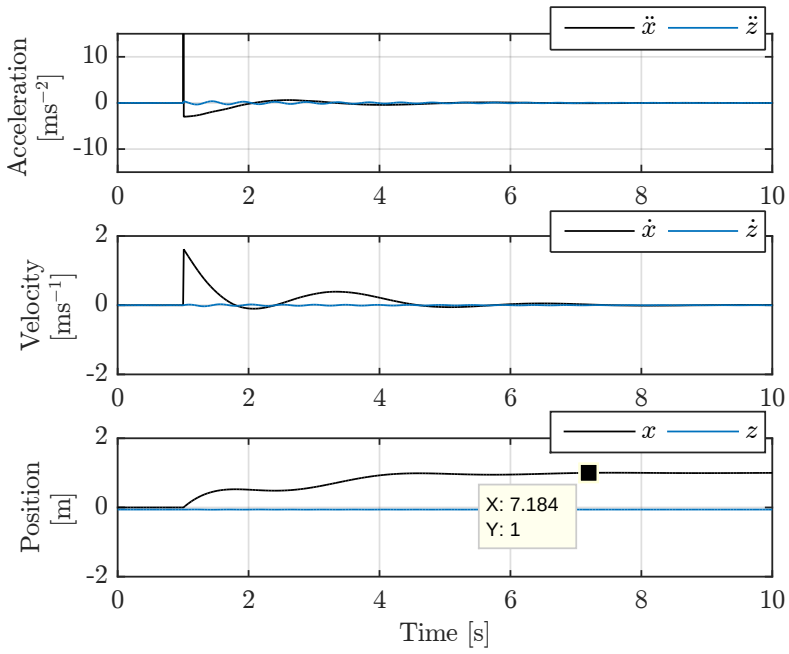

Figure B.3: Response of WG to a 10 kN impulse exerted in the x coordinate; (top) acceleration shows momentary impulse in x; (middle) velocity spikes as a result of the impulse, settling to $0\,\mathrm{m}\cdot\mathrm{s}^{-1}$ after 4 s; (bottom) the position settles at 1 m after 5 s.

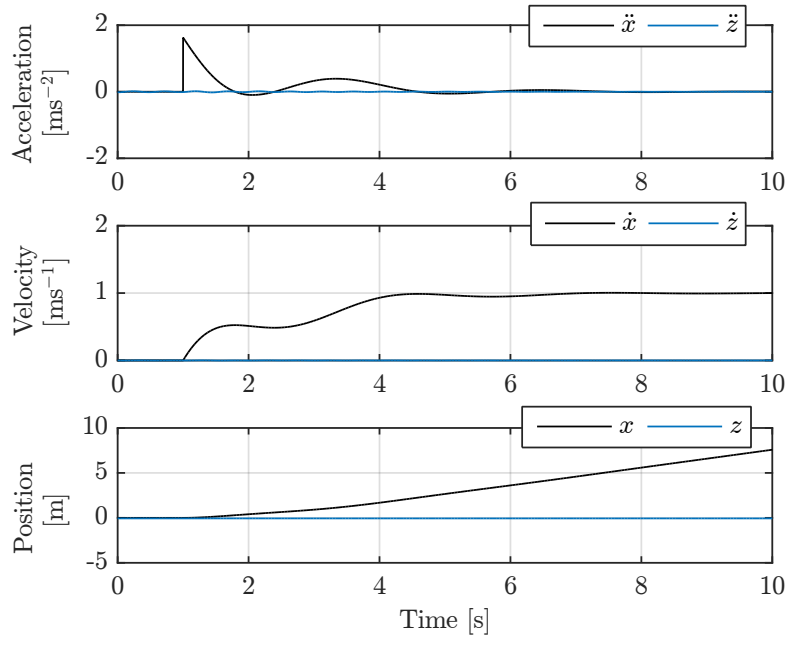

Figure B.4: Response of WG to a 0.1 kN force step in the positive x coordinate; (top) acceleration in x spikes as a result of the step, settling to $0\,\mathrm{m}\cdot\mathrm{s}^{-1}$ after 4 s; (middle) velocity settles at 1 m after 5 s; (bottom) the step causes the position to ramp at $1\,\mathrm{m}\cdot\mathrm{s}^{-1}$ at steady-state.

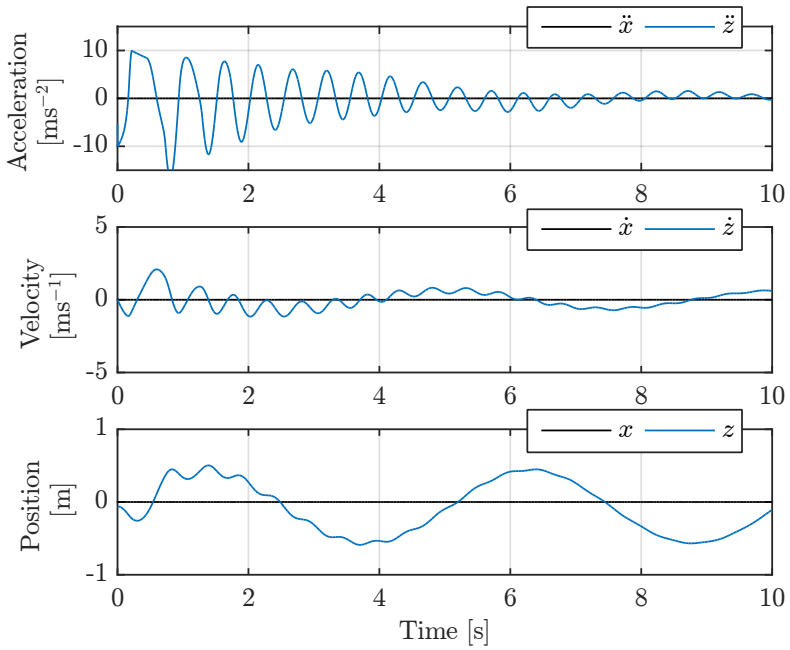

Figure B.5: Response of WG to sinusoidal input; the acceleration, velocity and position of the platform in the x and z coordinates show the platform settling on the smooth sinusoidal motion of the input.

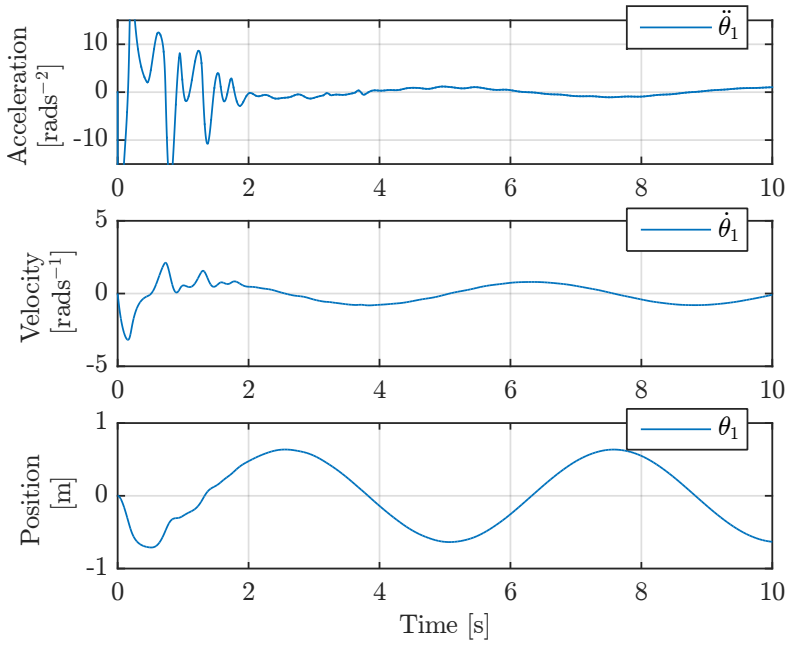

Figure B.6: Response of WG to sinusoidal input; the angular acceleration, velocity and position in the θ frame, settling on the sinusoidal motion of the input, at π rad out of phase with the motion in x.

B.1.2 Wave Glider Platform Under Varying Wave Conditions

The ocean wave generator takes in wind speed, U_{19}, and direction of arrival, θ, as inputs and produces deep sea waves. Fig. B.7 shows the WG response to a sea state generated using a wind speed, $U = 7\,\mathrm{m} \cdot \mathrm{s}^{-1}$ at a mean direction of 0 rad.

B.2 Spectral Estimation Simulations

B.2.1 Mean Wave Direction

Fig. B.9 shows the estimation of a constant mean wave direction of 0.5π rad from the positive x coordinate. The filter is initiated at 0 rad, and takes approximately 600 s to settle. This simulation is repeated with a constant mean wave direction of -0.5π rad from the positive x coordinate, and gives a similar result shown in Fig. B.10. The largest step in wave direction expected is π rad (the waves are coming from the opposite direction to the initial condition). When this is simulated, the filter takes approximately 1300 s to settle, shown in Fig. B.11. A long delay in response is present, before the estimate starts to converge on the true value.

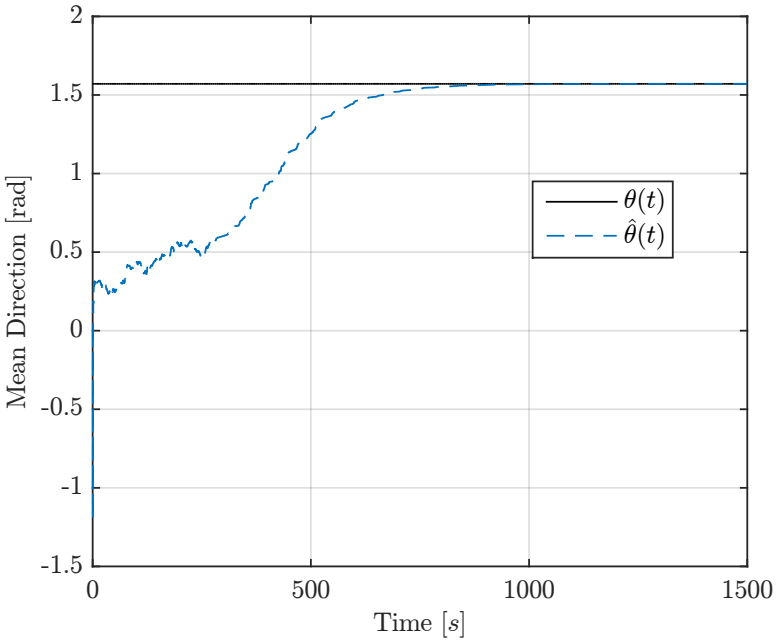

Figure B.9: Kalman filter tracking the mean wave direction, set to a constant value of 0.5π rad from the positive x coordinate.

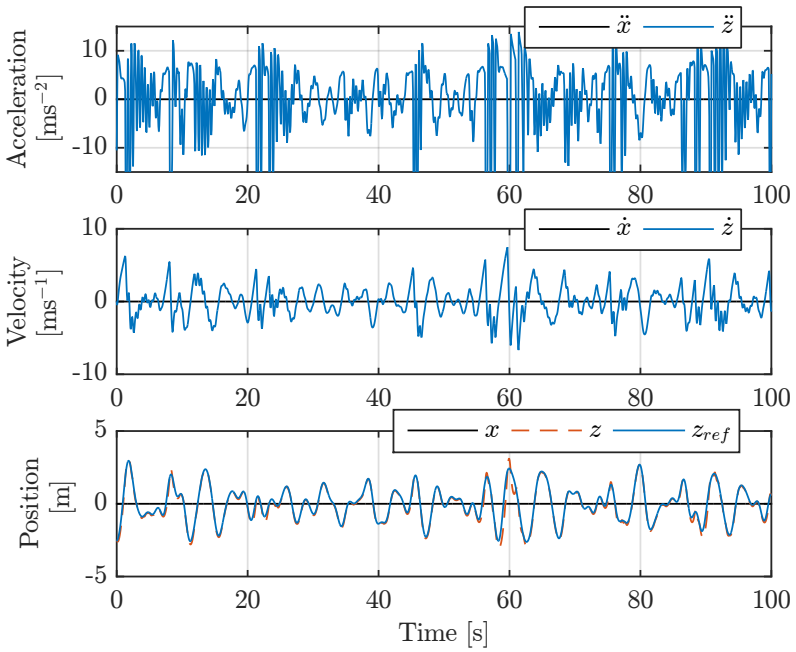

Figure B.7: Response of WG to sinusoidal input; the angular acceleration, velocity and position in the θ frame, settling on the sinusoidal motion of the input, at π rad out of phase with the motion in x.

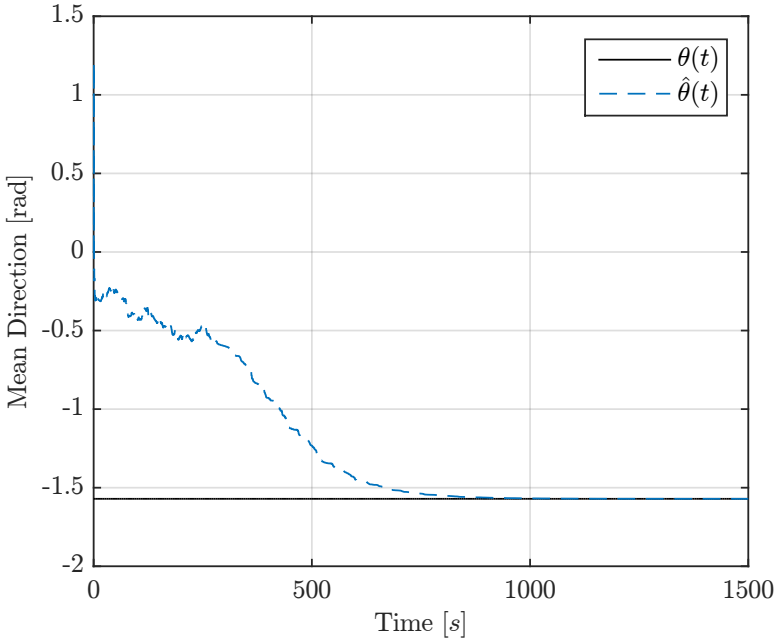

Figure B.10: Kalman filter tracking the mean wave direction, set to a constant value of -0.5π rad from the positive x coordinate.

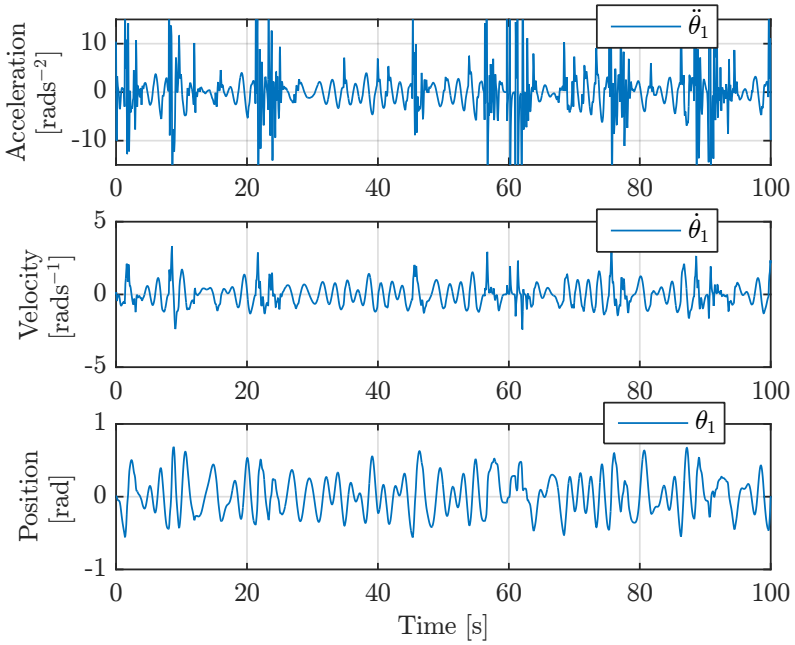

Figure B.8: Response of WG to sinusoidal input; the angular acceleration, velocity and position in the θ frame, settling on the sinusoidal motion of the input, at π rad out of phase with the motion in x.

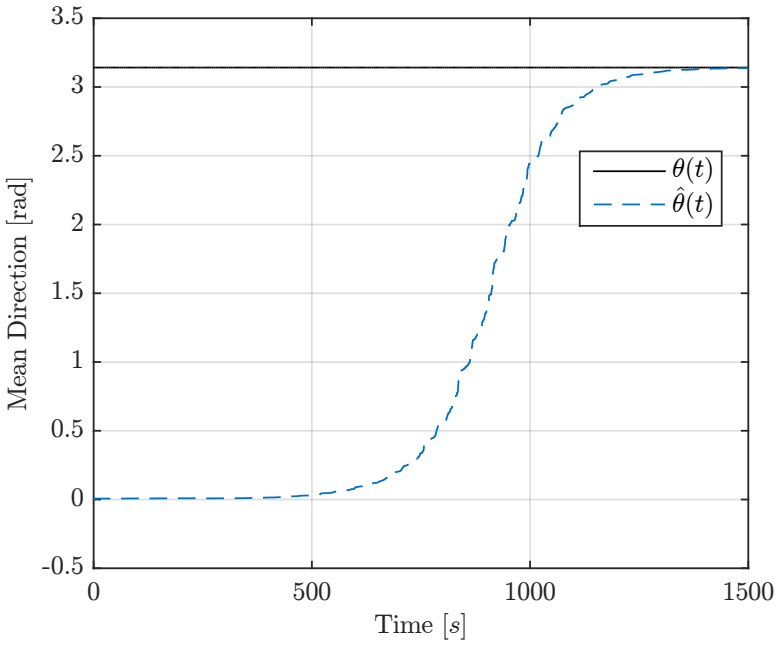

Figure B.11: Kalman filter tracking the mean wave direction, set to a constant value of π rad from the positive x coordinate, representing the largest step expected in the mean wave direction. A long delay in response is present, before the estimate starts to converge on the true value.

B.2.2 Process Noise Comparison

For the estimator, sources of uncertainty in the process model stem from discretisation and behaviour of the model. As explained in Chapter 5.4.1, the states, h_i and $\dot{h}_i$, are coupled because one is the time integral of the other. Hence it is not necessary to calculate both process deviations for each component, and the deviation for $\dot{h}_i$ can be set to zero, $\sigma^2_{\dot{h}_i} = 0$. However, a possible benefit of having noise feed in from the derivative state is that it allows for smoother changes at the output, due to the integration.

This is verified through simulation of both cases under similar conditions. The performance metric used in this simulation is the wave height error deviation, $\sqrt{P_{hh}}$, after the filter has reached steady-state. With the process noise contributed through the $\dot{h}_i$ state, the deviation is 7.48×10^{-2} m. This is a much lower value than when the process noise is contributed through h_i, at $\sqrt{P_{hh}} = 21.62 \times 10^{-2}$ m.

This page has been intentionally left blank.

Appendix C

Explanation of Operators Used

diag()

This function takes its arguments as elements and places them along the leading diagonal of a matrix.

$$A = \text{diag}(a, b, c, d) \tag{C.1}$$

$$A = \begin{bmatrix} a & 0 & 0 \\ 0 & b & 0 \\ 0 & 0 & c \end{bmatrix} \tag{C.2}$$

In the case where any number of the elements a, b, c or d, are themselves matrices, then the diag() function forms the block diagonal matrix.

$$B = \text{diag}(A, e, f) \tag{C.3}$$

$$B = \begin{bmatrix} a & 0 & 0 & 0 & 0 \\ 0 & b & 0 & 0 & 0 \\ 0 & 0 & c & 0 & 0 \\ 0 & 0 & 0 & e & 0 \\ 0 & 0 & 0 & 0 & f \end{bmatrix} \tag{C.4}$$

npow()

This function finds the next higher power of two for the argument provided. For example, to find the next highest power of 2 above 489, g is calculated as

$$g = 2^{\text{npow}(489)}, \tag{C.5}$$

$$= 2^{\text{ceil}(\log_2(489))}, \tag{C.6}$$

$$= 2^9 = 512. \tag{C.7}$$

logspace()

This function creates a logarithmically spaced vector, from 10^a to 10^b, with n points.

$$\omega = \text{logspace}(a, b, n) \tag{C.8}$$

$$\omega = \text{logspace}(0, 1, 10) \tag{C.9}$$

$$\omega = \begin{bmatrix} 1.0000 & 1.7783 & 3.1623 & 5.6234 & 10.0000 \end{bmatrix} \tag{C.10}$$

This page has been intentionally left blank.

Appendix D

Ethics Form

Application for Approval of Ethics in Research (EiR) Projects
Faculty of Engineering and the Built Environment, University of Cape Town

APPLICATION FORM

Please Note:
Any person planning to undertake research in the Faculty of Engineering and the Built Environment (EBE) at the University of Cape Town is required to complete this form **before** collecting or analysing data.The objective of submitting this application *prior* to embarking on research is to ensure that the highest ethical standards in research, conducted under the auspices of the EBE Faculty, are met. Please ensure that you have read, and understood the **EBE Ethics in Research Handbook**(available from the UCT EBE, Research Ethics website) prior to completing this application form: http://www.ebe.uct.ac.za/usr/ebe/research/ethics.pdf

APPLICANT'S DETAILS		
Name of principal researcher, student or external applicant		Tinashe Gwatiringa
Department		Department of Electrical Engineering
Preferred email address of applicant:		GWTTIN002@myuct.ac.za
If a Student	Your Degree: e.g., MSc, PhD, etc.,	MSc. Electrical Engineering
	Name of Supervisor (if supervised):	Professor E. Boje
If this is a researchcontract, indicate the source of funding/sponsorship		DST/CSIR ROSSA Grant
Project Title		Sea State Estimation using Wave Glider platform

I hereby undertake to carry out my research in such a way that:

- there is no apparent legal objection to the nature or the method of research; and
- the research will not compromise staff or students or the other responsibilities of the University;
- the stated objective will be achieved, and the findings will have a high degree of validity;
- limitations and alternative interpretations will be considered;
- the findings could be subject to peer review and publicly available; and
- I will comply with the conventions of copyright and avoid any practice that would constitute plagiarism.

SIGNED BY	Full name	Signature	Date
Principal Researcher/ Student/External applicant	Tinashe Gwatiringa	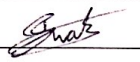	**19 May 2016**

APPLICATION APPROVED BY	Full name	Signature	Date
Supervisor (where applicable)	Professor E. Boje		23/5/16
HOD (or delegated nominee) Final authority for all applicants who have answered NO to all questions in Section1; and for all Undergraduateresearch (Including Honours).	Professor E. Boje		23/5/16
Chair : Faculty EIR Committee For applicants other than undergraduate students who have answered YES to any of the above questions.	Click here to enter text.		